Accelerating Nonlinear Model Predictive Control through Machine Learning with Application to Automotive Waste Heat Recovery

Beschleunigung Nichtlinearer Modellprädiktiver Regelung mittels Maschinellem Lernen mit Anwendung auf Abwärmerückgewinnung in Fahrzeugen

Von der Fakultät für Maschinenwesen der Rheinisch-Westfälischen Technischen Hochschule Aachen zur Erlangung des akademischen Grades eines Doktors der Ingenieurwissenschaften genehmigte Dissertation

vorgelegt von

Yannic Vaupel

Berichter: Universitätsprofessor Alexander Mitsos, Ph. D.
Universitätsprofessor Dr.-Ing. Sergio Lucia

Tag der mündlichen Prüfung: 04.12.2020

Titel: Accelerating Nonlinear Model Predictive Control through Machine Learning with Application to Automotive Waste Heat Recovery

Autor: Yannic Vaupel

Reihe: Aachener Verfahrenstechnik Series
AVT.SVT - Process Systems Engineering
Band 12 (2020)

Herausgeber: Aachener Verfahrenstechnik
Forckenbeckstraße 51
52074 Aachen
Tel.: +49 (0)241 80 97717
Fax: +49 (0)241 80 92326
E-Mail: secretary.svt@avt.rwth-aachen.de
https://www.avt.rwth-aachen.de

Vorwort

Die vorliegende Arbeit entstand während meiner Zeit als wissenschaftlicher Mitarbeiter am Lehrstuhl für Systemverfahrenstechnik (AVT.SVT) der RWTH Aachen. Mein besonderer Dank gilt an erster Stelle meinem Doktorvater, Professor Alexander Mitsos, Ph. D., für seine Unterstützung, Anregungen und das in mich gesetzte Vertrauen. Weiterhin danke ich Professor Dr.-Ing. Sergio Lucia für die Übernahme des Koreferates und Professor Dr.-Ing. Stefan Pischinger für die Übernahme des Prüfungsvorsitzes. Meinen Kolleginnen und Kollegen an der SVT bin ich für die vielen fachlichen und nicht-fachlichen Diskussionen ebenfalls zu großem Dank verpflichtet. Das Arbeitsklima am Lehrstuhl war stets hervorragend und ich bin (fast) jeden Tag gerne zur Arbeit gefahren. Aus einigen Kollegen sind enge Freunde geworden und ich hoffe, dass wir uns auch in Zukunft verbunden bleiben werden.
Des Weiteren danke ich Dr.-Ing. Adel Mhamdi Dank für die gute Zusammenarbeit in Forschung und Lehre, sowie insbesondere auch für die moralische Unterstützung in schwierigen Projektphasen. Da wissenschaftliche Mitarbeiter kommen und gehen, sind es in erheblichem Maße die nicht-wissenschaftlichen Mitarbeiter die Arbeitsprozesse und das Arbeitsklima des Lehrstuhls prägen. Daher gilt besonderer Dank Wanda Frohn, Petra Eissa, Didem Uslu, Jutta Friedrich sowie Sascha Gerhards für ihre jahrelange Arbeit.
Besondere Freude hat mir stets die Betreuung von studentischen Arbeiten bereitet. Darum danke ich allen Studierenden, die zum Gelingen dieser Arbeit beigetragen haben.
Weiterhin danke ich meinen Freunden die während Schulzeit, Studium und Promotion stets an meiner Seite standen sowie Julia für ihre Liebe (und therapeutische Unterstützung) in der Endphase dieser Arbeit. Zuletzt gilt mein Dank meinen Großeltern, die den Abschluss dieser Arbeit leider nicht mehr erleben durften, sowie meinen Eltern dafür, dass sie stets hinter mir standen und mir alles ermöglicht haben.

Köln, im Dezember 2020 *Yannic Vaupel*

Contents

Kurzfassung

Als Teil einer Strategie zur Reduzierung des CO_2-Fußabdrucks der Transportbranche ist der Einsatz von Wärmerückgewinnungssystemen in LKW eine vielversprechende Option. Dafür kommt eine Reihe möglicher Technologien in Betracht, wobei der Einsatz eines Organic Rankine Cycles (ORC), unter Nutzung der thermischen Energie des Abgases als Wärmequelle, als besonders vielversprechend gilt. Beim Einsatz im LKW ist das ORC-System, im Gegensatz zu etablierten Einsatzfeldern von ORCs, starken Fluktuationen der Wärmequelle ausgesetzt. Daraus ergeben sich substantielle Herausforderungen für den sicheren und effizienten Betrieb des Wärmerückgewinnungssystems.

In dieser Arbeit werden diese Herausforderungen mittels modellbasierter Methoden adressiert. Zu Beginn wird ein dynamisches Modell des ORC-Systems entwickelt und mit Messdaten validiert. Anschließend erfolgt eine Erweiterung zu einem schaltenden Modell, sodass auch An- und Abfahrvorgang abgebildet werden können. Darüber hinaus werden zwei Modellierungsansätze für Wärmeübertrager verglichen.

Im Rahmen einer modellbasierten dynamischen Optimierung wird anschließend der optimale Betrieb des Wärmerückgewinnungssystems analysiert. Dabei stellt sich heraus, dass eine temporäre Erhöhung der Überhitzung des Arbeitsmediums sinnvoll sein kann. Aus den gewonnenen Erkenntnissen wird eine Regelungsstruktur abgeleitet. Diese wird simulativ mit nichtlinearer Modellprädiktiver Regelung (NMPC) sowie einem PI-Regler mit Störgrößenaufschaltung umgesetzt. Die erreichte Regelungsgüte des NMPC ist hoch, allerdings übersteigt der Rechenaufwand die zulässige Rechendauer. Der PI-Regler erreicht eine ähnliche Regelgüte mit deutlich geringerem Rechenaufwand.

Anschließend wird eine auf maschinellem Lernen (ML) basierende NMPC Methode auf das ORC System angewandt. Diese reduziert den rechnerischen Aufwand, kann aber keine Einhaltung der Pfadbeschränkungen garantieren. Daher werden als finaler Beitrag der Arbeit Methoden entwickelt, die mittels ML den rechnerischen Aufwand von NMPC reduzieren und dabei Pfadbeschränkungen beachten.

Summary

Waste heat recovery (WHR) from heavy-duty (HD) diesel trucks is a viable option for reducing the carbon footprint of the transport industry. Among the various available technology options for WHR, using a bottoming organic Rankine cycle (ORC) with the exhaust gas as heat source is considered the most promising. The ORC system in a HD diesel truck is subject to strong heat source fluctuations, which is in contrast to ORC operation in established processes. This poses substantial challenges for safe and efficient operation of the WHR system.

In this thesis, we address these challenges using model-based methods. We first develop a dynamic ORC model for WHR and validate it with measurement data from a test rig. Next, we extend our dynamic model to a switching model that it is capable of accounting for start-up and shutdown situations. We compare two popular modeling approaches for the heat exchangers, identifying their perks and weaknesses.

With our model established, we use dynamic optimization to understand how the system is best operated and we find that it can be beneficial to temporarily increase workfing fluid superheat in certain situations. From our findings, we derive a control structure for model-based control of the process. We apply this structure in silico to nonlinear model predictive control (NMPC) and to a PI controller with feedforward term. Our findings indicate good control performance of NMPC but excessive computational demand for on-board application. The PI controller achieves similar control performance at insignificant computational demand.

Next, we apply a machine-learning (ML) based method for NMPC to the ORC system. While this achieves a drastic reduction in online computational demand, constraint satisfaction cannot be guaranteed. Hence, as a final contribution, we develop methods that use ML to reduce the computational demand of NMPC while promoting constraint satisfaction.

Publications and Copyrights

This thesis originates from research performed by the author during his time at the Chair of Process Systems Engineering at Aachener Verfahrenstechnik (AVT.SVT). Parts of this thesis have already been published. The publications are integrated in the following chapters as described:

- We published a large part of Chapter 3 together with Appendix A in [1]. W. R. Huster and Y. Vaupel jointly developed and implemented the model and performed the parameter estimation and model validation. W. R. Huster, Y. Vaupel, A. Mhamdi, and A. Mitsos contributed to the development of the original idea and to the writing of the manuscript.
- We published a large part of Chapter 4 together with Appendix B in [2]. Y. Vaupel and W. R. Huster jointly implemented the switching MB model. Y. Vaupel, W. R. Huster, and F. Holtorf jointly developed and implemented the FV model. Y. Vaupel carried out the analysis regarding start-up operation. Y. Vaupel, W. R. Huster, F. Holtorf, A. Mhamdi, and A. Mitsos contributed to the development of the original idea and to the writing of the manuscript.
- We submitted a large part of Chapter 5 in [3] and published a preprint in [4]. Y. Vaupel implemented the model in Modelica and the problems in DyOS. Y. Vaupel carried out the simulations and analyzed the results. Y. Vaupel, W. R. Huster, A. Mhamdi, and A. Mitsos contributed to the development of the original idea and to the writing of the manuscript.
- We published a large part of Chapter 6 in [5]. Y. Vaupel and J. C. Schulze implemented the controllers. Y. Vaupel carried out the simulations and analyzed the results. Y. Vaupel, J. C. Schulze, A. Mhamdi, and A. Mitsos contributed to the development of the original idea and to the writing of the manuscript.
- We published a large part of Chapter 7 in [6]. Y. Vaupel and N. C. Hamacher implemented the method. Y. Vaupel carried out the simulations and analyzed the results. Y. Vaupel, A. Caspari, W. R. Huster, A. Mhamdi, I. G. Kevrekidis,

and A. Mitsos contributed to the development of the original idea and to the writing of the manuscript.

- We published a large part of Chapter 8 together with Appendices C, D and E in [7]. Y. Vaupel implemented the methods, carried out the simulations and analyzed the results. N. C. Hamacher implemented an early version of dANN. Y. Vaupel, A. Caspari, A. Mhamdi, I. G. Kevrekidis, and A. Mitsos contributed to the development of the original idea and to the writing of the manuscript.

Additionally, the author contributed to the following publications during his time at AVT.SVT, which are not part of this thesis:

- A. Caspari, A. M. Bremen, J. M. M. Faust, F. C. Jung, C. D. Kappatou, S. Sass, Y. Vaupel, R. Hannemann-Tamás, A. Mhamdi, and A. Mitsos, "DyOS: A framework for optimization of large-scale differential algebraic equation systems," *Computer Aided Chemical Engineering* vol. 46, pp. 619–624, 2019.
- A. Caspari, L. Lüken, P. Schäfer, Y. Vaupel, A. Mhamdi, and A. Mitsos, "Dynamic optimization with complementarity constraints: Smoothing for direct shooting," *Computers & Chemical Engineering* vol. 139, 106891, 2020.
- D. T. Doncevic, A. M. Schweidtmann, Y. Vaupel, P. Schäfer, A. Caspari, and A. Mitsos, "Deterministic global nonlinear model predictive control with neural networks embedded," *21st IFAC World Congress*, 2020.
- P. Schäfer, A. Caspari, A. M. Schweidtmann, Y. Vaupel, A. Mhamdi, and A. Mitsos, "The potential of hybrid mechanistic/data-driven approaches for reduced dynamic modeling: Application to distillation columns," *Chemie Ingenieur Technik* vol. 92 (12), pp. 1910–1920, 2020.

During his time at AVT.SVT, the author supervised the student theses of Laura Mey [8], Johannes Wiebe [9], Christin Köhler [10], Nils Christian Hamacher [11], Jan Christoph Schulze [12], Benedikt Bier [13], Ashutosh Manchanda [14] and Aron Zingler [15]. The work of all students is acknowledged. In the Bachelor's thesis of N. C. Hamacher [11], dANN is presented for the polystyrene case study. For Chapter 8, Y. Vaupel re-implemented and improved the method, adjusted the case study, carried out new simulations and analyzed the results. In the Master's thesis of J. C. Schulze [12], nonlinear model predictive controllers for the ORC system with a reduced model are presented. Chapter 6 is based on the presented insights. Y. Vaupel, adjusted the controllers to the full ORC model, implemented an additional controller, carried out the simulations and processed the results.

Copyrights

Parts of the following publications, especially figures, are included in this thesis and are reprinted with permission:

- Reprinted from W. R. Huster, Y. Vaupel, A. Mhamdi, and A. Mitsos, "Validated dynamic model of an organic Rankine cycle (ORC) for waste heat recovery in a diesel truck," *Energy*, vol. 151, pp. 647–661, 2018. Copyright © (2018), Elsevier.
- Reprinted from Y. Vaupel, W. R. Huster, F. Holtorf, A. Mhamdi, and A. Mitsos, "Analysis and improvement of dynamic heat exchanger models for nominal and start-up operation," *Energy*, vol. 169, pp. 1191–1201, 2019. Copyright © (2019), Elsevier.
- Reprinted from Y. Vaupel, A. Caspari, N. C. Hamacher, W. R. Huster, A. Mhamdi, I. G. Kevrekidis, and A. Mitsos, "Artificial neural networks for real-time model predictive control of organic Rankine cycles for waste heat recovery," in *Proceedings of the 5th international seminar on ORC power systems*, 2019. Copyright © (2019), National Technical University of Athens.
- Reprinted from Y. Vaupel, N. C. Hamacher, A. Caspari, I. G. Kevrekidis, A. Mhamdi, and A. Mitsos, "Accelerating nonlinear model predictive control through machine learning," *Journal of Process Control*, vol. 92, pp. 261–270, 2020. Copyright © (2020), Elsevier.
- Reprinted from Y. Vaupel, J. C. Schulze, A. Mhamdi, and A. Mitsos, "Nonlinear model predictive control of organic Rankine cycles for automotive waste heat recovery: Is it worth the effort?," *Journal of Process Control*, vol. 99, pp. 19–27, 2021. Copyright © (2021), Elsevier.

Chapter 1

Introduction

The transport sector accounted for 14% of worldwide direct greenhouse gas emissions (GHG) in 2010 according to the Intergovernmental Panel on Climate Change (IPCC) [16]. To limit global warming by the year 2100 to 2 °C compared to pre-industrial levels, an unprecedented effort among all industries is required. Therefore, decarbonization of the transport industry is an important aim [17]. A major contributor to GHG emissions from the transport sector is road transport. Here, heavy-duty (HD) diesel trucks, are the largest source of GHG emissions. Consequently, there is regulatory pressure to improve fuel economy of HD trucks, e.g., in the european market [18]. Furthermore, the reduction in operating cost associated with improved fuel economy provides an additional selling proposition for vehicle manufactures in an enormously cost-sensitive industry.

Internal combustion engine (ICE) vehicles, and HD trucks in particular, have a long history of fuel economy improvement through engine technology innovation [19]. However, as further improvement through traditional levers (engine efficiency, powertrain efficiency, aerodynamic efficiency) is limited, creative approaches are imperative. Considering that only around 40 % of fuel energy is converted to propulsion energy [20], waste heat discharged to the environment from the exhaust gas and coolant provides a potential lever. Accordingly, waste heat recovery (WHR) has become a heavily researched approach to improve fuel efficiency of vehicles. A variety of technologies to realize the conversion of thermal energy to either mechanical or electric energy exist. The most discussed technologies are thermoelectric generators, turbocompounding and the organic Rankine cycle (ORC). In this thesis, we will focus on the ORC. Like the steam Rankine cycle, the ORC is a thermodynamic cycle that utilizes a heat source to evaporate a pressurized working fluid and generates mechanical energy through expanding the working fluid. In contrast to the steam Rankine cycle, an organic working

fluid is used. This makes the process more suitable for low to medium-temperature heat sources such as coolant or exhaust gas of HD trucks. Consequently, the ORC is an established technology for a variety of applications ranging from geothermal power generation [21] to industrial waste heat recovery [22]. Employing an ORC in a vehicle, however, raises issues that are not encountered in classic ORC applications. The system is required to be small in order to maintain high payload and light-weight in order to avoid detrimental effects on fuel economy. Furthermore, high safety standards apply which makes the use of many flammable working fluids questionable. Beyond design aspects, operation of the system is inherently complex, since, in contrast to classical ORC applications, the heat source varies strongly with limited predictability. Therefore, control system design requires careful consideration so that the control system is able to reject these disturbances.

In this thesis, we will focus on safe and economically optimal operation of the system. We will apply a model-based approach to understand and optimize system operation of the ORC system. To this end, process simulation is a powerful tool. As the ORC system has considerable thermal inertia, a dynamic process model is required to adequately describe its operation in a HD truck. To develop such a model, it has to be considered which phenomena of the process occur sufficiently fast to be considered as steady-state, which phenomena warrant consideration of dynamic effects and which phenomena occur slow enough to be practically irrelevant. For dynamic ORC models, the pump and expansion machine can typically be considered as steady-state and the most relevant dynamic phenomena occur in the heat exchangers, i.e., in the evaporator and condenser. For all process units, adequate models have to be developed. These typically consists of mass and energy balances and, in case a pressure drop is to be considered, momentum balances. Finally, phenomenological equations are required to describe the physical properties and transport phenomena, in particular heat transfer. With a dynamic model established, simulations can be executed that enhance understanding of the process and its dynamic behavior. Thereby, it is for example possible to understand the effect of changes in the heat source conditions on the system. Provided that the model contains the necessary features, simulation of a system start-up or a complete driving cycle is possible. Dynamic process models can furthermore be used in dynamic optimization problems to find optimal operating policies for a specified objective.

Dynamic optimization is a subclass of numerical optimization where the optimization problem is subject to the dynamic model equations and user-specified constraints on input and state variables. As the inputs and constraints are continuous in time, the problem is of infinite dimension. However, the problem can be approximated in finite dimension with methods that either “first optimize then discretize” or “discretize

then optimize" [23]. In this thesis, we use direct single shooting which is of the latter type. In contrast to simple simulation, we can gain much more insight using dynamic optimization. For example, we might be interested in how the ORC system has to be operated in order to maximize power production during a specific driving cycle or how to reach power production as fast as possible from a cold start. Although we could try to find a good operation strategy by trial and error, this would be a cumbersome process for a transient driving cycle with many degrees of freedom due to the time-dependent inputs. Furthermore, even if we had a preconception of what constitutes an optimal input for a specific scenario, we would need an optimization solver to obtain a certificate of optimality.

For a variety of reasons, results from offline dynamic optimization cannot be directly employed to operate the system. First, the heat source conditions in real-world operation might significantly deviate from the benchmark driving cycles considered in dynamic optimization. Second, due to mismatch between our model and the real system, the system might react to the computed controls differently than expected. Thus, we cannot directly use our results in an open-loop manner but rather we have to use feedback control to operate the system. For developing a suitable control system, our insights from dynamic optimization can be helpful. The control method closest to our dynamic optimization approach is nonlinear model predictive control (NMPC). Here, also an optimal control problem is solved. In contrast to dynamic optimization, however, only part of the full time frame, the prediction horizon, is considered. Thereby, the size of the optimal control problem can be reduced so that it can be solved in a reasonable time, which allows for implementation as a controller. The problem is then re-solved after one sampling interval to introduce feedback. The objective function in NMPC can be either regulatory, i.e., tracking of a prescribed set-point or set-point trajectory or it can be motivated by economics (eNMPC) [24]. In the latter case, one can design a controller that automatically operates the system such that power production is maximized.

Although we solve the optimal control problem on a limited horizon, NMPC is associated with significant computational cost. As the technology is increasingly employed outside of classic fields, e.g., chemical plants, this is a relevant concern for many applications where dynamics are fast and little computational power is available. In the case of WHR in a vehicle, the control signal has to be updated frequently due to the fast changes in driving conditions. Furthermore, the available computational power is relatively small. The high computational cost of NMPC is a long-standing issue and, unsurprisingly, many methods to alleviate this problem have been proposed. The most prominent is explicit MPC, which originally was proposed for linear model predictive control [25]. Here, the fact that the optimal control problem is parametric

in the initial state is exploited by solving the parametric program a priori and storing the result. Similar notions are exploited in fast-update methods [26], where an approximate solution is found based on the assumption that it only changes slightly compared to the previous solution. As explicit MPC reaches its limits for increasing problem size, it has been suggested to learn the optimal control policy based on offline simulation with a machine learning (ML) method [27]. These methods are straightforward to use but have the drawback that their success depends on careful training of the ML model. Furthermore they do not guarantee constraint satisfaction, which is a major feature of MPC.

In this thesis, we address many of the points raised before. First, we provide the necessary background with a literature review in Chapter 2. In particular, we discuss technological options for automotive WHR. We only briefly touch turbocompounding and thermoelectric generators and focus on ORC technology. Furthermore, we discuss the basics of dynamic optimization and NMPC. Finally, we provide a brief overview of artificial neural networks (ANN), which is the ML model used in this work. We start the main sections of the thesis by developing a dynamic model of an ORC for automotive WHR in Chapter 3 with a heat exchanger model based on the moving boundary (MB) approach [28]. We use dynamic optimization to estimate key parameters such that the model matches data obtained from a test rig and subsequently validate the model on another data set. The model we establish in Chapter 3 is only applicable when all three phases (liquid, two-phase and vapor) are present in the heat exchangers ("nominal operation"). To allow for simulation of situations where this is not the case, e.g., start-up or temporary loss of superheat, we extend the heat exchanger model to account for non-nominal operation in Chapter 4. For comparison, we also implement a heat exchanger model based on the finite volume (FV) approach in Chapter 4. We analyze the models in non-nominal operation and show that the MB model can produce unphysical results due to the enthalpy averaging assumptions. We propose two remedies to solve the issue. After developing an ORC model and analyzing the properties of commonly used heat exchanger models, we proceed to find optimal operating policies for the system in Chapter 5. Therefore, we assess typical driving situations with dynamic optimization. We find that, in contrast to steady-state operation, several peaks in superheat occur in optimal operation of a typical driving cycle. However, the additional produced power compared to operation at minimal superheat is negligible. In a situation where the power that can be utilized is temporarily limited, we find that it is sensible to increase superheat in order to store thermal energy in the heat exchanger walls for later use. In Chapter 6, we transfer the findings from Chapter 5 to a control setting. We compare NMPC strategies with regulatory and economic objective function to a PI controller with feedforward term. We find that

the NMPC controllers only hold small economic advantages over the PI controller. The NMPC strategies in Chapter 6 are not real-time capable for the WHR system. As the application of NMPC in embedded applications is a growing and relevant field, we develop a contribution consisting of two parts in Chapters 7-8. In the first part in Chapter 7, we use artificial neural networks to learn the optimal control policy for an ORC system. We find that the ANN controller is able to stabilize a superheat set-point even when the disturbances are outside the training set boundaries. However, since no guarantees exist that the ANN controller satisfies the constraints, we propose two methods that use a ML model of the optimal control policy as a starting point to find a good control policy at small computational cost in Chapter 8. The first method uses the ANN to initialize the NMPC algorithm. The idea is that providing a good initial guess will accelerate convergence to the optimal solution. The second method uses the ANN prediction and carries out a correction with the solution of a single quadratic program (QP), facilitating optimality and feasibility at small computational cost.
We conclude this thesis in Chapter 9 where we provide a summary of our findings. Furthermore, we outline promising avenues for further research.

Chapter 2

Literature review

In this chapter, we cover the scientific background required for this thesis. First, we review automotive waste heat recovery technology with a focus on WHR systems using an ORC to recover waste heat in Chapter 2.1. We then proceed to discuss dynamic optimization problems and solutions approaches with a focus on direct single shooting in Chapter 2.2, followed by an introduction to model predictive control in Chapter 2.3. We conclude this chapter with a presentation of machine learning with a focus on artificial neural networks, our machine learning method of choice in this thesis, in Chapter 2.4. More specific literature reviews regarding the contributions of this thesis are provided in the introductions of the respective chapters.

2.1 Automotive waste heat recovery

While the passenger vehicle market is beginning a transition away from vehicles with ICEs towards zero-emission propulsion technology, most notably battery electric vehicles, a similar trend cannot yet be observed for HD vehicles [19]. Here, diesel engines are expected to be the dominant propulsion technology for the foreseeable future [29]. However, manufacturers are facing ever increasing environmental regulations and pressure from customers to reduce operational cost, both of which provides incentive to improve fuel efficiency [19].
Besides a plethora of technologies that aim at directly improving engine efficiency [19], WHR is a promising technology to increase fuel efficiency [30]. It is motivated by the fact that only about 40 % of fuel energy are converted to propulsion energy [20] and the rest is discharged to the environment as "waste heat". Waste heat streams are the tailpipe exhaust gas, the exhaust gas recirculation (EGR), the coolant, the charge air

cooling system and the lubricating oil [31]. Among these, the tailpipe exhaust gas and EGR are most attractive for WHR [32, 33, 34]. In [32], the authors assessed the available heat sources from an energy and an exergy perspective. They found that the engine coolant, while having the second highest energy content, was unattractive due to its relatively low temperature.
A variety of technologies is considered for WHR in automotive application [19]. The most significant are

- turbocompounding (either mechanical or electrical),
- thermoelectric generators,
- organic Rankine cycles.

We will discuss these technologies in the following sections. In accordance with the focus of this thesis, we will limit ourselves to a brief overview of turbocompounding and thermoelectric generators and emphasize the background on ORCs.

2.1.1 Turbocompounding

Turbocompounding is based on the expansion of the tailpipe exhaust gas, similar to turbocharging [35]. It can be distinguished into mechanical turbocompounding and electrical turbocompounding. In mechanical turbocompounding, an additional turbine is placed behind the turbocharger turbine in the exhaust gas stream. The generated mechanical power is directly transmitted to the engine crankshaft. In electrical turbocompounding, more mechanical power is generated from expanding the exhaust gas in the turbocharger than is required for compressing the engine air and the difference is fed to an electric generator. The advantage of both approaches, compared to ORCs, is their simplicity as much less additional equipment is required. However, the amount of power that can be produced is limited and expected reductions in fuel consumption are in the range of 5 %.

2.1.2 Thermoelectric generators

Thermoelectric generators (TEG) [36] recover energy based on the Seebeck effect with semiconductor materials. Two cells of n-type and p-type are electrically connected in sequence and thermally connected in parallel. Connecting one side of the system to a hot source and the other side to a cold sink causes a flow of electrical current which then can be utilized. The advantages of TEGs are that the system, unlike turbo compounding or ORCs, does not contain any moving parts or potentially dangerous fluids

[37]. However, available materials are limited to moderately high temperatures and overheating has to be prevented when used for automotive waste heat recovery. The efficiency of TEGs is further limited as electron transport also results in undesired heat transport, reducing the thermal potential [36]. Even for state-of-the-art materials, e.g., bismuth telluride, TEGs only achieve about 20% of the Carnot efficiency for the relevant range of operating conditions [38]. The efficiency of TEGs is commonly evaluated through the figure of merit ZT where T is the average temperature of the considered system and Z is defined as

$$Z = \frac{\alpha^2 \sigma}{\lambda} \tag{2.1}$$

where α is the Seebeck coefficient, σ is the electrical conductivity and λ is the thermal conductivity. The value for ZT in established materials and temperature conditions ranges around approximately 1 [36, 39] and an increase to a value of 1.2 would be required for WHR in vehicles to be competitive [36].
TEGs have been investigated as means to recover waste heat by major automotive companies and several contributions present mathematical models and experimental setups [40, 39, 41, 34, 42]. The nominal power among the mentioned systems is below 1 kW. The reported potential fuel savings are in the range of 3%. As TEGs are also associated with high cost, the technology is currently not competitive for WHR in vehicles.

2.1.3 Organic Rankine cycles

The ORC is a power cycle that converts thermal energy into mechanical energy. In contrast to the classic steam Rankine cycle, organic working fluids (WF) are used. ORCs are adequate for utilizing low to medium grade heat sources. Thus, they have been investigated for a variety of applications including primary power generation from geothermal [43] and solar thermal heat sources [44]. Furthermore, the technology is attractive for waste heat recovery in industrial [22] and transport applications [45]. Beside vehicles, suitable applications in the transport sector are ships [46] and diesel trains [47]. The two latter applications hold some advantages over application in road vehicles. Longer periods of steady-state operation occur, the exhaust gas conditions can be predicted and weight and space constraints are less significant than in HD trucks. Thanks to the wide range of potential applications, the technology has become very popular and a great body of work, including a textbook [48], exists. In accordance with the focus of this thesis, we will put emphasis on the area of automotive waste heat recovery using ORCs. We will briefly discuss the thermodynamic principles of

ORCs and various design aspects before we discuss ORC systems that were specifically proposed for WHR in vehicles operated in street traffic.

2.1.3.1 Working principle

The ORC is a thermodynamic power cycle, presented in its most basic form with a T-s diagram in Fig. 2.1. The process consists of the following steps. The subcooled

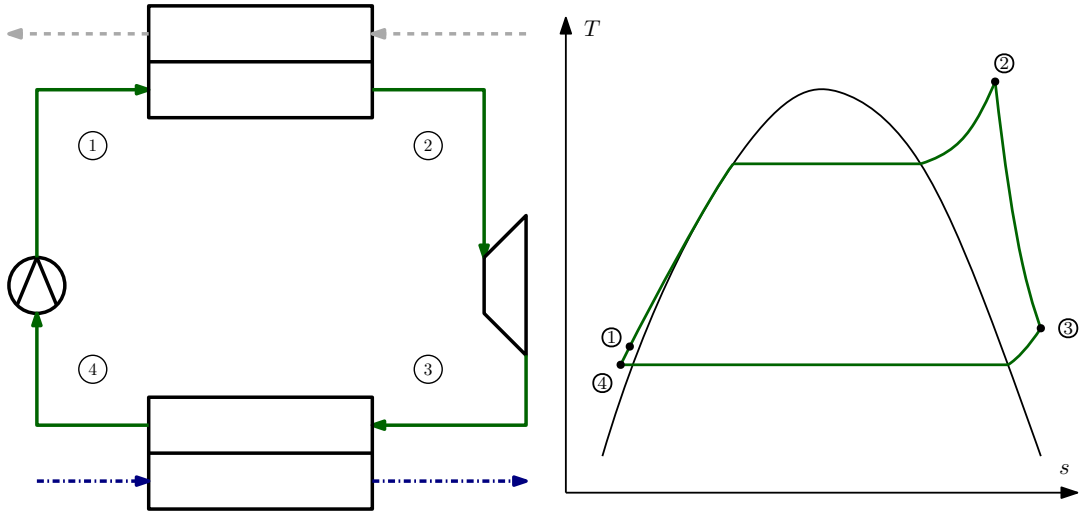

(a) Flowsheet of basic ORC configuration

(b) T-s diagram

Figure 2.1: Sketch of a basic ORC and corresponding T-s diagram. The WF is represented by the green solid lines, the heat source is represented by the gray dashed lines and the coolant is represented by the blue dash-dotted lines.

WF is pressurized in a pump ④→①. Then it is preheated, evaporated and eventually superheated in one or more heat exchangers where thermal energy is extracted from the heat source ①→②. Next, it is expanded in an expansion machine (e.g., a turbine) which produces mechanical power ②→③. This expansion machine can be coupled to a generator so that the ORC system provides electric power or the mechanical power can be used directly, e.g., by connecting the expansion machine to an engine crankshaft. In a final step, the WF is cooled down in a condenser to subcooled state in order to prevent cavitation in the pump ③→④.
Working fluids are commonly grouped according to their behavior during expansion. WFs with negative slope in the T-s diagram are termed wet fluids, those with positive slope are termed dry fluids and those with near-infinite slope are termed isentropic fluids [49]. Dry and isentropic WFs hold the advantage over wet WFs that no superheating is necessary. For wet WFs (cf. Fig. 2.1b), superheating is required to avoid

droplet formation during expansion which can lead to significant damage in a turbine [31].

2.1.3.2 Literature review on proposed automotive WHR systems

Here, we provide a brief overview of ORC systems for automotive WHR. More specific literature reviews with regard to ORC modeling, operation and control are provided throughout the introductions of Chapters 3-6.
In contrast to stationary applications, ORCs operated in vehicles have to be lightweight, cheap and of small size. Furthermore, the transient nature of the heat source makes operation challenging [50]. Nevertheless, when compared to turbocompounding and TEGs, ORC systems for waste heat recovery in vehicles are considered to be a relatively mature and competitive technology [30, 50]. Research reaches back into the 1970s where an initial system was proposed in the wake of the 1973 oil crisis [19]. The subject was sparsely investigated throughout the 1980s and 1990s but has experienced renewed interest from the late 2000s on [30]. More recent reviews can be found in [51, 31, 50]. The review in [31] focuses on an assessment of the available heat sources in HD trucks. In contrast, the review in [51] focuses on a variety of suitable vehicle types for WHR and their respective engine operation profiles. Finally, in [50] many aspects ranging from system design to proposed control structures are covered. The authors note the discrepancy between the predicted power outputs in simulation studies and realized experimental systems. These raise concerns regarding estimates on potential fuel savings which vary between 5 % and 10 % [30, 51]. Concurrently to this thesis, Katharina Eichler develops a holistic simulation toolchain for ORC simulation in vehicles [52]. The work is complementary as [52] focuses on providing methods to develop an ORC system from an early conceptual stage to application on a test rig, whereas this thesis focuses on deriving optimal operating policies and control strategies for a specific system based on numerical optimization. In this section, we first discuss possible system architectures, the choice of which mostly depends on the choice of heat source followed by a brief discussion on common expander and heat exchanger types. Finally, we touch on methods for choosing an adequate WF.

System architecture A variety of system architectures have been proposed in literature. Albeit ORC systems for WHR are mostly proposed for heavy-duty vehicles, applications to passenger vehicles exist, in particular in earlier contributions [53, 54, 55, 56, 57]. The number of employed heat sources has a strong impact on possible architectures. As discussed before, the most suitable heat sources are the ex-

haust tailpipe gas and the EGR. Thus, most proposed systems either use the exhaust tailpipe gas only or both, the tailpipe exhaust gas and EGR. Reviews on the resulting configuration and their respective advantages can be found in [58, 59, 50]. When only the tailpipe exhaust gas is chosen as heat source, a single heat exchanger is typically used to achieve compact packaging [59] but exceptions exist [60]. In case both the tailpipe exhaust gas as well as the ERG are employed as heat sources, a serial or a parallel configuration is possible. The serial configuration simplifies the control task but is also associated with a lower efficiency [59].
Some authors suggested more uncommon power cycle setups, e.g., the Kalina cycle or a transcritical cycle [61]. A recent review on further modified ORC structures for automotive WHR can be found in [62]. Herein, we consider a basic ORC process as presented in Fig. 2.1. The rationale for this choice is the low capital expense and structural simplicity of this process.

Expanders Two types of expansion machines, volumetric expanders and turbines, are commonly used [50]. Volumetric expanders operate at relatively low rotational speeds and have a fixed displacement volume. In contrast, turbines operate at a high rotational speed and the mass flow is not influenced by the rotational speed in supersonic operation [63]. The system considered herein uses a turbine.
Expanders can either produce mechanical power by coupling them directly with the drivetrain or produce electrical power by coupling them with a generator. Direct coupling with the drivetrain requires a gearbox due to the differences in rotational speed. Due to the high rotational speeds, higher transmission losses can be expected for turbines [50]. Generally, mechanical coupling removes the expander rotational speed as a degree of freedom which means that the expander will likely operate at a suboptimal speed. Electrical coupling preserves the rotational speed as a degree of freedom. However, it requires the integration of an additional electric system, which is associated with high investment cost, and the conversion and reconversion of energy, which is associated with losses in efficiency. A clear advantage of volumetric expanders is that they can operate with vapor-liquid mixtures, while these have to be avoided in turbines in order to prevent damage. For further information, the reader is referred to [64] for a discussion of expander choice in small-scale ORC system generally and to [65] for discussions concerning automotive WHR specifically.

Heat exchangers Either shell-and-tube heat exchangers or plate-and-fin heat exchangers are used [50]. Plate-and-fin heat exchangers can typically be built with smaller volume but tend to be heavier than shell-and-tube heat exchangers. An in-

depth review is provided in [66]. The heat exchangers considered herein are of plate-and-fin type. The design target for the heat exchangers is to provide a large heat exchange area at little volume and weight. However, a high heat exchanger weight is associated with high thermal inertia, buffering WF temperature fluctuation and, thus, simplifying the control task [50]. This observation motivated the use of a thermal buffer system in [67].

Working fluids Many factors have to be considered when choosing an adequate working fluid. Besides thermodynamic properties, relevant criteria include flammability, toxicity and global warming potential [31]. Great care is required as the choice of working fluid also affects other design decisions, e.g., the required heat transfer area [50]. WFs can be either pure substances or zeotropic mixtures of components with different boiling points. The latter can be exploited to achieve higher second law efficiencies. An overview of WF selection for ORCs in general is provided in [68]. Publications considering optimal WF choice include [49, 69, 70] and the choice of WF mixtures is discussed in [71, 72, 73, 74]. Occasionally, dynamic models were used to account for part-load conditions [75]. For automotive WHR, a variety of publications compare different working fluids, mixtures or even try to design novel molecules. Simulation-based screenings are carried out in [76, 77]. A working fluid screening typically consists of a pre-screening step where working fluids are removed from the considered set based on undesired thermodynamic properties. This is followed by a second step where a considered system is simulated with the various fluids. Optimization-based strategies for WF selection are employed in [78, 79, 80]. In [78], the cycle is optimized with global optimization for each candidate fluid. In [80, 79] fluid design is considered. The authors account for transient heat source with operating point clustering in [80] and a simplified dynamic model in [79].

2.2 Dynamic optimization

A focus of this thesis is to find optimal operating policies for an ORC system using numerical optimization. Due to operation in street traffic, optimal operation is strongly influenced by the transient exhaust gas conditions. Furthermore, the ORC system exhibits significant thermal inertia (mostly due to the HX metal walls). These factors require the use of a dynamic model to adequately describe system operation in street traffic. As a consequence, when we want to optimize ORC operation, we have to consider this dynamic model in our optimization problem. This gives rise to dynamic optimization problems which are commonly encountered in chemical engineering and

other disciplines [23].

2.2.1 Problem formulation

We consider dynamic optimization problems of the following type

$$\min_{\boldsymbol{u}(t)} \quad \Phi\left(\boldsymbol{x}\left(t_f\right)\right) \tag{2.2a}$$

$$\text{s.t.} \quad \boldsymbol{M}\dot{\boldsymbol{x}}\left(t\right) = \boldsymbol{f}\left(\boldsymbol{x}\left(t\right), \boldsymbol{y}\left(t\right), \boldsymbol{u}\left(t\right), \boldsymbol{d}\left(t\right), \boldsymbol{p}\right) \qquad \forall t \in [t_0, t_f] \tag{2.2b}$$

$$\boldsymbol{0} = \boldsymbol{g}\left(\boldsymbol{x}\left(t\right), \boldsymbol{y}\left(t\right), \boldsymbol{u}\left(t\right), \boldsymbol{d}\left(t\right), \boldsymbol{p}\right) \qquad \forall t \in [t_0, t_f] \tag{2.2c}$$

$$\boldsymbol{x}\left(t_0\right) = \boldsymbol{x}_0 \tag{2.2d}$$

$$\boldsymbol{0} \geq \boldsymbol{h}\left(\boldsymbol{x}\left(t\right), \boldsymbol{y}\left(t\right), \boldsymbol{u}\left(t\right), \boldsymbol{d}\left(t\right), \boldsymbol{p}\right) \qquad \forall t \in [t_0, t_f] \tag{2.2e}$$

$$\boldsymbol{u}_{min} \leq \boldsymbol{u}\left(t\right) \leq \boldsymbol{u}_{max} \qquad \forall t \in [t_0, t_f] \tag{2.2f}$$

where Φ is a Mayer-type objective function evaluated at final time t_f. Note that Lagrange-type or Bolza-type objective functions can easily be rewritten as Mayer-type objective function, thus, our formulation remains generally applicable. The differential equations are described by the vector-valued function $\boldsymbol{f}$ in (2.2b) and the algebraic equations are described by the vector valued function $\boldsymbol{g}$ in (2.2c) where $\boldsymbol{M}$ is a constant mass matrix, $\boldsymbol{x}$ are the differential variables, $\boldsymbol{y}$ the algebraic variables, $\boldsymbol{u}$ are the inputs to the system that can be manipulated, $\boldsymbol{d}$ are the disturbances, i.e., inputs to the system which cannot be manipulated and $\boldsymbol{p}$ are time-invariant parameters. The initial conditions at t_0 are described by $\boldsymbol{x}_0$ (2.2d). The optimization problem is subject to the inequality path constraints described by $\boldsymbol{h}$ (2.2e) and the inputs are box-constrained in (2.2f).

2.2.2 Solution approaches

As time is continuous, the inputs and constraints in (2.2a)-(2.2f) are of infinite dimension. Practically, we are interested in a sufficiently fine approximation of this problem. Methods to solve dynamic optimization problems are of either of the following categories [23].

1. Indirect methods
2. Direct methods

Indirect methods aim at finding a solution which satisfies the necessary conditions of optimality through solving a boundary value problem. They are also referred to as

"optimize then discretize" methods [23]. As we use direct methods in this thesis, we refrain from further discussion and refer the reader to [23, 81].

Direct methods Direct methods first reduce the problem to finite dimension by discretization and then solve the resulting finite-dimensional optimization problem. Depending on which quantities are discretized, direct approaches can be further categorized as sequential [82] and simultaneous methods [83] or multiple shooting [84]. In simultaneous methods, all variables are discretized and the states are obtained by approximation, e.g., with a Runge-Kutta scheme [23]. The resulting nonlinear program (NLP) is typically sparse and can be solved with readily available solvers such as, e.g., IPOPT [85]. The sequential method, also referred to as single shooting, only discretizes the control variables by control vector parameterization. This results in a much smaller dense NLP. Multiple shooting is a hybrid between the aforementioned methods. In addition to discretizing the controls, the states are discretized at a few shooting knots. Continuity of the final solution is enforced through additional constraints in the NLP. The method holds advantages over single shooting for unstable or strongly nonlinear systems and can easily be parallelized. However, the additional constraints complicate the NLP. In the following, we provide additional detail on single shooting as our method of choice in this thesis.

Single shooting Single shooting is based on splitting the two tasks of solving the differential-algebraic equations (DAE) model and optimizing the controls. Here, the control vector is discretized using control vector parameterization. The input function is thereby split into time intervals and represented by B-splines parameterized with coefficients which become the new degrees of freedom of the optimal control problem [86].

$$\boldsymbol{u}_i\left(t\right) = \sum_{j}^{n_\phi} c_{i,j}\phi_{i,j}\left(t\right) \tag{2.3}$$

where $c_{i,j}$ are the coefficients and $\phi_{i,j}$ the B-splines. A piece-wise constant parameterization is the most simple and concurrently most commonly used parameterization [86]. However, continuous control parameterizations can hold advantages when applied to process equipment. In addition to the degrees of freedom, the constraints have to be considered. These are typically evaluated on a grid. In principle, this allows for intermediate violations of the constraints, however, these are rarely relevant given that an adequate grid is chosen. In case avoiding any constraint violation is deemed necessary, algorithms to guarantee constraint satisfaction exist [87, 88].

The resulting NLP reads

$$\min_{\boldsymbol{c}} \quad \varphi(\boldsymbol{c}, \boldsymbol{p}) \tag{2.4a}$$

$$\text{s. t.} \quad \mathbf{0} = \boldsymbol{g}(\boldsymbol{c}, \boldsymbol{p}) \tag{2.4b}$$

$$\mathbf{0} \geq \boldsymbol{h}(\boldsymbol{c}, \boldsymbol{p}) \tag{2.4c}$$

where $\boldsymbol{c}$ is the concatenation of all control vectors parameters $c_{i,j}$ and $\boldsymbol{p}$ is a vector of quantities in which the problem is parametric. In our case, it includes the initial state $\boldsymbol{x}_0$ and the disturbances $\boldsymbol{d}$.
Typically, a sequential quadratic programming method, e.g., SNOPT [89] is used to solve the dense NLP. In the single shooting algorithm, the NLP solver and a DAE integrator are called in an alternating fashion. The integrator solves the DAE equation system with the current control profile and computes state values and sensitivities. The sensitivities can be obtained integrating the sensitivity system or solving the adjoint equations [23]. Single shooting holds advantages over simultaneous methods for stiff systems, as state-of-the-art integrators with variable step length control can easily be employed. It has, however, disadvantages for unstable systems.

2.3 Model predictive control

Model predicitve control (MPC) [90] is an advanced control method. The working principle is illustrated in Fig. 2.2. The basic idea is to use a process model to predict the evolution of the considered system given an input vector. This model is used in an optimization problem to minimize a given cost function while respecting specified constraints. While input constraints generally represent physical limits, constraints on states are typically desirables and often realized through soft constraints [90]. The problem is solved on a limited horizon called the prediction horizon consisting of N_P intervals of duration Δt_C in order to limit computational demand. The controls are varied on a control horizon of length $N_C \leq N_P$ after which they are held constant. The result of the optimization is an optimal input trajectory. Unless we consider a batch problem, we would like to use an infinite horizon to achieve optimal and stable operation. However, for practical reasons we have to use a finite horizon [91]. For a variety of reasons, the calculated input trajectory is not fully applied to the plant. First, due to plant-model mismatch the model predictions will not be equal to the plant response. Second, unexpected disturbances might arise during the prediction horizon. Third, the finite horizon solution might be a bad approximation of the infinite horizon solution. Thus, only the first input signal of the trajectory is sent

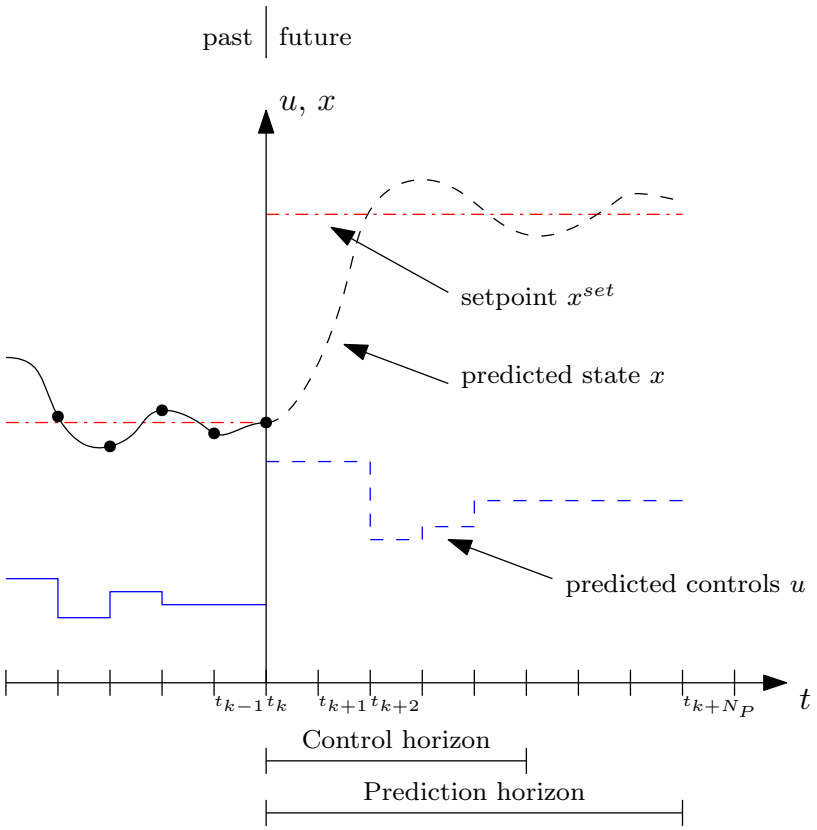

Figure 2.2: Illustration of the working principle of model predictive control (adapted from [91]). Based on the current measurements, an optimal control problem with prediction horizon N_P is solved. The resulting open-loop control trajectory is applied to the plant until the problem is re-solved in order to provide feedback.

to the plant and the model is re-solved after one sampling interval Δt_S to introduce feedback. Therefore, the closed-loop trajectory can differ significantly from the open-loop trajectory, especially when a short prediction horizon is chosen. The main perks of MPC are [92]

- handling of multiple-input-multiple-output (MIMO) systems,
- consideration of input and state constraints,
- disturbances can be considered,
- prediction of future plant behavior.

Depending on the model equations and objective function, MPC can be categorized as linear model predictive control (LMPC), nonlinear model predictive control (NMPC)

or economic nonlinear model predictive control (eNMPC). These subcategories are briefly discussed in the following.

2.3.1 Linear model predictive control

Linear model predictive control (LMPC) problems use a quadratic objective function, a linear model and linear constraints. Typically the objective function aims at tracking a predefined setpoint while penalizing control action.

$$\begin{aligned}\Phi\left(t\right) = \int_{t_0}^{t_f} &\left(\boldsymbol{x}\left(t\right) - \boldsymbol{x}^{\boldsymbol{des}}\right)^T \boldsymbol{Q}\left(\boldsymbol{x}\left(t\right) - \boldsymbol{x}^{\boldsymbol{des}}\right) + \left(\boldsymbol{u}\left(t\right) - \boldsymbol{u}^{\boldsymbol{des}}\right)^T \boldsymbol{R}\left(\boldsymbol{u}\left(t\right) - \boldsymbol{u}^{\boldsymbol{des}}\right) \mathrm{d}t \\ &+ \left(\boldsymbol{x}\left(t_f\right) - \boldsymbol{x}^{\boldsymbol{des}}\right)^T \boldsymbol{P}\left(\boldsymbol{x}\left(t_f\right) - \boldsymbol{x}^{\boldsymbol{des}}\right) \end{aligned} \tag{2.5}$$

where $\boldsymbol{Q}$ and $\boldsymbol{R}$ and $\boldsymbol{P}$ are positive definite weighting matrices. An additional term penalizing incremental change in the controls can be added to prevent drastic control action. Since a linear model is used, the method only works well in the vicinity of the corresponding operating point. However, as linear models can be easily identified for operational plants, e.g., through step response, it is the predominant method in industry [92]. Historically, large-scale chemical plants have been operated at a fixed operating point and the main focus of the controller was disturbance rejection. With increasing penetration of intermittent renewable energies, however, this operational paradigm might change [93].

2.3.2 Nonlinear model predictive control and economic nonlinear model predictive control

LMPC might not be appropriate, i.e., it might lead to suboptimal or even infeasible closed-loop behavior, when the controlled system exhibits a strongly nonlinear behavior or is operated flexibly as opposed to operation at a fixed operating point. Nonlinear model predictive control (NMPC) has been extensively researched since the 1990s [91], which, to some extent, has been driven by the increasing combination of the scheduling and supervisory control layers in the automation hierarchy [94]. In NMPC, either the model or constraints are nonlinear or the objective function is non-quadratic or both. In each instance of NMPC a dynamic optimization problem (2.2a)-(2.2f) has to be solved and the methods mentioned in Chapter 2.2 can be employed. Solving NMPC problems is much more computationally expensive than solving LMPC problems. Although nonlinear identification methods exist, a drawback that impairs the widespread application of NMPC is that, often, the model has to be developed by hand. A good

overview of the developments in the field is provided in [95]. In the 1990s and early 2000s, most of the works focused on guaranteeing stability for NMPC [91]. Common approaches for this use terminal region constraints and terminal penalty terms in the objective function [96, 91]. More recently, approaches that do not require a terminal constraint have been developed [97]. Another significant focus in research in recent years was on handling uncertainty, which can occur due to measurement noise, state estimation or uncertain model parameters [95]. Rigorous approaches to the problem can guarantee constraint satisfaction (e.g., [98]). However, these methods often result in an overly conservative control policy. Thus, methods that offer a compromise (e.g., [99]) have been proposed.
Traditionally, the NMPC controller serves as supervisory controller that maintains a setpoint. This would typically be specified by the upper layer of the automation hierarchy and aim at profitable operation. However, the most profitable operation of a plant might not always correspond to operating at a fixed point [100]. Furthermore, a regulatory objective function might not choose the most economical transition from one operating point to another. These considerations motivate economic nonlinear model predictive control (eNMPC) [24]. Here, an objective function reflective of the process economics is chosen. This objective function is typically not quadratic and positive definite with respect to an optimal steady state, allowing for transient operation [24]. Thus, the objective function does not satisfy the assumptions of standard stability proofs and requires special stability theory [95]. However, the approaches are similar in that they use ideas like terminal constraints or a quasi-infinite horizon. For an overview, we refer the reader to [24].

2.3.3 Fast-update methods

As NMPC problems are expensive to solve, the associated feedback delay can severely deteriorate control performance for many application. To remedy this problem, so-called fast-update methods have been proposed. An overview of such methods is provided in [26]. The methods make use of the fact that the discretized NMPC optimization problem (2.4a)-(2.4c) is parametric in $\boldsymbol{p}$. The aim of these methods is to follow an optimal solution trajectory $\boldsymbol{c}^{opt}(\boldsymbol{p})$. Fast-update methods can be subdivided into sensitivity-based update methods and suboptimal update methods [26]. Methods from the first category use a linear approximation of the KKT conditions to construct an update step. Methods from the latter category approximate the NMPC solution by performing a limited number of iterations. The QP we solve in one of our methods in Chapter 8 is inspired by these methods (Neighboring extremal updates [101, 102]).

2.4 Machine learning

Machine learning (ML) refers to a variety of methods that aim at inferring knowledge from data [103]. They have in common that data is used for training in the hope that the trained ML model is able to make adequate predictions when presented with data not encountered in training, i.e., it is able to generalize. ML tasks can be classified into regression tasks and classification tasks. Regression tasks, e.g., predicting reaction rates as a function of species concentration, typically operate on a continuous output domain. Classification tasks, e.g., assessing whether sensor data is corrupted or not, operates on a discrete output domain. In this thesis, we restrict ourselves to the discussion of regression tasks. A plethora of methods is available and the reader is referred to introductory literature for an overview [103]. In the following, we introduce artificial neural networks (ANN) which is our ML model of choice. We choose ANNs because of their easy applicability with available software and good generalization capabilities [104].

2.4.1 Artificial neural networks

An ANN is a ML model that is inspired by the workings of neural networks in organisms [105]. It consists of a network of interconnected artificial neurons. The original idea of using artificial neurons as computing units was developed by McCulloch and Pitts [106] in 1943.
A seminal finding is that ANNs are universal approximators, i.e., they can learn any smooth function on a compact subset of $\mathbb{R}^n$ to arbitrary precision [107, 108]. The most commonly used artificial neural network is the multilayer feedforward neural network, often also referred to as a multilayer perceptron. A sketch of a feedforward neural network is depicted in Fig. 2.3. It provides a mapping from the input to the output space by propagating information through an input layer, at least one hidden layer and one output layer. Although, a great variety of further ANN-types exists, we will limit the discussion to multilayer feedforward ANNs as they are sufficient for the regression tasks considered in this work. ANNs with a single hidden layer are commonly referred to as shallow ANNs and ANNs with multiple hidden layers are referred to as deep ANNs. The hidden layer consists of artificial neurons and the number of neurons in each layer as well as the number of hidden layers are degrees of freedom in ANN design. A sketch of a single neuron is depicted in Fig 2.4. The inputs to the neurons are received from the previous layer and are multiplied with their respective weights w_{ij}, summed up with the bias b_j and then evaluated by the

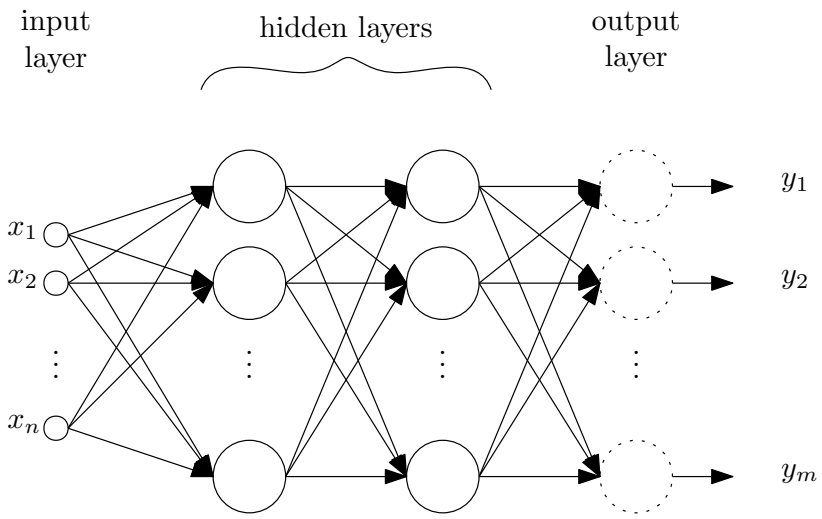

Figure 2.3: A fully connected feedforward artificial neural network. Hidden layer neurons are indicated by solid circles and output layer neurons by dashed circles. For clarity of presentation, biases and weights are not shown.

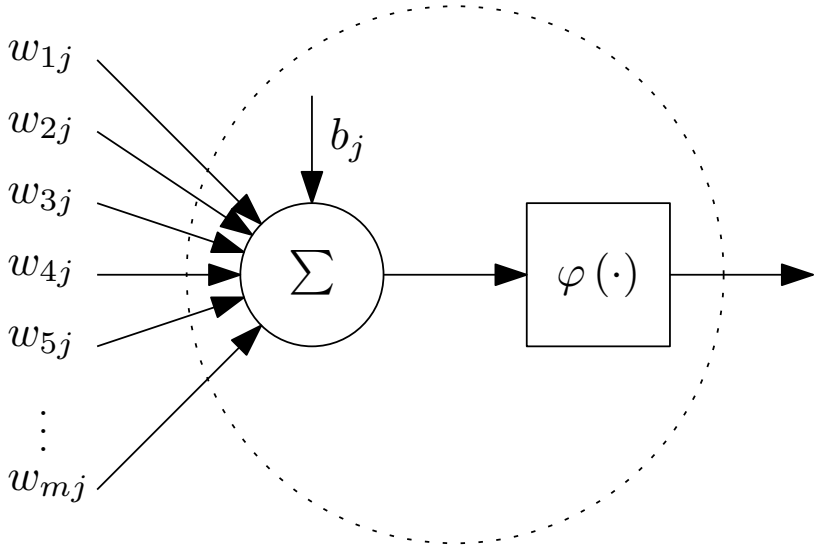

Figure 2.4: A single neuron (adapted from [105]). The inputs to the neuron are weighted and summed up with the bias and the result is evaluated by the activation function φ.

activation function φ. The output of neuron j is given by

$$y_j = \varphi\left(\sum_{i \in N_i} w_{ij} x_i + b_j\right) \tag{2.6}$$

A variety of activation functions can be used. Typical choices are sigmoid functions (e.g., hyperbolic tangent) and threshold functions (e.g., signum function). Recently the rectified linear unit (ReLU) activation function has been used extensively. It shows superior learning results [109], in particular in deep networks. Furthermore, it is less prone to the vanishing gradient problem [110] than other activation functions. In the final layer (output layer) the number of neurons is equal to the number of outputs and often a linear activation function is used. With the basic network structure established, we can now discuss how an ANN is trained, i.e., how adequate values for weights and biases are identified from data.
The training task is to find values for the weights and biases such that the ANN, when provided with the input data, minimizes a given loss function of its predicted output and the output data. The most common loss function for regression tasks is the mean squared error (MSE). Training is performed by optimization, often with stochastic gradient descent. The gradient of the objective function can be determined by the backpropagation algorithm [105]. The training problem is known to exhibit multiple minima [104]. However, it was observed that, given sufficient data is available and an adequate ANN architecture is chosen, good performance can be obtained from most training results [109]. A further issue during training is the danger of over- and underfitting (bias/variance dilemma) [111]. A common remedy, also used in this thesis, is early stopping. The data is split into a training set, a validation set and a test set. Training is stopped after a number of training steps with increases in the loss function on the validation set to prevent overfitting.
After some initial success, a new wave of interest in ANNs arose through the advances in tasks such as digital image processing and text recognition using deep learning [109]. In chemical engineering, ANNs have been heavily researched in the 1990s and had established themselves as a method for a variety of application, e.g., fault detection [104]. Another widely investigated field in chemical engineering are hybrid models which combine first principle models with ANNs [112, 113]. Furthermore, ANNs have been used in process control which we discuss in the introduction of chapter 8. The recent success of deep learning in text and image recognition has ignited new hope that artificial intelligence can significantly advance chemical engineering, although it is unclear whether all the novel methods developed in computer science are useful in chemical engineering tasks [114]. For example, the use of deep learning requires great amount of data which are normally not available in chemical engineering applications unless the data is generated by simulation [114]. Examples of this can be found in [115], where the physical properties of a WF are represented with an ANN and in [27], where the optimal control policy of a NMPC controller is represented by an ANN.

Chapter 3

Development and validation of an ORC model

3.1 Introduction

In this chapter, we develop a dynamic model of an ORC for WHR in a diesel truck that is suitable for optimization. To obtain a model that is valid over a broad range of operating conditions, we estimate model parameters using transient data obtained from a test rig. To enable parameter estimation via dynamic optimization, the thermodynamic formulation necessary for the calculation of the WF properties [116] is directly implemented in the model. Further, we introduce generic heat transfer correlations that can be parameterized without detailed knowledge about the heat exchanger (HX) geometry. This approach of estimating parameters with transient data on an ORC system for waste heat recovery has so far not been reported in literature and promises to provide a more accurate prediction of transients. In order to demonstrate the effectiveness of the approach, we validate the model with a simulation using input data from the World Harmonized Transient Cycle (WHTC), which exhibits strongly transient exhaust gas conditions.

Since HD trucks are operated in street traffic, the ORC system is subject to significant fluctuation in its heat source. Therefore, the dynamic system behavior is of high relevance. In [117], it was found that during transient operation less than half of the design point efficiency could be achieved. Thus, we focus on dynamic modeling of the ORC in this Chapter.

When building a dynamic model, it has to be decided which dynamic effects have to be considered and which can be assumed to be quasi-stationary on the timescale of

interest. In accordance with the findings in literature, we use dynamic models for the HXs, as the most significant dynamics of an ORC are observed there [118], while the pump and the turbine are represented with pseudo-steady-state models.
Dynamic modeling of HXs has received significant attention, especially with regard to control system design [119]. The two most common approaches are either discretization using the finite volume (FV) method or the implementation of a moving boundary (MB) model. While historically a trade-off between more accurate FV models and computationally less expensive MB models was assumed to exist, recent publications have questioned this notion [120, 119, 121, 122]. It was found that, with a sufficient number of finite volumes, both approaches can achieve similar accuracies. Under such conditions, a smaller computational effort for the MB approach is required, which explains its popularity in model-based control applications [123]. For further reduction of computational demand, often linearized models derived from either type are employed [124, 125, 126, 127] or physically motivated simplifications are used [47]. As the computational effort can be crucial in dynamic optimization, we choose the MB approach.
An extensive description of MB models can be found in [28], where many important aspects regarding the implementation are discussed. In contrast to discretization with the FV method, the MB approach in its initial formulation can not handle the appearance or disappearance of phases that is associated with start-up and shutdown of the system and can also occur during operation. This particular shortcoming and attempts to overcome it have been subject of several publications [128, 129, 130, 131, 132, 133, 134].
While many publications dealing with details of dynamic HX modeling are available, relatively few contributions report full ORC models for WHR. In the majority of publications on full ORC models, HXs are modeled with the FV method [135, 136, 137, 138]. In [139], both HX modeling approaches are presented. In [138] an ORC model for a heavy duty diesel truck implemented in Simulink is presented. Most of these publications obtain thermodynamic properties of the WF from look-up tables or databases connected through an interface. Another option is presented in [135], where polynomials that are valid in certain intervals are fitted to the data.
We extend the findings in literature by providing a dynamic parameter estimation procedure. To allow for this, we embed the fundamental equation of state in the model. Further, we introduce flexible heat transfer correlations that do not require precise knowledge of the HX geometry. Finally, we present an extensive parameter estimation and model validation using experimental data representative of street traffic conditions.
The remainder of this chapter is structured as follows: In Chapter 3.2, we introduce

the topology of the considered system, followed by a description of the implemented models in Chapter 3.3. We describe the parameter estimation in detail in Chapter 3.4 and its results are discussed in Chapter 3.5, together with a validation using input data of different experiments. Finally, we draw conclusions in Chapter 3.6.

3.2 System topology

A schematic representation of the considered system is depicted in Fig. 3.1. The sys-

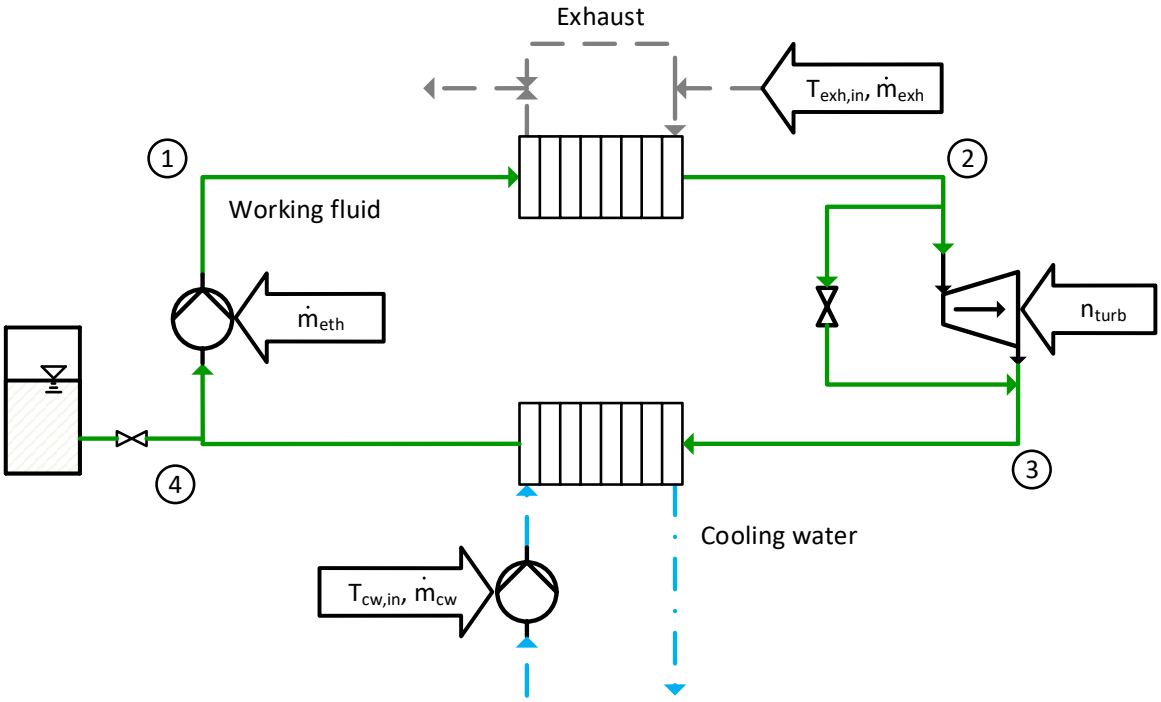

Figure 3.1: System topology of the ORC test rig including the exhaust pipe (grey, dashed), the WF cycle (green, solid), and cooling water (blue, dash-dot). Circled numbers mark the states of the working fluid. Disturbances and control inputs, which are recorded during experiments, are labeled within arrows.

tem is a basic ORC configuration as discussed in Chapter 2.1.3. The input variables to the system are the exhaust gas mass flow and inlet temperature $\dot{m}_{exh}$, $T_{exh,in}$, the CW mass flow and inlet temperature $\dot{m}_{CW}$, $T_{CW,in}$ and the WF mass flow $\dot{m}_{WF}$ and turbine speed n_{turb}.
The WF leaves the evaporator as superheated vapor ("nominal operation"), as sub-cooled liquid or as two-phase fluid, depending on the amount of heat transferred from

the exhaust gas to the system. In the latter cases, the turbine bypass valve is opened in order to avoid droplet erosion in the turbine during expansion, thus no power is generated. Also, in case of insufficient cooling capacity, the amount of heat transferred into the system can be reduced by opening the exhaust gas bypass valve. In this Chapter, we only consider the nominal transient operation mode where the WF is not expanded into the two-phase region. Furthermore, all available exhaust gas is passed through the evaporator. A liquid storage tank is installed in the system in order to be able to control the total WF volume in the cycle. The valve to the storage tank can be opened during start-up/shutdown which maintains the condenser pressure at ambient pressure and can be closed when the desired amount of WF in the cycle is reached.

3.3 Dynamic ORC model

In the following, we describe all implemented dynamic models representing the ORC system. The model is implemented in the equation-based modeling environment gPROMS [140], which, in addition to providing numerical solvers for DAE-systems, offers the possibility to perform parameter estimation and solve dynamic optimization problems.

3.3.1 Heat exchanger model using the moving boundary approach

We model the HXs (evaporator, condenser) with the MB approach where, instead of discretizing in the spatial domain along a grid with fixed cell volumes, the fluid volume is discretized in zones according to the fluid's aggregate state. Given an evaporator, in which subcooled fluid is fed and superheated vapor exits (vice versa for the condenser), the model consists of three zones. This case is illustrated in Fig. 3.2.
The quantities at the zone interfaces using the indexes 0 and 2 are in fact saturation quantities in the presence of all zones. However, to maintain generality, we use the notation where two additional differential quantities, the specific enthalpies h_0 and h_2, are added to the model, as compared to the most common formulation [28]. This allows the model to be easily extendable to simulate non-nominal conditions, where not all zones are present and h_0 or h_2 might be the outlet enthalpy [132]. For each zone, we formulate a lumped mass and energy balance. The differential quantities characterizing the WF are pressure p and enthalpy h at the zone boundaries. The HX wall is divided according to the zone lengths of the WF and an energy balance is derived for each wall element. During simulations, the zones move along the evaporator

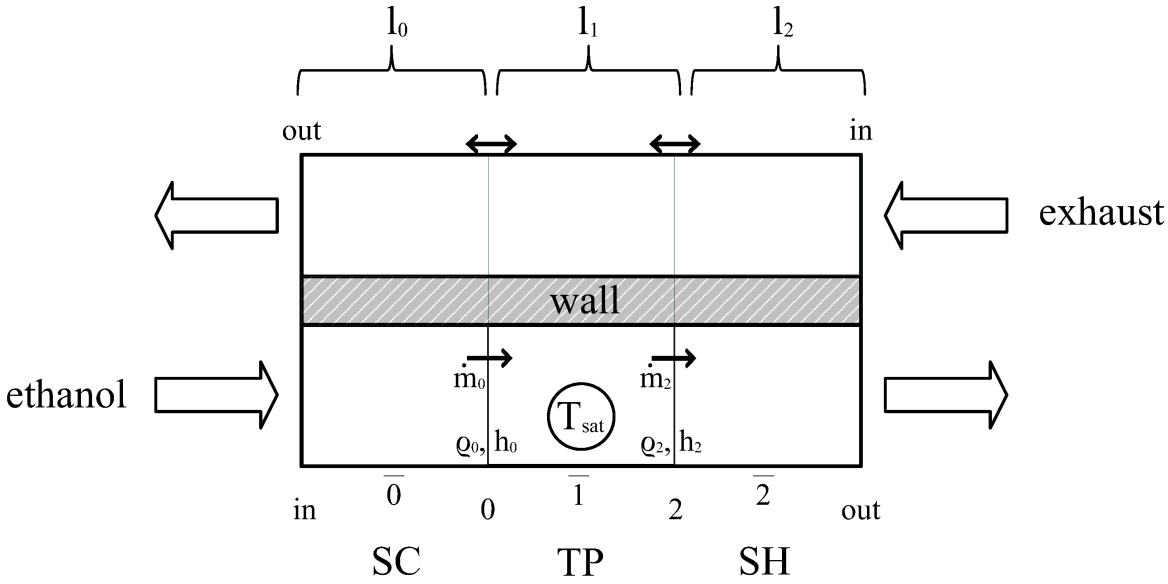

Figure 3.2: Application of the moving boundary approach to the counter-current evaporator in the nominal case. Numbers represent the discretized zones (subcooled, two-phase, superheated) respectively their boundaries.

length. The secondary side is modeled quasi-stationary, as the exhaust gas or cooling water normally have lower residence times in the HX and no phase change occurs [28]. The HX is a counter-current plate heat exchanger with multiple fluid channels. For simplicity, the channels are not modeled separately. Instead, we assume that only one rectangular channel per fluid and one single separating wall exists. For this assumption to be valid, the flow conditions in the separate channels must all be similar. This simplification of the geometry is expected to contribute to the prediction error.
In order to derive the MB model equations, we make a number of assumptions, namely

- averaged thermodynamic state variables for each zone (enthalpy, density),
- spatially uniform pressure over the complete HX length (momentum balance can be omitted),
- constant cross sectional fluid flow area,
- no axial heat conduction in WF or wall,
- homogeneous equilibrium two-phase flow, and
- quasi-stationary behavior on the secondary sides (exhaust, CW).

These assumptions are typically made for the implementation of the MB approach in literature ([28, 119, 130]) and are applied when deriving the following equations.

3.3.1.1 Governing differential equations

For the sake of brevity, we present the equations in the final form that is implemented in the model, rather than discussing their derivation. A detailed derivation of all of the following equations in this section can be found in [132].
For control volumes with single-phase flow, we get the following mass (3.1) and energy (3.2) balances

$$A\left(\left(z_a - z_b\right)\frac{\mathrm{d}\bar{\rho}}{\mathrm{d}t} + \bar{\rho}\frac{\mathrm{d}\left(z_b - z_a\right)}{\mathrm{d}t}\right) + \rho_a A\frac{\mathrm{d}z_a}{\mathrm{d}t} - \rho_b A\frac{\mathrm{d}z_b}{\mathrm{d}t} = \dot{m}_a - \dot{m}_b, \tag{3.1}$$

$$\begin{aligned} A\left(\left(z_b - z_a\right)\bar{\rho}\frac{\mathrm{d}\bar{h}}{\mathrm{d}t} + \left(z_b - z_a\right)\bar{h}\frac{\mathrm{d}\bar{\rho}}{\mathrm{d}t} + \bar{\rho}\bar{h}\frac{\mathrm{d}\left(z_b - z_a\right)}{\mathrm{d}t}\right) - A\left(z_b - z_a\right)\frac{\mathrm{d}p}{\mathrm{d}t} \\ +\rho_a h_a A\frac{\mathrm{d}z_a}{\mathrm{d}t} - \rho_b h_b A\frac{\mathrm{d}z_b}{\mathrm{d}t} = \dot{m}_a h_a - \dot{m}_b h_b + b_{WF}\alpha_{WF}\left(z_b - z_a\right)\left(T_w - \bar{T}\right), \end{aligned} \tag{3.2}$$

where A is the cross-sectional area of the fluid channel and z is the longitudinal coordinate. ρ, T and $\dot{m}$ are density, temperature and mass flow of the WF, where the subscripts a and b indicate quantities of the left-hand and right-hand boundary of the zones and the overline indicates averaged quantities. t is the time, b_{WF} the width of the fluid channel and α_{WF} is the heat transfer coefficient from WF to the wall. The last term on the right hand side of (3.2) is the heat flow from the wall into the WF. As $\bar{\rho}$ and $\bar{h}$ are algebraic quantities, we account for their time dependence by constructing their total differential w.r.t. the differential quantities (3.3) and (3.4) and inserting them into (3.1) and (3.2), in order to obtain formulations, where only actual differential quantities appear in time derivatives.

$$\frac{\mathrm{d}\bar{\rho}}{\mathrm{d}t} = \frac{\partial\bar{\rho}}{\partial p}\frac{\mathrm{d}p}{\mathrm{d}t} + \frac{\partial\bar{\rho}}{\partial\bar{h}}\frac{\mathrm{d}\bar{h}}{\mathrm{d}t} \tag{3.3}$$

$$\frac{\mathrm{d}\bar{h}}{\mathrm{d}t} = \frac{1}{2}\left(\frac{\mathrm{d}h_a}{\mathrm{d}t} + \frac{\mathrm{d}h_b}{\mathrm{d}t}\right) \tag{3.4}$$

For the two-phase zone, the mass (3.5) and energy (3.6) balances are

$$\begin{aligned} A\Big(\left(\bar{\gamma}\rho'' + \left(1-\bar{\gamma}\right)\rho'\right)\frac{\mathrm{d}\left(z_b - z_a\right)}{\mathrm{d}t} + \left(z_b - z_a\right)\Big(\frac{\mathrm{d}\bar{\gamma}}{\mathrm{d}t}\left(\rho'' - \rho'\right) \\ +\bar{\gamma}\frac{\partial\rho''}{\partial p}\frac{\mathrm{d}p}{\mathrm{d}t} + \left(1-\bar{\gamma}\right)\frac{\partial\rho'}{\partial p}\frac{\mathrm{d}p}{\mathrm{d}t}\Big)\Big) + \rho_a A\frac{\mathrm{d}z_a}{\mathrm{d}t} - \rho_b A\frac{\mathrm{d}z_b}{\mathrm{d}t} = \dot{m}_a - \dot{m}_b, \end{aligned} \tag{3.5}$$

$$A\Big(\frac{\mathrm{d}\left(z_b - z_a\right)}{\mathrm{d}t}\left(\bar{\gamma}\rho''h'' + \left(1-\bar{\gamma}\right)\rho'h'\right) + \left(z_b - z_a\right)\Big(\frac{\mathrm{d}\bar{\gamma}}{\mathrm{d}t}\left(\rho''h'' - \rho'h'\right)$$

$$+\bar{\gamma}h''\frac{\mathrm{d}\rho''}{\mathrm{d}p}\frac{\mathrm{d}p}{\mathrm{d}t}+(1-\bar{\gamma})\,h'\frac{\mathrm{d}\rho'}{\mathrm{d}p}\frac{\mathrm{d}p}{\mathrm{d}t}+\bar{\gamma}\rho''\frac{\mathrm{d}h''}{\mathrm{d}p}\frac{\mathrm{d}p}{\mathrm{d}t}+(1-\bar{\gamma})\,\rho'\frac{\mathrm{d}h'}{\mathrm{d}p}\frac{\mathrm{d}p}{\mathrm{d}t}\Big)\Big)$$
$$-A\,(z_b-z_a)\,\frac{\mathrm{d}p}{\mathrm{d}t}+A\rho_a h_a\frac{\mathrm{d}z_a}{\mathrm{d}t}-A\rho_b h_b\frac{\mathrm{d}z_b}{\mathrm{d}t}$$
$$=\dot{m}_a h_a-\dot{m}_b h_b+b_{WF}\alpha_{WF}\,(z_b-z_a)\left(T_w-\bar{T}\right), \tag{3.6}$$

where $\bar{\gamma}$ is the average void fraction calculated with (3.7) and the superscripts $'$ and $''$ indicate quantities at liquid and vapor saturation respectively. The time derivative of the average void fraction can be expressed by constructing the total differential w.r.t. the differential quantities (3.8).

$$\bar{\gamma}=\frac{\rho'}{(h_0-h_2)\,(\rho'-\rho'')^2}\Bigg\{(h_0-h_2)\,\rho'+\rho''\Bigg[h_2-h_0$$
$$+(h'-h'')\ln\left(\frac{\rho''\,(h''-h_0)}{\rho'\,(h_2-h')}\right)\Bigg]\Bigg\} \tag{3.7}$$

$$\frac{\mathrm{d}\bar{\gamma}}{\mathrm{d}t}=\frac{\partial\bar{\gamma}}{\partial h_0}\frac{\mathrm{d}h_0}{\mathrm{d}t}+\frac{\partial\bar{\gamma}}{\partial h_2}\frac{\mathrm{d}h_2}{\mathrm{d}t}+\frac{\partial\bar{\gamma}}{\partial p}\frac{\mathrm{d}p}{\mathrm{d}t} \tag{3.8}$$

Under nominal operating conditions, the HX model consists of two single-phase control volumes and one two-phase control volume, which are combined as can be seen in Fig. 3.2. The mapping of the zone boundary positions to the zone lengths l_i is given in Tab. 3.1. The energy balance for each wall zone (3.9) reads,

Table 3.1: Mapping of zone boundary positions (cf. Fig 3.2) and zone lengths [28].

	z_a	z_b	$\frac{\mathrm{d}z_a}{\mathrm{d}t}$	$\frac{\mathrm{d}z_b}{\mathrm{d}t}$
0	0	l_0	0	$\frac{\mathrm{d}l_0}{\mathrm{d}t}$
1	l_0	l_0+l_1	$\frac{\mathrm{d}l_0}{\mathrm{d}t}$	$\frac{\mathrm{d}(l_0+l_1)}{\mathrm{d}t}$
2	l_0+l_1	l	$\frac{\mathrm{d}(l_0+l_1)}{\mathrm{d}t}$	0

$$A_w\rho_w c_{p_w}\left(l_i\frac{\mathrm{d}T_{w_i}}{\mathrm{d}t}+\left(T_{w,B_{i,i-1}}-T_{w_i}\right)\frac{\mathrm{d}z_{a,i}}{\mathrm{d}t}+\left(T_{w_i}-T_{w,B_{i,i+1}}\right)\frac{\mathrm{d}z_{b,i}}{\mathrm{d}t}\right)$$
$$=\dot{Q}_{exh_i}-b_{WF}\alpha_{WF,i}l_i\left(T_{w_i}-\bar{T}_i\right)-\alpha_{amb}p_{evap}l_i\left(T_{w_i}-T_{amb}\right), \tag{3.9}$$

where A_w, ρ_w and c_{p_w} are the wall cross-sectional area, density and heat capacity. T_{w_i} is the temperature of the respective wall zone and $T_{w,B_{i,i-1}}$ and $T_{w,B_{i,i+1}}$ are the

wall temperatures at the left- and right-hand boundary of the zone, which are calculated using a length-weighted average, as suggested in [130]. $\dot{Q}_{exh_i}$ is the amount of heat transfered from the exhaust gas to the wall, b_{WF} is the WF channel width and α_i the heat transfer coefficient for the WF in the respective zone. We introduce a term accounting for heat loss from the exchanger wall to the environment, in which α_{amb} is the heat transfer coefficient, p_{evap} the HX perimeter and T_{amb} the ambient temperature.

3.3.1.2 Thermodynamic model of the working fluid

We implemented a suitable thermodynamic formulation for the WF ethanol in form of a fundamental equation of state based on the free Helmholtz energy [141, 116]. A major advantage of this formulation is the availability of analytical derivatives for all important derivatives required for the MB model. The analytical expressions for the derivatives can be found in [142]. Saturation properties are calculated from auxiliary equations which can be found in [116].

3.3.1.3 Exhaust temperature calculations

By analytical integration of the quasi-stationary energy balance on the exhaust side from interface $i+1$ to interface i assuming static one dimensional flow [131] (Fig. 3.3), the temperature at the end of one element can be calculated as in (3.10) and the heat transfered to the wall as in (3.11). Both the exhaust heat capacity c_{p,exh_i} and the heat

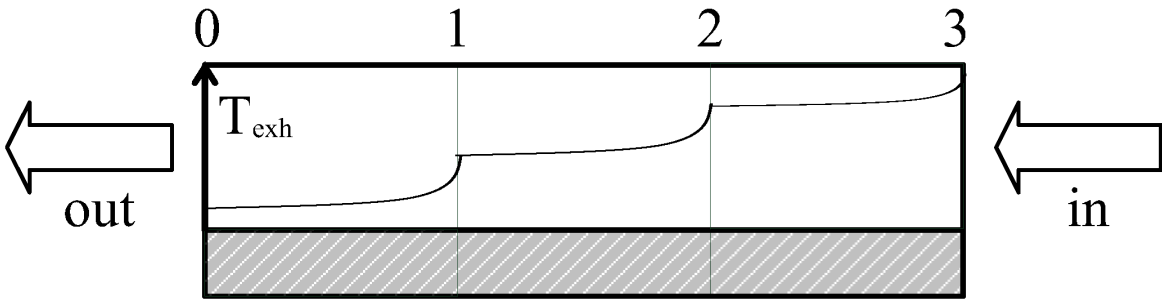

Figure 3.3: Illustration of the qualitative temperature distribution assumed for the exhaust gas in the evaporator.

transfer coefficient α_{exh_i} are assumed constant over one element. $\dot{m}_{exh}$, T_{exh} and b_{exh} are mass flow, temperature and width of the exhaust channel.

$$T_{exh_i} = T_{w_i} + \left(T_{exh_{i+1}} - T_{w_i}\right) \exp\left(-\frac{\alpha_{exh_i} b_{exh}}{\dot{m}_{exh} c_{p,exh_i}} l_i\right), \quad i \in [0, 2] \tag{3.10}$$

$$\dot{Q}_{exh_i} = \dot{m}_{exh} c_{p,exh_i} \left(T_{exh_{i+1}} - T_{exh_i} \right) \tag{3.11}$$

3.3.1.4 Heat transfer correlations

The dynamic behavior of the HX model is significantly influenced by the chosen heat transfer correlations. In literature, correlations of varying complexity, ranging from fixed heat transfer coefficients [137] to elaborate Nusselt correlations [55], can be found. While fixing the heat transfer coefficients reduces computational effort, it can be expected to deteriorate the model accuracy. Nusselt correlations, which are based on similarity theory, promise high accuracy, but require detailed knowledge about the HX geometry. As a compromise, we decided to introduce generic correlations for the calculation of all heat transfer correlations, where the influences of mass flow and temperature on the heat transfer coefficient can be captured without detailed information on geometry. An additional advantage of this approach is that finding adequate bounds on the parameters to be estimated is rather simple. A similar approach has been used in [135]. For all three sections of the evaporator, we choose the same generic functional approach, as given in (3.12), for the WF heat transfer coefficients.

$$\alpha_{i,WF,evap} = \alpha_{i,0,evap} \cdot \left[(1 - k_i) \cdot \left(\frac{\dot{m}}{\dot{m}_0} \right)^{c_{i,1,evap}} + k_i \cdot \left(\frac{\dot{m}}{\dot{m}_0} \right)^{c_{i,2,evap}} \right] + d_{i,evap} \tag{3.12}$$

The approach assumes the heat transfer coefficient to depend on the WF mass flow rate. It is scaled using a maximum mass flow rate $\dot{m}_0$ to ensure the scaled value ranges between zero and one. $\alpha_{i,0}$ and d_i in (3.12) represent a base coefficient and an additional factor. While the exponent $c_{i,1}$ is bounded between zero and one, the exponent $c_{i,2}$ is bounded to be greater than one. To allow for the dominance of one exponent within a region of low or high mass flow, we use the logistic function k_i as an activation function, as shown in (3.13):

$$k_i = \frac{1}{1 + \exp\left(\frac{\dot{m} - e_i}{\dot{m}_0 \cdot f_i} \right)} \tag{3.13}$$

The parameters e_i and f_i are used to determine the mass flow rate at which the logistic function switches and how fast this switch occurs. While this functional approach offers great flexibility and a wide range of behaviors can be captured, six parameters per zone are added to the parameter estimation problem.
For the heat transfer in the condenser and the exhaust gas heat transfer coefficient, we use the comparable, yet slightly different correlations (3.14) and (3.15), where the subscripts *cond* and *exh* represent the values of the WF in the condenser and the

exhaust gas.

$$\alpha_{i,WF,cond} = \alpha_{i,0,cond} \cdot \left(\frac{\dot{m}_{WF}}{\dot{m}_{WF,0}}\right)^{c_{i,1,cond}} \cdot \left(\frac{T_{i,WF,in}}{T_{WF,0}}\right)^{c_{i,2,cond}} + d_{i,cond} \tag{3.14}$$

$$\alpha_{i,exh} = \alpha_{exh,0} \cdot \left(\frac{\dot{m}_{exh}}{\dot{m}_{exh,0}}\right)^{c_{exh,1}} \cdot \left(\frac{T_{i,exh,in}}{T_{exh,0}}\right)^{c_{exh,2}} + d_{exh} \tag{3.15}$$

In addition to the mass flow rate, they also depend on the respective temperature $T_{WF/exh,0}$. Again, the temperature is normalized by the maximum permissible temperature in the HX.
For calculating the heat transfer coefficient of the CW in the condenser, we employ a simple approach, where the CW mass flow $\dot{m}_{CW}$ is the independent variable, i.e.,

$$\alpha_{CW} = \alpha_{CW,0} \cdot \left(\frac{\dot{m}_{CW}}{\dot{m}_{CW,0}}\right)^{c_{CW}} + d_{CW}. \tag{3.16}$$

The mass flow rate is once again normalized by the maximal CW mass flow.

3.3.2 De Laval's nozzle

An important variable that strongly influences the pressure in the evaporator and therefore most characteristics of the WF is its mass flow leaving the evaporator $\dot{m}_{evap,out}$. Its value can be determined by the implementation of a model for a de Laval's nozzle, which is placed within the turbine to convert thermal energy into kinetic energy. The nozzle is modeled similar to an orifice, thus can also be used for the turbine bypass.
We implemented a model based on the description in the VDI Wärmeatlas [143] and the previous work of Leung [144], assuming homogeneous flow equilibrium conditions. With the simplification of neglecting friction on the wall, $\dot{m}_{evap,out}$ is calculated from (3.17) - (3.19), in which C_d is the discharge coefficient, p_{HP} the high pressure level, ν_{in} the specific inlet volume, ψ the discharge function and A_{Laval} the smallest cross-sectional area of the Laval nozzle.

$$\dot{m}_{evap,out} = C_d \sqrt{2 \cdot \frac{p_{HP}}{\nu_{in}}} \cdot \psi \cdot A_{Laval} \tag{3.17}$$

$$\psi = \frac{\sqrt{(1-\eta_s) + \left(\omega \cdot \eta_s \cdot \ln\left(\frac{\eta_s}{\eta}\right) - (\omega - 1) \cdot (\eta_s - \eta)\right)}}{\omega \cdot \left(\frac{\eta_s}{\eta} - 1\right) + 1} \tag{3.18}$$

$$0 = \frac{(\omega^2 - 2 \cdot \omega + 1)}{2 \cdot \eta_s \cdot \omega} \cdot \eta_s^2 - 2 \cdot (\omega - 1) \cdot \eta_c + \omega \cdot \eta_s \cdot \ln\left(\frac{\eta_c}{\eta_s}\right) + \frac{3}{2} \cdot \omega \cdot \eta_s - 1 \quad (3.19)$$

The calculation of ψ in (3.18) depends on whether the flow is in choked state (reaching sonic velocity at A_{Laval}). This can be verified by calculating the critical flow pressure $p_{c,Laval}$ and comparing it to the low pressure level p_{LP}. In (3.18), the nondimensionalized pressures $\eta_c = \frac{p_c}{p_{HP}}$ and $\eta = \frac{p_1}{p_{HP}}$ are used. η_s is set to one [143]. Using this formulation, C_d is the only unknown parameter that can be determined in the parameter estimation.

3.3.3 Models for pump, turbine, piping and fluid tank

We model the pump assuming a fixed isentropic and mechanical efficiency ($\eta_{is,pump}$, $\eta_{mech,pump}$), according to (3.20). Within the model, we set both efficiencies to 0.9. Changes of either efficiency would have a minor impact on the system model, as the pump power P_{pump} is far smaller than that produced by the turbine P_{turb} and the effect of $\eta_{is,pump}$ on the WF outlet temperature is negligible. $h_{out,is}$ is the enthalpy of the WF in the case of an isentropic compression/expansion.

$$P_{pump} = \frac{1}{\eta_{mech,pump}} \cdot \dot{m}_{WF} \cdot \frac{h_{out,is} - h_{in}}{\eta_{is,pump}} \quad (3.20)$$

For the turbine, we use (3.21) to calculate the power output P_{turb}.

$$P_{turb} = \eta_{mech,turb} \cdot \dot{m}_{WF} \cdot \eta_{is,turb} \cdot (h_{in} - h_{out,is}) \quad (3.21)$$

For both the isentropic and mechanical efficiency ($\eta_{is,turb}$, $\eta_{mech,turb}$), a set of data points of the turbine efficiencies is available. Using this data, we create polynomial fits. The isentropic efficiency is a function of pressure ratio between high and low pressure and turbine speed. For this, we choose a polynomial function of third order with respect to pressure ratio and fifth order with respect to turbine speed. The mechanical efficiency, in contrast, is a function of turbine speed n (second order polynomial) and torque M (fifth order polynomial). Both polynomial functions reflect the measured data accurately, as shown in Tab. 3.2.

When comparing outlet and corresponding inlet temperatures of two sequential units in the ORC, it becomes obvious that it is necessary to account for heat losses in between. For this, we place pipe segments between each pair process units in the model. We model these pipes to track a stationary outlet temperature $T_{WF,out}^{stat}$ with a first-order delay behavior with the time-constant τ_{pipe}, i.e.,

$$\frac{\mathrm{d}T_{WF,out}}{\mathrm{d}t} = \frac{1}{\tau_{pipe,i}} \cdot \left(T_{WF,out}^{stat} - T_{WF,out}\right). \quad (3.22)$$

Table 3.2: Summary of the data fit for the isentropic and mechanical efficiency of the turbine, including validity range, size of data set and R^2-value of the fit. The subscript *scale* indicates a scaling value.

	Valid input range	Data set	R^2
η_{is}	$\frac{p_{HP}}{p_{LP}} \in [0, 40]$, $n_{turb} \in [0.636, 1.636] \cdot n_{scale}$	54	0.992
η_{mech}	$M_{turb} \in [0, 1] \cdot M_{scale}$, $n_{turb} \in [0.636, 1.636] \cdot n_{scale}$	192	0.995

The stationary outlet temperature of the WF $T^{stat}_{WF,out}$ is computed from (3.23), similar to (3.10). It is a function of ambient temperature T_{amb}, inlet temperature $T_{WF,in}$ and heat capacity flow $\dot{m}_{WF} \cdot c_{p,WF}$, assumed to be constant over the pipe segment. Furthermore, the heat transfer to the pipe wall is described by the factor $\alpha_{pipe} \cdot A_{pipe}$.

$$T^{stat}_{WF,out} = T_{amb} + (T_{WF,in} - T_{amb}) \cdot \exp\left(\frac{(\alpha_{pipe} \cdot A_{pipe})_i}{\dot{m}_{WF} \cdot c_{p,WF}}\right) \tag{3.23}$$

Both τ_{pipe} and $(\alpha_{pipe} \cdot A_{pipe})$ depend on the respective pipe segment and fluid state, thus are not known a priori. Therefore, they have to be estimated within the parameter estimation described in Chapter 3.4.
We did not implement a dynamic model including storage terms for the tank since no sensor signals for validation are available. Instead, we introduced an orifice, representing the connection to the tank, using (3.17) - (3.19). The tank is assumed to operate at atmospheric level. With an adequate cross-sectional area, it is possible to calculate the mass flow leaving the condenser in order to keep the pressure level constant.

3.4 Parameter estimation

The models of the units in the ORC described in Chapter 3.3 contain a large number of unknown parameters. These include parameters for the heat transfer correlations in the HXs and geometry parameters. As discussed in Chapter 3.1, few publications in the field of dynamic HX modeling present results of parameter estimation. In the rare cases where a parameter estimation is carried out, it is generally done with a steady-state model. This yields a NLP, which can be solved to minimize some least-squares criterion [145]. In [138], Nusselt correlations are extended with multipliers, which are separately optimized for various steady-state points using Particle Swarm Optimization. In [146], coefficients for heat transfer correlations, that are very similar to the ones introduced in Chapter 3.3.1.4, are estimated. However, the estimation is performed with a steady-state model and only base coefficients, that correspond

to α_0, are estimated. Parameter estimation based on data measured at steady-state points does not necessarily improve capturing the system's transient behavior.
To estimate the parameters using data measured under transient conditions means that the dynamic model has to be embedded in the parameter estimation problem, which results in a dynamic optimization problem (2.2a)-(2.2f). In case of a parameter estimation, however, the DOF are the fixed parameters $\boldsymbol{p}$ while the inputs $\boldsymbol{u}$ are those that were used during the experiment. The parameter estimation utility in gPROMS allows to perform dynamic parameter estimation using a Maximum Likelihood formulation by minimizing the objective function (3.24a) subject to the dynamic model, where data of j measured variables in i experiments, taken at k time points, are considered. $\boldsymbol{\xi}$ are the measured quantities. The sensor variances σ^2_{ijk} are assumed to have constant values of 2 K for temperature and 0.1 bar for pressure sensors. As we used a constant variances model, changes in the variance values correspond to a different weighting in the objective function between pressure and temperatures. Delays in the response of the sensors are neglected.

$$\min_{\boldsymbol{p}} \quad \sum_{i=1}^{NE} \sum_{j=1}^{NV_i} \sum_{k=1}^{NM_{ij}} \left[\frac{\left(\tilde{\xi}_{ijk} - \xi_{ijk} \right)^2}{\sigma^2_{ijk}} \right] \tag{3.24a}$$

$$\text{s.t.} \quad \text{(2.2b)-(2.2d)}$$

$$\boldsymbol{p}^{min} \leq \boldsymbol{p} \leq \boldsymbol{p}^{max} \tag{3.24b}$$

To solve the parameter estimation problem, the initial values for the differential quantities $\boldsymbol{x}_0$ have to be specified. However, the vector of differential variables contains quantities such as the wall temperatures and zone lengths that cannot be measured. To circumvent this issue, we assume the system to be in steady-state at the beginning of the experiment.

$$\boldsymbol{x}_0 = \boldsymbol{x}^{stat} \left(\boldsymbol{u}_0, \boldsymbol{p} \right) \tag{3.25}$$

The steady-state of the system $\boldsymbol{x}^{stat}$ is a function of the parameters to be estimated as indicated in (3.25). We derive the steady-state by simulation by simulating from an initial state with fixed inputs $\boldsymbol{u}_0$ for 5000 seconds before the first measurement is recorded. Depending on the chosen set of parameters, the simulation still can fail during the transient from the initial value to the steady-state associated with the parameter set, which might, in consequence, cut off some feasible solutions. Another issue associated with the method is that dynamic optimization problems typically have multiple minima, while we only employ a local solver. Hence, the quality of the solution depends on the chosen initial values of the parameters.

Fig. 3.4 shows the ORC topology including all relevant sensors and introduced pipe segments required for the parameter estimation and following model validation. We introduce five pipe segments according to the formulation presented in Chapter 3.3.3. The geometry of the evaporator and condenser have many uncertainties such as the

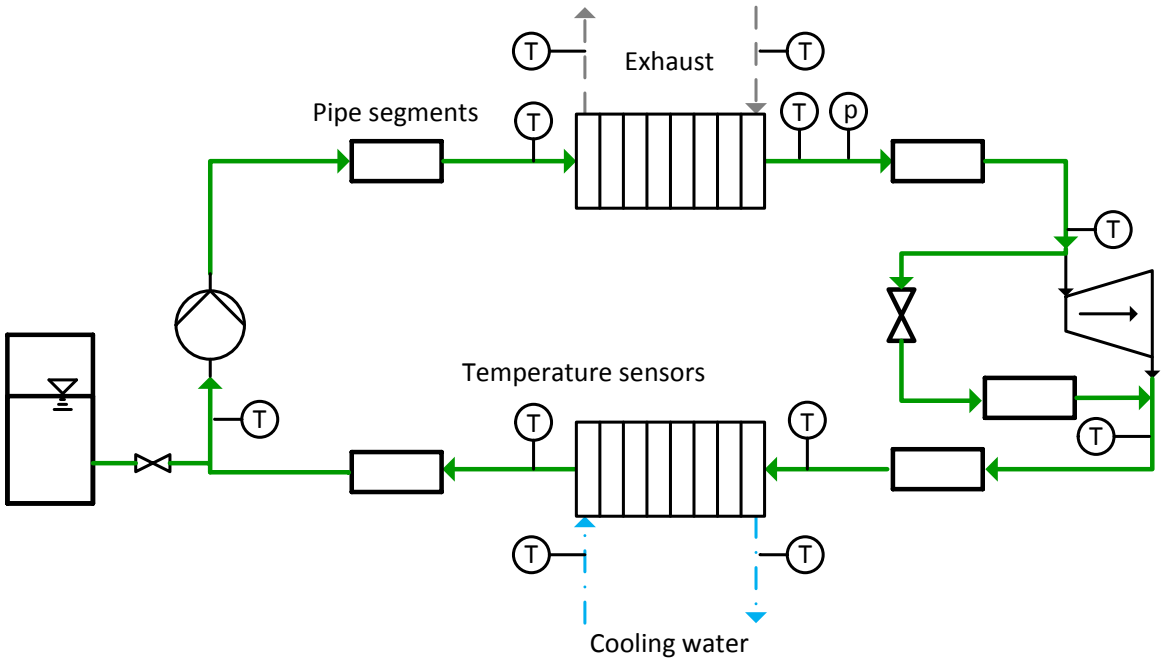

Figure 3.4: ORC topology for parameter estimation including pipe segments within the WF cycle. Temperature and pressure sensor positions are labeled in circles. The pipe segment in the bypass path is also accounting for losses in the expansion through the valve.

fluid flow areas, heat exchange areas, wall thicknesses etc., therefore several parameters have to be estimated here. Another important parameter is the discharge coefficient for the Laval nozzle in the turbine. Additionally, all coefficients for the heat transfer correlations introduced in (3.12) to (3.16) have to be estimated. As no sensor data of the ambient conditions during the measurement is available, we estimate the sink term with a constant heat transfer coefficient multiplied with the perimeter, together with an assumed ambient temperature.
The tables summarizing all estimated parameters together with their respective lower and upper bounds are given in Tab. A.1, A.2 and A.3.

3.5 Parameter estimation results and model validation

The results of the parameter estimation for the main ORC model components are presented in Chapter 3.5.1, followed by a validation of the full cycle model in Chapter 3.5.2 using measurement data from an experiment not incorporated in the previous parameter estimation. For confidentiality reasons, all signals are scaled. The parameter estimations results for the pipe model are provided in Appendix A. We use all pipe models together with their respective values for τ and $\alpha \cdot A$ within the validation of the ORC in the next section. Parameter values for the pipe models are given in Tab. A.1.

3.5.1 Parameter estimation results of the ORC model

We carry out the parameter estimation for the main parts of the ORC model, namely the evaporator and condenser, using transient measurement data from the test rig described in Chapter 3.2. As the storage tank valve after the condenser is open throughout the experiments, the low pressure of the ORC is nearly constant at around 1 bar. Therefore, the low pressure level is not taken into account for the objective function of this parameter estimation problem. For the measurements taken for the parameter estimation, the turbine in the test rig was bypassed using the expansion valve. As a result, we assume the superheated vapor to undergo an isenthalpic expansion to the low pressure level. To account for losses in the bypass, we introduce an additional pipe segment.
The input variables for one of the experiments included in the parameter estimation are depicted in Fig. 3.5. In this particular experiment, the response on steps in the WF mass flow is examined. Step changes in the mass flow to three different constant levels are applied, each of the steps corresponding to about 10 % change in mass flow. The simulation results obtained after the parameter estimation using the method described in Chapter 3.4, are shown together with the measurement data in Fig. 3.6. Although there is a bias between the simulated and measured data, the transient behavior caused by time-varying inputs is captured by the model, as the plots of the measured values show similar dynamics, e.g., in comparing the high pressure level to the WF mass flow.
To provide quantitative observations, we introduve four statistic indicators in (3.26) to (3.29): the maximal absolute deviation between the simulated result and measurement $\Delta\xi_{max}$, the maximal relative deviation $\Delta\xi_{max,rel}$, the absolute deviation averaged

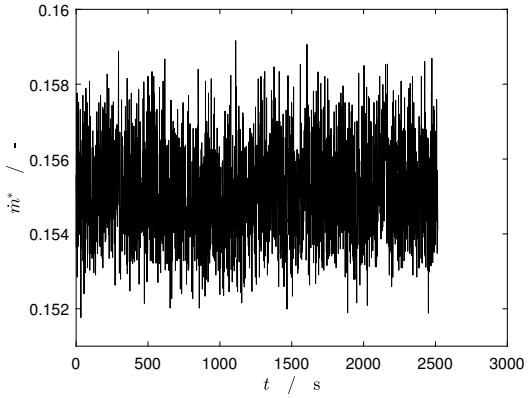

(a) Exhaust mass flow

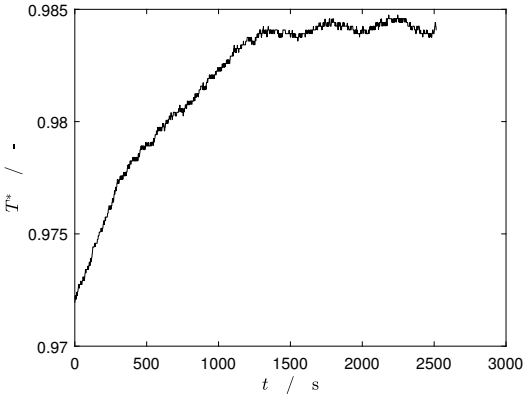

(b) Exhaust inlet temperature

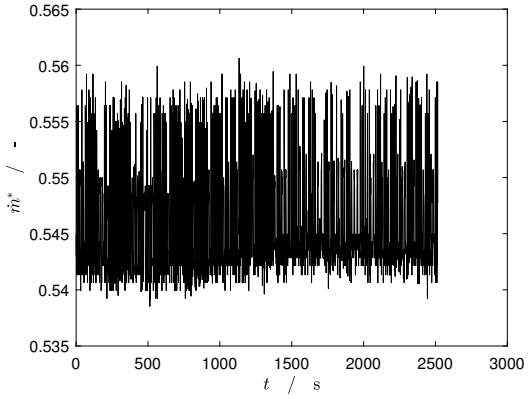

(c) CW mass flow

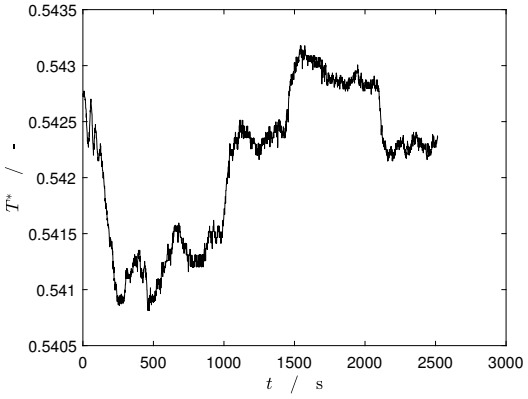

(d) CW inlet temperature

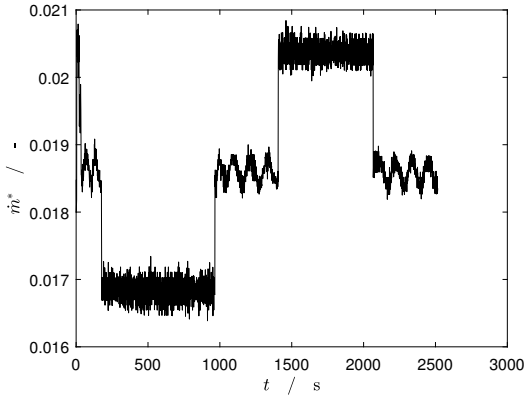

(e) Evaporator WF inlet mass flow

Figure 3.5: Trajectories of all input variables within a step-response experiment used for the parameter estimation.

over all samples $\Delta\bar{\xi}$ and the relative mean deviation $\Delta\bar{\xi}_{rel}$.

$$\Delta\xi_{max} = \max\left(\sqrt{\left[\tilde{\xi}_k - \xi_k\right]^2}\right), \quad k \in [0, k_{tot}] \tag{3.26}$$

$$\Delta\xi_{max,rel} = \max\left(\frac{\sqrt{\left[\tilde{\xi}_k - \xi_k\right]^2}}{\tilde{\xi}_k}\right), \quad k \in [0, k_{tot}] \tag{3.27}$$

$$\Delta\bar{\xi} = \frac{\sum_{k=0}^{k_{tot}}\left(\sqrt{\left[\tilde{\xi}_k - \xi_k\right]^2}\right)}{k_{tot}} \tag{3.28}$$

$$\Delta\bar{\xi}_{rel} = \frac{\sum_{k=0}^{k_{tot}}\left(\frac{\sqrt{\left[\tilde{\xi}_k - \xi_k\right]^2}}{\tilde{\xi}_k}\right)}{k_{tot}} \tag{3.29}$$

The values of these indicators for the presented case are summarized in Tab. 3.4. In general, the deviations are small with a maximum relative error of less than 4 % and a relative averaged error of less than 2 % for the temperatures. For the high pressure level, the mean relative error of 3 % supports the impression obtained from inspection of the plot in Fig. 3.6a, where the dynamics are captured appropriately.
The high pressure level of the system can be adequately predicted for steady-state points. It is predominantly influenced by the WF inlet mass flow into the evaporator as the steps in the inlet mass flow rate are qualitatively similar compared to the high pressure level. In the measurement data, after each step in the mass flow, the pressure shows a notable overshoot before it reaches a steady level. This overshoot is not appropriately captured by the model.
The remaining simulated output variables associated with the evaporator model also exhibit an acceptable representation of the measurements. The maximum deviation of the simulated WF evaporator outlet temperature is 10.2 K and the mean deviation is 3.7 K. The maximum and mean deviations of the exhaust gas outlet temperature are 4.6 K and 1.0 K respectively. In the condenser, a constant offset between the simulated outlet temperatures and the respective measurements is observed. This can be attributed to uncertainties in the geometry, heat transfer coefficients and heat capacity of the CW.
The resulting values of all parameters characterizing evaporator and condenser are given in Tab. A.2 and A.3. Quantitative measures of errors for direct comparison are rarely provided in literature. When comparing the errors found here to [139], where the deviation of the WF outlet temperature in the evaporator is at around 8 K, the

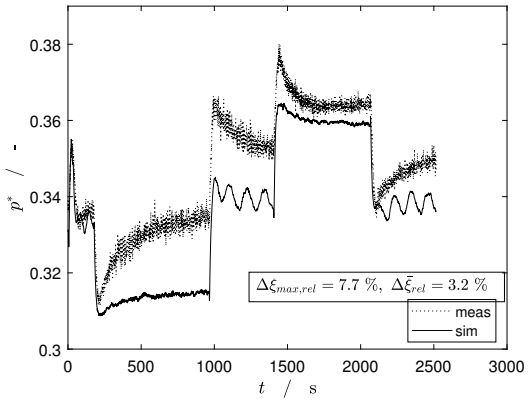

(a) Evaporator WF outlet pressure

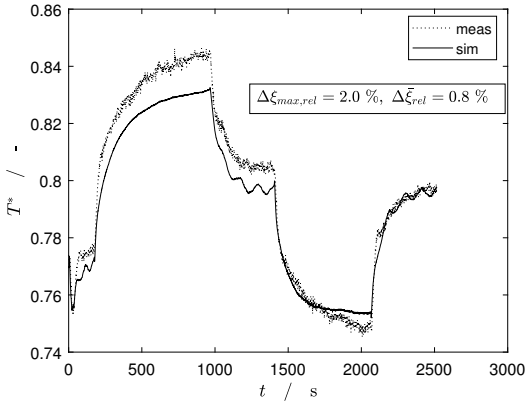

(b) Evaporator WF outlet temperature

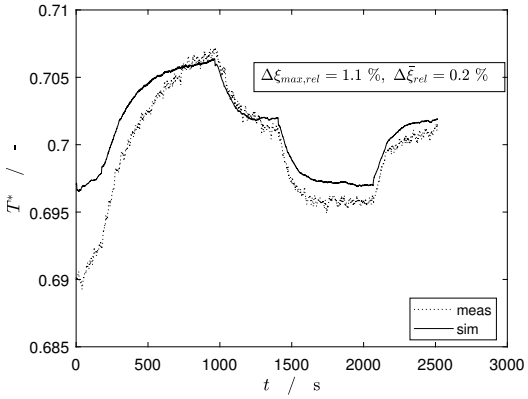

(c) Exhaust outlet temperature

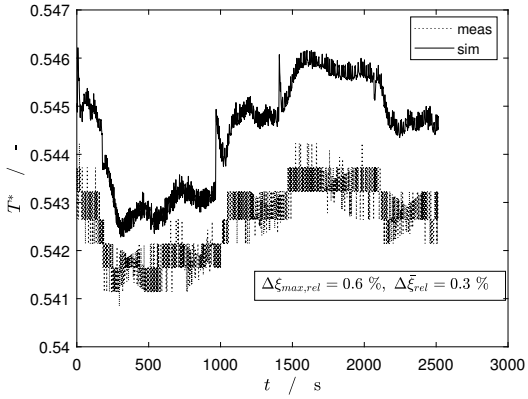

(d) Condenser WF outlet temperature

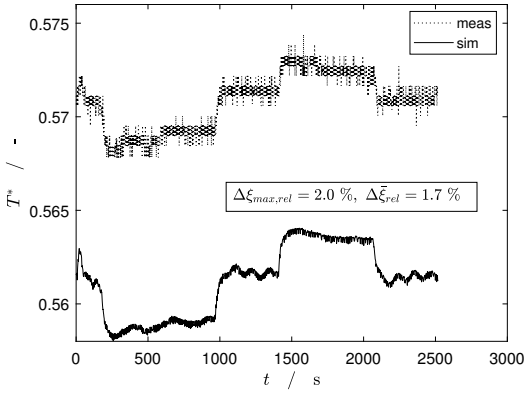

(e) CW outlet temperature

Figure 3.6: Simulated trajectories of relevant thermodynamic variables of the ORC in comparison to their corresponding measured trajectories in a measurement used for the parameter estimation, including maximal and mean relative errors.

Table 3.3: Summary of statistic error indicator values for relevant variables resulting from a measurement used for the parameter estimation.

	$\Delta\xi_{max}$ [bar]/[K]	$\Delta\xi_{max,rel}$ [%]	$\Delta\bar{\xi}$ [bar]/[K]	$\Delta\bar{\xi}_{rel}$ [%]
$p_{WF,evap,out}$	0.52	7.7	0.22	3.2
$T_{CW,cond,out}$	6.8	2.0	5.7	1.7
$T_{WF,cond,out}$	2.0	0.6	1.1	0.3
$T_{WF,evap,out}$	10.2	2.0	3.7	0.8
$T_{exh,evap,out}$	4.6	1.1	1.0	0.2

absolute average error here with 3.9 K for the measured value seems to be smaller. In general, a fair comparison of model accuracy is hardly possible as the system topology and scenarios vary from publication to publication. For example, in [138], comparable mean errors of $\Delta\bar{\xi}_{p_{HP},rel} = 2.2$ % and $\Delta\bar{\xi}_{T_{turb,in}} = 8$ K are reported, but this system includes a second evaporator in parallel, which also applies to [147, 148]. While [147] lists the errors for steady-state validation, the averaged errors in the dynamic validation are not provided. Compared to the errors given in [148] ($\Delta\bar{\xi}_{p_{HP},rel} = 12.4$ %, $\Delta\bar{\xi}_{h_{turb,in,rel}} = 5.4$ %), our proposed approach seems to be more accurate. In contrast, the relative errors reported in [120] are comparable small (< 5 % when using the MB approach). It has to be noted that the system is a vapor compression cycle operating at lower temperature and pressure levels.

3.5.2 Validation of the model

In order to validate the model, we performed simulations with inputs taken from an experiment not considered in the parameter estimation. For this experiment, parts of the World Harmonized Transient Cycle (WHTC) were taken as inputs, thus representing realistic data for the exhaust mass flow and inlet temperature in street traffic. The experiment was also executed with an open tank valve thus constant low pressure level. In contrast to the case used for the parameter estimation, the WF was expanded using the turbine. Hence, the turbine model described in Chapter 3.3.3 is used.
All model inputs are shown in Fig. 3.7. The exhaust gas mass flow exhibits strong fluctuations, as expected under real-world driving conditions, with the lowest value being 70 % smaller than the highest. However, the variations in the exhaust gas temperature are small.
Again, the simulated output variables of the evaporator are in good agreement with the measurements and the relative deviations are of the same magnitude as those

in the previous section (Tab. 3.4). Note that the simulated WF evaporator outlet temperature does not completely capture the dynamics measured in the system. The maximum deviation is three times higher than the deviation averaged over all sampling points. For the turbine outlet and condenser, the simulated values capture the dynamics of the measured temperatures properly, but deviate by an almost constant offset. Accordingly, the difference between the maximum absolute deviation $\Delta\xi_{max}$ and the mean absolute deviation $\Delta\bar{\xi}$ is comparatively small.

Table 3.4: Summary of statistic error indicator values for relevant variables resulting from the measurement used for the model validation.

	$\Delta\xi_{max}$ [bar]/[K]	$\Delta\xi_{max,rel}$ [%]	$\Delta\bar{\xi}$ [bar]/[K]	$\Delta\bar{\xi}_{rel}$ [%]
$p_{WF,evap,out}$	0.95	9.7	0.49	5.5
$T_{CW,cond,out}$	4.9	1.4	3.7	1.1
$T_{WF,cond,out}$	2.2	2.7	1.3	0.4
$T_{WF,evap,out}$	13.5	2.7	3.9	0.8
$T_{WF,turb,out}$	18.3	4.8	12.4	3.2
$T_{exh,evap,out}$	4.9	1.2	1.7	0.4

3.6 Conclusion

In this Chapter, we presented a dynamic model representing an ORC for waste heat recovery in a diesel truck. As the dominant transient phenomena can be observed in the HXs, we implemented dynamic models for the evaporator and condenser. More precisely, we chose the MB approach, one of two prominent approaches in dynamic HX modeling. The pump and expander are described with pseudo-steady-state models. To account for heat losses between components, we developed a simple pipe model. To facilitate the use of the ORC model for dynamic optimization, we implemented a fundamental thermodynamic equation based on the free Helmholtz energy. This holds the advantage that the sensitivities with respect to the optimization variables can be obtained directly by integrating the sensitivity system. To validate the model, we used transient measurement data and solved the arising dynamic optimization problem in gPROMS. Here, we used simple functional approaches instead of more complex Nusselt correlations for the calculation of the heat transfer coefficients.
The results of a validation study show that the ORC model is able to capture the relevant dynamics qualitatively as well as quantitatively, with a mean relative error

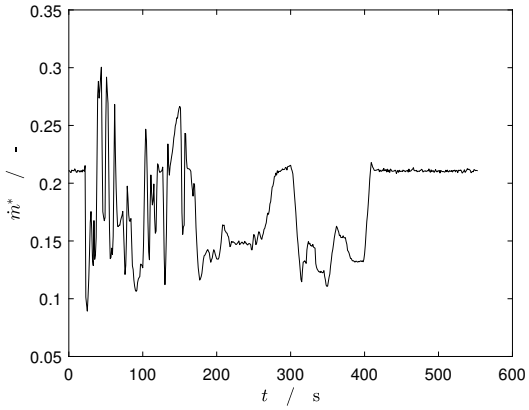

(a) Exhaust mass flow

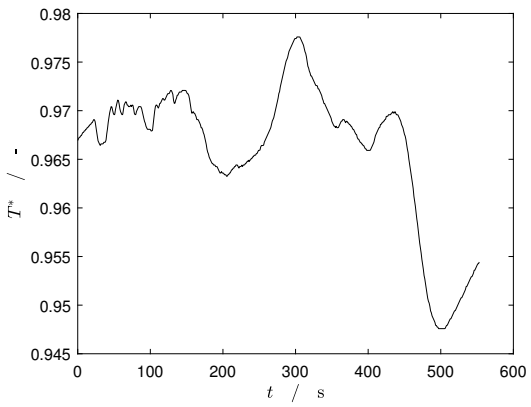

(b) Exhaust inlet temperature

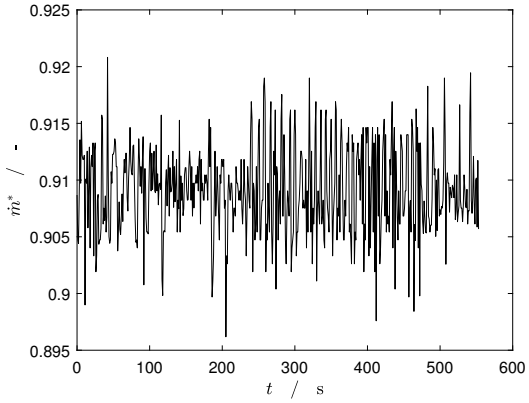

(c) CW mass flow

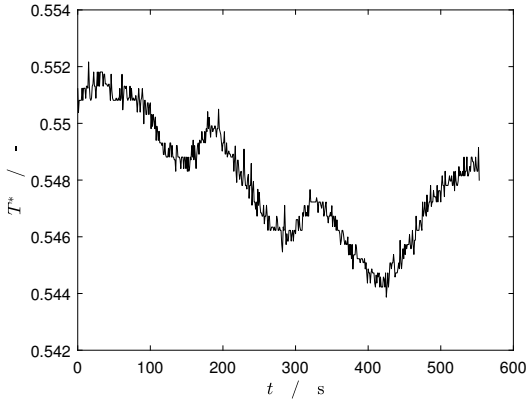

(d) CW inlet temperature

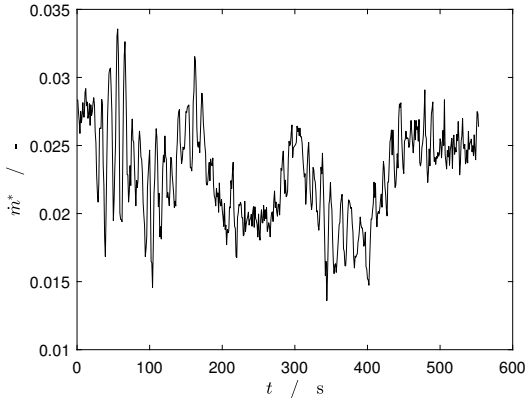

(e) Evaporator WF inlet mass flow

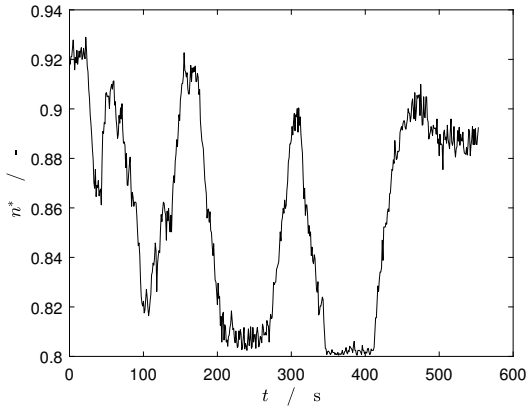

(f) Turbine speed

Figure 3.7: Trajectories of all controlling inputs within the measurement used for the model validation.

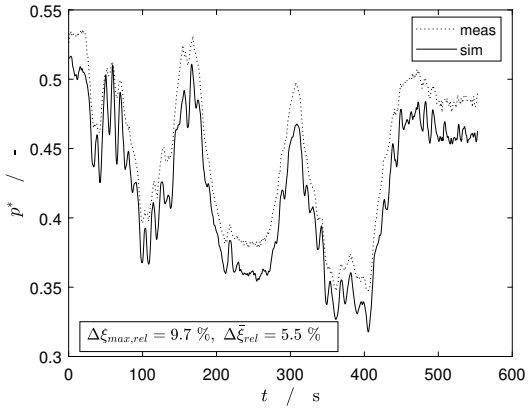

(a) Evaporator WF outlet pressure

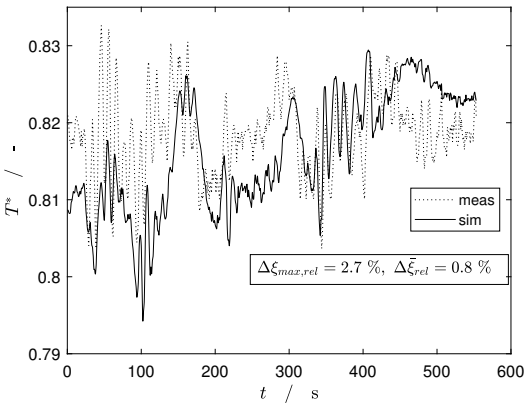

(b) Evaporator WF outlet temperature

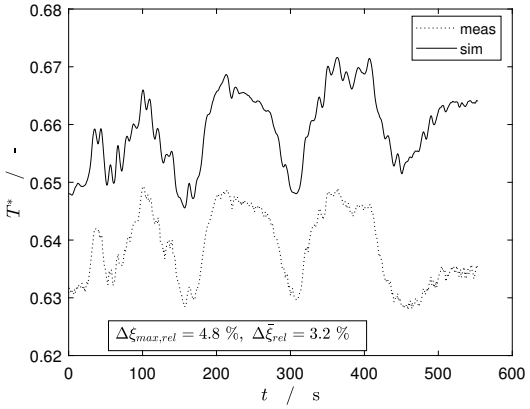

(c) Turbine WF outlet temperature

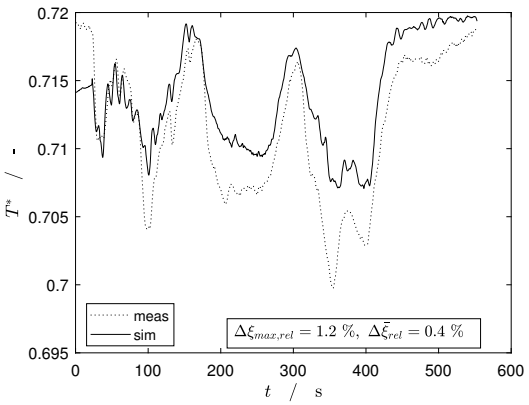

(d) Exhaust outlet temperature

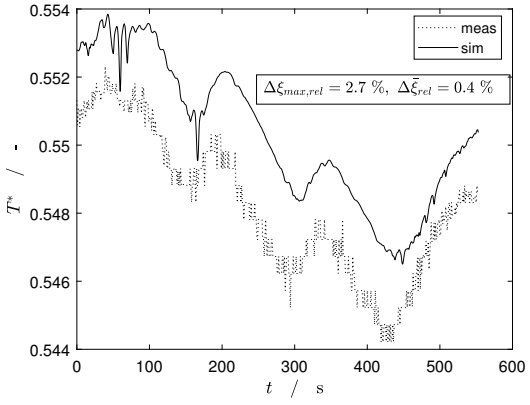

(e) Condenser WF outlet temperature

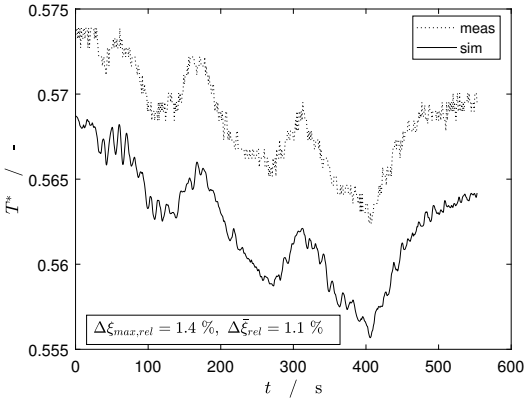

(f) CW outlet temperature

Figure 3.8: Simulated trajectories of relevant thermodynamic variables of the ORC in comparison to their corresponding measured trajectories within the model validation, including maximal and mean relative errors.

smaller than 4 % for all measured temperatures for a transient measurement data set. The mean relative error for both evaporator outlet temperatures is smaller than 1 %. For the high pressure level, a mean relative deviation of 5.5 % arises. This model accuracy could not have been obtained without the parameter estimation applied to transient data.

Chapter 4

Comparison and improvement of heat exchanger models with phase changes

4.1 Introduction

In this chapter, we extend our model from Chapter 3 to cover non-nominal operation. Furthermore, we implement a FV heat exchanger model for comparison. Dynamic models of HXs are used for simulation, control and optimization of a variety of systems, such as ORCs [118, 135, 149, 138], vapor compression systems [121, 150, 151, 120] and solar thermal systems [134, 152]. The type of models employed depends on the requirements on precision and computational demand. As discussed in Chapter 3, two model types are predominantly used for HX: the MB approach and the FV method. In research contributions considering nonlinear model predictive control applications, the MB approach is typically employed due to its lower computational demand [123, 153]. In the FV method, the HX is discretized spatially. Often, an equidistant grid is chosen as the position of the two-phase zone is usually not known a-priori. Mass and energy are conserved in the volumes and the values of the edge fluxes are obtained depending on the discretization scheme. The MB approach and the FV approach both allow for the consideration of a pressure drop along the HX by including a momentum balance [28, 154]. Numerical problems, typically termed chattering [155], can occur when discontinuities in relevant thermodynamic derivatives at the saturation lines are present. Several methods to circumvent chattering have been proposed [156, 157, 158, 155].
The standard MB approach [28], as presented in Chapter 3, does not consider the appearance and disappearance of phases that can occur during transient operation of a HX. Several contributions generalized the MB approach to allow for the appearance

and disappearance of phases [128, 129, 130, 131, 159, 134, 132, 133]. Typically, the appearance and disappearance of zones is realized by employing a hybrid discrete-continuous approach in the sense of [160]. In literature, authors use different criteria for the model switches, such as enthalpy [133], a combination of enthalpy and zone length [134, 132], density and zone length [159] or void fraction and zone length [131]. While in many publications only selected switching events are described, all possible zone combinations are presented in [132]. The models are implemented in different simulation environments, e.g., Modelica [130, 161] or Simulink [131, 138].
The model from Chapter 3 represents the desired operational mode of the ORC ("nominal operation") in which superheated vapor is obtained from the evaporator and the expander can be used for power generation.
In this Chapter, we assess both the MB and FV modeling approach. In particular, we discuss the model behavior in start-up situations. To account for conditions of insufficient heat availability, such as the start-up of the ORC, we extend our MB model from Chapter 3 to a hybrid discrete-continuous model [160] in this Chapter. Our analysis reveals that the MB approach exhibits some limitations that become evident during simulations of start-ups.
In most relevant literature [121, 120], the discussed modeling approaches are compared on the application to vapor compression systems. In [121], the authors limit themselves to cases where model switching occurs at the HX outlet. They find that the MB and FV approaches result in similar accuracy, while the FV approach has a higher computational demand. The trade-off between accuracy and computational demand is investigated in [120], where a switching MB and FV model are compared. Desideri et al. [119] examine HX models in ORCs but exclude switching in their analysis. The authors present an integrity test that assesses a model's capability to ensure energy and mass conservation. In their work, all implemented models pass the test. For assessment of model accuracy, a FV model with 100 control volumes is used as reference. Rodriguez and Rassmussen [122] assess the impact of the switching criteria and thresholds of the MB model on its performance. The authors compare the deviation of the MB model from a FV model and argue that the MB model should closely mimic the FV model and that the number of switches should be similar.
The remainder of this chapter is structured as follows: In Chapter 4.2, we present the models for the MB and FV approach. In Chapter 4.3, we identify the limitations of the MB approach related to the start-up of a condenser. We then propose solutions for the identified shortcomings in Chapter 4.4. In Chapter 4.5, we compare these solutions for the start-up of a condenser of an ORC using data from an existing test rig. We provide conclusions in Chapter 4.6.

4.2 Model description

In this section, we first discuss the extensions of the MB model from Chapter 3 to handle the appearance and disappearance of zones. In the second part of this section, we introduce the FV approach. we address the well-known chattering problem appearing in the FV approach using the smooth-density method [155], which is a recommended measure as it provides high accuracy together with limited additional computational cost. Both models are implemented in the equation-oriented modeling software gPROMS v5.0.1 (x64) [162]. The model equations are shown in Chapter 3.3.1 for the MB approach and Appendix B for the FV approach. For both models, the required thermodynamic properties of the WF are calculated from an implementation of a fundamental equation of state based on the free Helmholtz energy [141, 116].

4.2.1 Switching moving boundary model

The mass and energy balance of the exhaust/coolant side are modeled quasi-stationary and the energy balance for the wall element is identical to the one presented in Chapter 3. Depending on the application, various combinations of single-phase and two-phase flow zones and switches between combinations are possible [132]. Herein, we restrict ourselves to combinations of zones as they typically occur during operation of power cycles. The treatment of the discrete-continuous behavior is transferable to other case studies, such as the operation of vapor compression cycles [131]. The relevant model equations can be found in Chapter 3.3.1. For our case study, all possible combinations of zones are illustrated in Fig. 4.1 for the condenser. We assume that the WF leaving the condenser/entering the evaporator is always in subcooled state. The following model states are accounted for:

- Condenser (Evaporator)
  - SC (SC): only a subcooled zone exists
  - TPSC (SCTP): a two-phase zone and a subcooled zone exist
  - SHTPSC (SCTPSH): a superheated zone, a two-phase zone and a subcooled zone exist. This is equivalent to our model presented in Chapter 3.

The nomenclature reflects the fact that state events occur only at the evaporator outlet and the condenser inlet, as is typical for power cycles. Handling of the discrete state events that trigger switching is discussed in a variety of publications [132, 133, 154]. Herein, we choose a switching scheme based on enthalpy, as illustrated in Fig. 4.1. When simulating hybrid discrete-continuous models using declarative modeling lan-

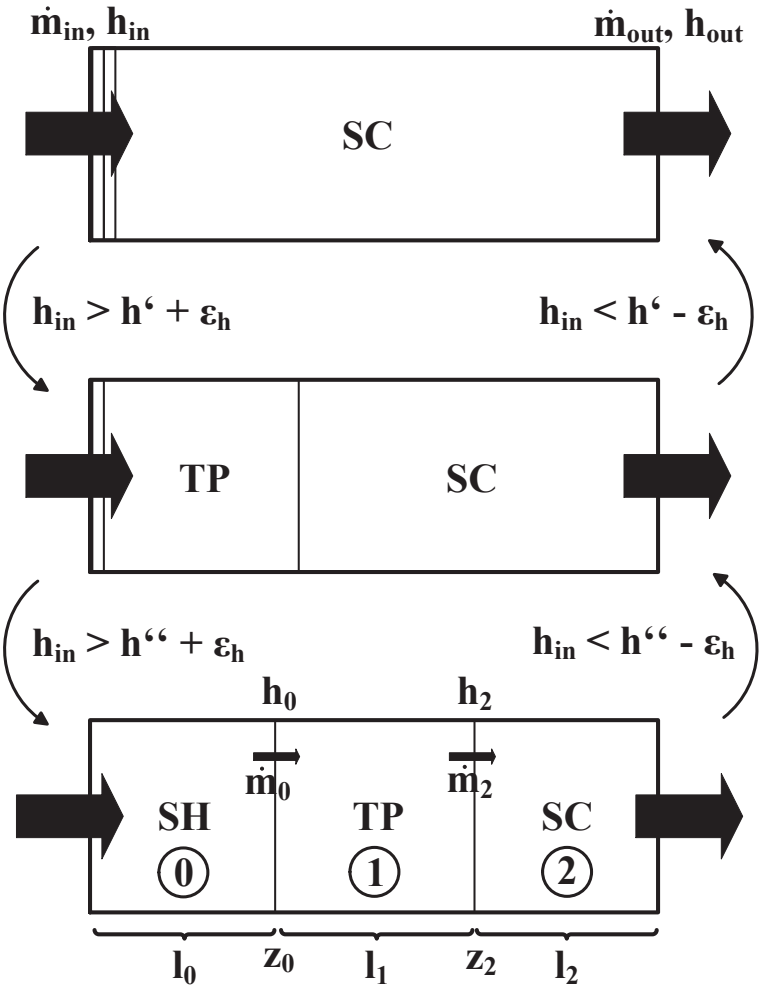

Figure 4.1: Illustration of switching events for the MB approach for the case of a condenser. Horizontal lines at the left end in the top and middle figure represent inactive zones. Inequalities display the switching criteria, in which the inlet/outlet enthalpy is compared to the saturation enthalpy plus/minus a small positive value (ϵ_h).

guages, such as gPROMS [162], all differential states have to exist in all continuous modes of the model. To satisfy this requirement, inactive zones are handled by pseudo balances, which allow for a proper initialization when the zone is reactivated. We illustrate this approach on the example of the inactive superheated zone for the condenser in TPSC mode (see Fig. 4.1, middle), where we have the following equations:

$$\frac{\mathrm{d}l_0}{\mathrm{d}t} = 0, \tag{4.1}$$

$$\frac{\mathrm{d}T_{w,0}}{\mathrm{d}t} = \frac{1}{\tau_w}\left(T_{w,1} - T_{w,0}\right), \tag{4.2}$$

$$\dot{m}_{in} = \dot{m}_0, \tag{4.3}$$

$$\frac{\mathrm{d}h_0}{\mathrm{d}t} = \frac{\mathrm{d}h_{in}}{\mathrm{d}t} + \frac{1}{\tau_h}\left(h_{in} - h_0\right), \tag{4.4}$$

in which l is the length of the zone, t the time, $\dot{m}$ the mass flow of the WF crossing a zone boundary, h the mass-specific enthalpy, T_w the temperature of the wall and the user-specified time constants τ_w and τ_h. As it serves to eliminate the offset resulting from ϵ_h, the parameter τ_h should be generally assigned to a small value. τ_w eliminates the temperature difference between a zone that vanished and its neighbor. A general rule for providing an adequate value for τ_w cannot be stated here as it depends on the system at hand. Subscript 0 indicates the superheated zone in the condenser.
If the two-phase zone and one of its neighboring zones are active, the enthalpy at the left (h_0) or right zone boundary (h_2) tracks the liquid respectively vapor saturation enthalpy (h' and h''), depending on pressure p. This is shown in (4.5) for the previously mentioned case, in which h_2 tracks h'.

$$\frac{\mathrm{d}h_2}{\mathrm{d}t} = \frac{\mathrm{d}h'}{\mathrm{d}p}\frac{\mathrm{d}p}{\mathrm{d}t} + \frac{1}{\tau_h}\left(h' - h_2\right) \tag{4.5}$$

4.2.2 Finite volume model

For the FV model, we use the same assumptions as for the MB approach in Chapter 3. The model equations are discretized on an equidistant grid and can be found in Appendix B. Fig. 4.2 provides a visualization of the discretization scheme.
The partial derivatives of the density ρ of the WF $\partial\rho/\partial h|_p$ and $\partial\rho/\partial p|_h$ are discontinuous at the phase boundary between subcooled and two-phase fluid. This gives rise to a spurious numerical internal mass flow in a volume when switches occur. This phenomenon causes a high number of discontinuous switches, hence is termed chattering in literature [158], and can drastically reduce simulation speed. It is well known that it also gives rise to large numerical errors which can eventually even lead

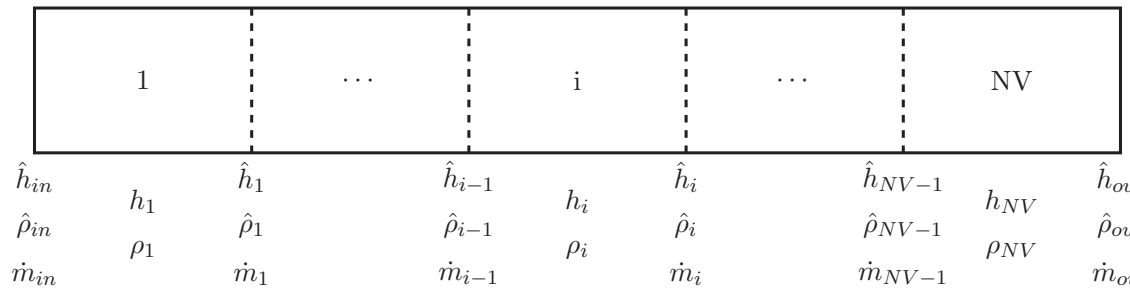

Figure 4.2: FV discretization scheme with the values for h, ρ and $\dot{m}$ for both cells and boundaries.

to flow reversal, i.e., negative value of $\dot{m}_{WF}$ [155]. Several methods to circumvent the problem have been proposed [156, 157, 158, 155]. Herein, we apply smoothing of the density function [155] within a transition section (vapor quality $x \in [0, \delta]$). Thereby, the equation of state is replaced by a third order polynomial for a $\mathcal{C}^1$-continuous density approximation in the transition section. Hence, each cell volume is in one of the following states:

- SC: subcooled fluid,
- TRANS: transition to two-phase fluid,
- TP: two-phase fluid,
- SH: superheated fluid.

To avoid a chattering effect due to discontinuities in the heat transfer coefficients in the cells, we use a linear interpolation with respect to x for the FV model:

$$\alpha_{liq-trans} = \alpha_{liq} + \big(\alpha_{trans} - \alpha_{liq}\big)\frac{x}{\delta} \quad \text{for} \quad x \in [0, \delta]\,, \tag{4.6}$$

$$\alpha_{trans-vap} = \alpha_{vap} + \big(\alpha_{trans} - \alpha_{vap}\big)\frac{1-x}{\delta} \quad \text{for} \quad x \in [1-\delta, 1]\,, \tag{4.7}$$

where α is the heat transfer coefficient, the subscripts liq, $trans$, vap indicate quantities in subcooled, two-phase and superheated region and δ is a user-specified parameter. Note that the transition region of the heat transfer coefficient and smoothed density function are expressed in terms of the same model parameter δ, hence the regions coincide. This choice is natural in order to minimize the number of state events during simulation to further mitigate chattering effects and speed up simulations, however, it is not mandatory.

4.3 Model analysis for start-up operation

In this section, we discuss the start-up process where the HX is in SC mode, i.e., only subcooled liquid is present. We identify a limitation of the MB approach by simulating a typical start-up situation in a condenser with parameters (heat transfer coefficient, residence time) taken from literature. Further, we simplify and analyze the model equations to identify the cause of the limitation. Our analysis indicates that the problem becomes particularly evident in the condenser. Finally, we present two approaches to circumvent the problem.

4.3.1 Problem identification

At the beginning of the start-up procedure, the condenser is completely filled with subcooled liquid. Hence, the employed MB model only consists of one active zone. Further, the inlet enthalpy of the WF entering the condenser increases strongly during start-up.
We assume a constant rate of change in inlet enthalpy of $\mathrm{d}h_{in}/\mathrm{d}t = 1500\ \mathrm{J/(kg \cdot s)}$ for the first 100 s of the simulation and $\mathrm{d}h_{in}/\mathrm{d}t = 0\ \mathrm{J/(kg \cdot s)}$ for the remaining 300 s. The average residence time of the WF in the condenser τ_{HX} is given by

$$\tau_{HX} = \frac{\bar{\rho} V}{\dot{m}_{WF}} \tag{4.8}$$

and adjusted to a value taken from literature (140 s, [163]) by choosing an adequate V and $\dot{m}_{WF}$ for this constructed example. $\bar{\rho}$ and V are the averaged density of the WF and the HX volume. The HX is operating in a WHR system with open tank valve, i.e., at ambient pressure. The use of a Laval nozzle model from Chapter 3 allows enforcing a near constant pressure level. For the heat transfer from the WF to the wall, we choose a heat transfer coefficient of $\alpha_{liq} = 400\ \mathrm{W/(m^2 \cdot K)}$ [143]. We assume constant WF and CW mass flow rates and a constant CW inlet temperature of 298 K. The model is initialized at steady-state for $\mathrm{d}h_{in}/\mathrm{d}t = 0\ \mathrm{J/(kg \cdot s)}$, so that it is subjected to a step in the inlet enthalpy rate of change as $t = 0$ s, as is typical in the start-up situation. The resulting WF outlet temperature is depicted in Fig. 4.3. It can be seen that the increase in inlet enthalpy leads to a substantial initial decrease in outlet temperature. In the illustrated case, the temperature drops from the initial steady-state to 282 K. When $\mathrm{d}h_{in}/\mathrm{d}t$ is set to zero at $t = 100$ s, the WF outlet temperature trajectory exhibits a kink and consequently approaches a new stationary value. From physical insight, an increase in outlet temperature due to the increase in h_{in} after some initial delay associated with τ_{HX} would be expected under the given conditions.

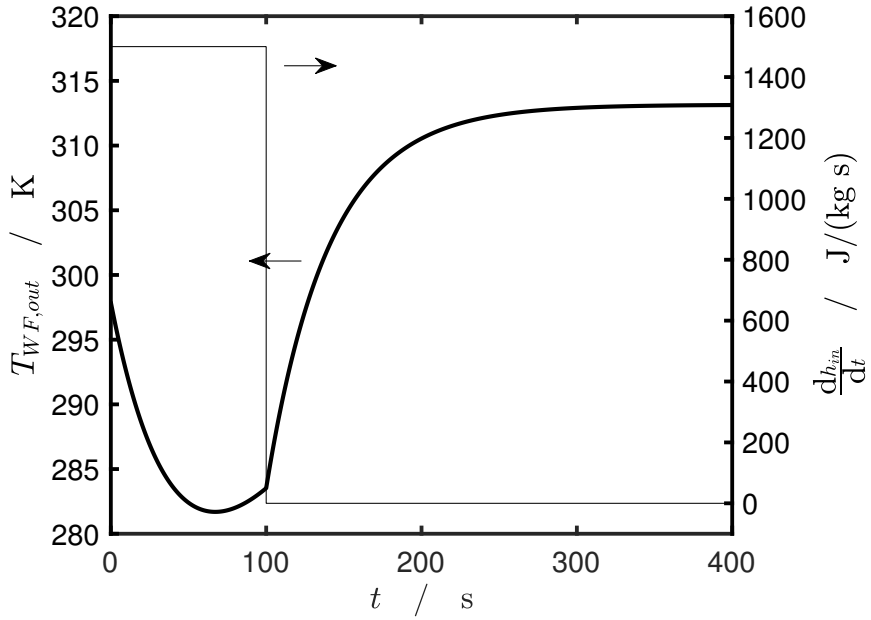

Figure 4.3: Simulated WF outlet temperature in the start-up case with heat transfer, together with the change of inlet enthalpy.

The model behavior seen in Fig. 4.3 is therefore non-physical and can cause severe numerical problems. In fact, we experienced several crashes during simulation of the model due to the WF outlet temperature reaching the lower bound for temperature variables when we carried out simulations with input data from the test rig described in Chapter 3.
By varying the mass flow rate, we further assess the effect of the residence time on the identified phenomenon. To avoid different final steady-states and to isolate the effect of the residence time, we remove the heat transfer term from the model equations to allow for a distinct analysis of this behavior. The inlet enthalpy is raised starting at $t = 0$ s with a constant rate of 100 J/(kg · s). At $t = 300$ s, the rate of change of the inlet enthalpy is set to 0 J/(kg · s).
The results are depicted in Fig 4.4 and demonstrate that a higher residence time amplifies the effect.

4.3.2 Problem analysis

As the model consists of a single active zone with length l_{tot}, we replace the indexes a and b with *in* and *out*. To allow for assessment of model equations, we assume the WF

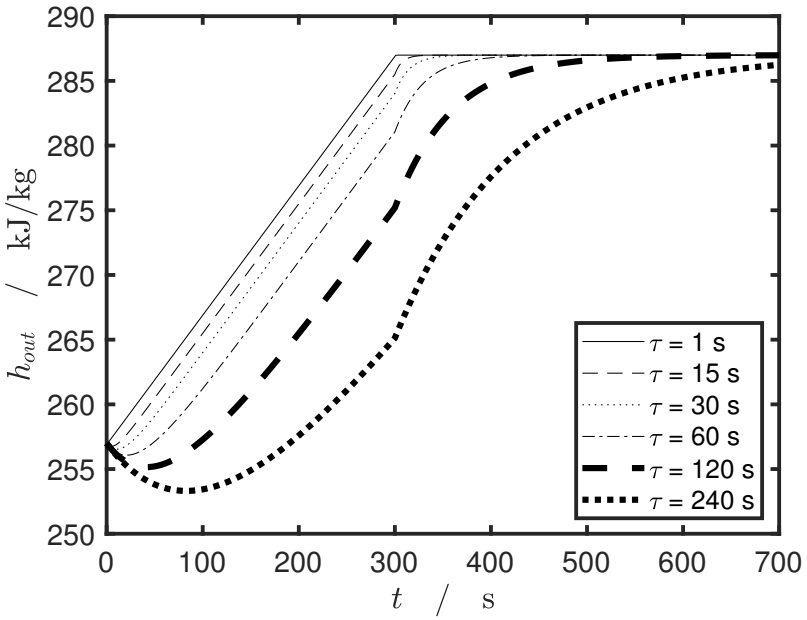

Figure 4.4: Simulated WF outlet enthalpy in the start-up case with no heat transfer for different residence times.

density to be constant, i.e., $\partial\rho/\partial p = 0$ s^2/m^2 and $\partial\rho/\partial h = 0$ (kg $\cdot$ s^2)/m^5, which is a reasonable assumption for subcooled fluids. Further, we assume isobaric operation during start-up, i.e., $\mathrm{d}p/\mathrm{d}t = 0$ bar/s. The boundaries of the zone do not move in space, i.e., $\mathrm{d}z_{in}/\mathrm{d}t = 0$ m/s and $\mathrm{d}z_{out}/\mathrm{d}t = 0$ m/s. Using these assumptions, the mass and energy balance (3.1) and (3.2) of the MB formulation simplify to

$$\frac{\mathrm{d}h_{out}}{\mathrm{d}t} = \underbrace{\frac{2}{\tau_{HX}}\left(h_{in} - h_{out}\right)}_{①} - \underbrace{\frac{2 \cdot \alpha_{WF}\ b_{WF}\ l_{tot}\left(T_w - \bar{T}\right)}{\rho V}}_{②} - \underbrace{\frac{\mathrm{d}h_{in}}{\mathrm{d}t}}_{③}, \tag{4.9}$$

where b_{WF} is the heat transfer width and $\bar{T}$ the averaged temperature of the WF.
In order to assess the behavior of h_{out}, the terms in (4.9) have to be evaluated. At the beginning of the start-up process ($t = t_0$), the temperature along the length of the HX is constant, i.e., $h_{in}(t_0) = h_{out}(t_0)$ and the fluid temperature is equal to the wall temperature, i.e., $\bar{T}(t_0) = T_w(t_0)$. Hence, term ① and term ② on the right-hand side (RHS) of (4.9) are initially equal to zero. Consequently, the MB model response shows an initial decrease in h_{out} to an initial increase in h_{in} under these assumptions. The decrease in h_{out} continues until the difference of term ① and ② becomes greater than term ③. In a physical system, the outlet enthalpy is expected to increase in

response to a ramp in inlet enthalpy after a certain time delay due to the average residence time of the fluid in the apparatus.
By neglecting the heat transfer term ② from the RHS of (4.9), we obtain a linear system that allows for a more detailed analysis in the Laplace domain. We introduce the Laplace transform of the linear system (4.10) by setting $y(t) = h_{out}$ and $u(t) = h_{in}$, i.e.,

$$\mathcal{L}(\dot{y}(t)) = \frac{2}{\tau_{HX}} (\mathcal{L}(u(t)) - \mathcal{L}(y(t))) - \mathcal{L}(\dot{u}(t)) . \tag{4.10}$$

We can rearrange (4.10) to obtain the transfer function $G(s)$.

$$G(s) = \frac{Y(s)}{U(s)} = \frac{-s + \frac{2}{\tau_{HX}}}{s + \frac{2}{\tau_{HX}}} \tag{4.11}$$

The system exhibits a positive root of the term in the nominator of (4.11). This is called a non-minimum phase zero and is a well known phenomenon in control engineering [164]. Non-minimum phase systems are associated with an inverse response behavior, as identified in the previous section, which is unphysical for the examined system. The linear system can be solved analytically. The resulting trajectories of the analytic solution for the outlet enthalpy h_{out} for a step in $\mathrm{d}h_{in}/\mathrm{d}t$ and a variety of residence times are depicted in Fig. 4.5. The effect occurs irrespective of the residence time, though its significance differs. This is in agreement with (4.9), as the residence time influences the first term on the RHS. Note that assuming no heat transfer is conservative for a condenser as the occurrence of heat transfer with $\bar{T} > T_w$ would enhance the phenomenon. This is obvious from (4.9), where the second term on the RHS would be negative, hence amplify the effect.

4.4 Proposed solution approaches for start-up operation

The behavior observed and analyzed in Chapter 4.3 can be traced back to the averaging assumption for the enthalpy

$$\bar{h} = \frac{1}{2} (h_a + h_b) , \tag{4.12}$$

which is commonly used in the MB approach [28]. In situations such as a start-up, where the enthalpy difference between the zone boundaries of a single zone is small, the model predicts an inverse reaction of outlet enthalpy to changes in inlet enthalpy,

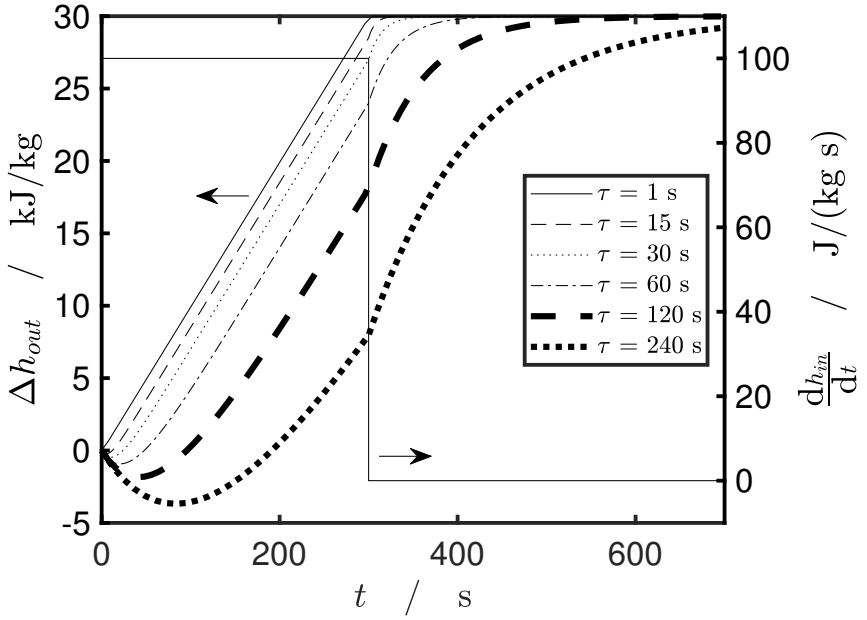

Figure 4.5: Analytic solution of (4.9) assuming no heat transfer and $\mathrm{d}h_{in}/\mathrm{d}t = 100\ \mathrm{J/(kg \cdot s)}$ between 0 and 300 s and $\mathrm{d}h_{in}/\mathrm{d}t = 0\ \mathrm{J/(kg \cdot s)}$ between 300 and 700 s for a variety of residence times.

in particular for small throughput to volume ratios, i.e., high τ_{HX}. A straightforward method to prevent this behavior is to change the averaging assumption (4.13) for $\bar{h}$ by adjusting the averaging parameter f

$$\bar{h} = f \cdot h_{in} + (1 - f)\, h_{out}\,, \tag{4.13}$$

which will be discussed in the following. If we apply the altered assumption to (4.9), neglect the heat transfer term ② and perform the Laplace transform, we obtain the transfer function $G^f(s)$

$$G^f(s) = \frac{-\frac{f}{1-f}s + \frac{1}{(1-f)\tau_{HX}}}{s + \frac{1}{(1-f)\tau_{HX}}}. \tag{4.14}$$

Reducing f monotonically decreases the spurious inverse response. For $f = 0$, which is equivalent to an ideal mixing assumption, the inverse response completely vanishes. It has to be noted that reducing f to zero yields a first-order system with response time τ_{HX}. The resulting transfer function $G^{f=0}(s)$ reads

$$G^{f=0}(s) = \frac{1}{\tau_{HX}s + 1}. \tag{4.15}$$

Clearly, a first-order response is not representative of the physical behavior as the delay in the outlet response due to the residence time of the HX is neglected. Note that the altered averaging assumption ($f = 0$) is equivalent to a FV model with $NV = 1$ for a first-order upwind scheme which generally has the transfer function $G^{FV}(s)$

$$G^{FV}(s) = \frac{1}{\left(\frac{\tau_{HX}}{NV}s + 1\right)^{NV}}. \tag{4.16}$$

An illustration of the behavior with the altered averaging assumption (4.13) is depicted in Fig. 4.6, for a system with a residence time of 60 seconds making use of the assumptions from Chapter 4.3.2. Again, $\mathrm{d}h_{in}/\mathrm{d}t = 100$ J/(kg · s) for the first 300 seconds and $\mathrm{d}h_{in}/\mathrm{d}t = 0$ J/(kg · s) for the last 400 seconds. This corresponds to a ramp in h_{in}. For comparison, the corresponding trajectories with the standard averaging assumption and $f = 0.3$ are also depicted, as well as the behavior for ideal plug flow, reflecting the expected behavior of the simulation. Further, the solution for the FV approach with $NV = 20$ is depicted. A detailed view of the first 100 seconds is provided in Fig. 4.7. The higher order behavior of the FV model captures the delay due to the residence time best and it can be seen that the classic averaging assumption exhibits a trajectory very similar to the one of the FV model after the initial inverse response. The altered averaging assumption does not exhibit the inverse response, but the trajectory differs slightly more. However, this drawback is insignificant compared to avoiding potential simulation failures. The observation that the FV approach with multiple cells most closely mimics the expected behavior suggests a combination of both modeling approaches.

Since the problem only occurs in particular situations, the FV model should only be used when it is necessary as it is associated with higher computational cost. Consequently, we only use the FV approach when only the liquid zone is present. Otherwise, we use the MB approach. As mentioned before, most equation oriented modeling frameworks require the vector of differential quantities to consist of the same variables for each continuous mode of switching models. Hence, the FV equations also have to be solved when the model is inactive. However, we can use pseudo-balances as they would be used for inactive zones in a switching MB model as suggested in, e.g., [132]. So, when the HX is in SC mode, the balances of the MB model are simplified and the variables are set to dummy values. The FV model is solved as usual and all balances for each cell are solved. When the inlet enthalpy fulfills the switching criterion ($h_{in} > h' + \epsilon_h$), the model switches to the MB mode and consequently uses its balances. The FV balances are then simplified, e.g., the heat transfer and time-derivative of the distributed state variable $h_{fv,i}$ are set to zero, thus reducing

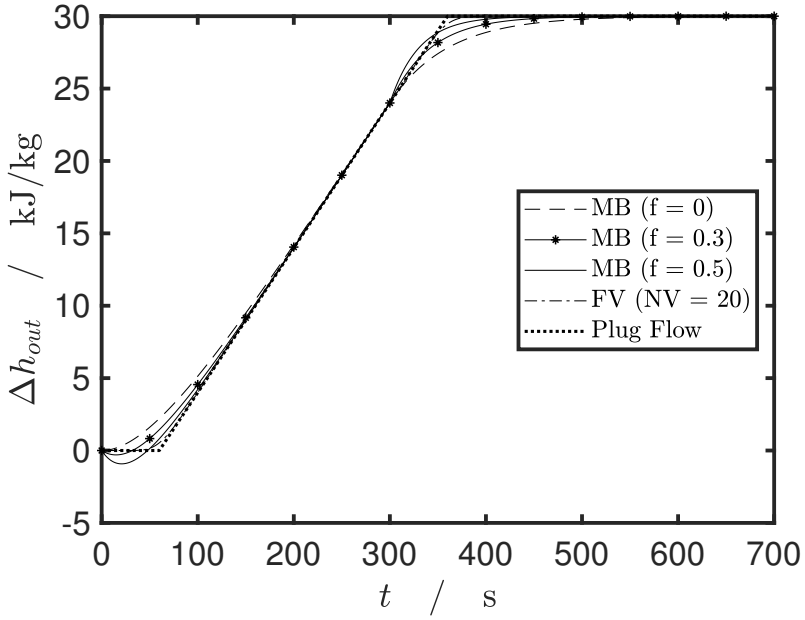

Figure 4.6: Solution assuming no heat transfer and $\mathrm{d}h_{in}/\mathrm{d}t = 100$ J/(kg · s) between 0 and 300 s and $\mathrm{d}h_{in}/\mathrm{d}t = 0$ J/(kg · s) between 300 and 700 s for a residence time of $\tau_{HX} = 60$ s. Depicted is the solution of Eq (4.14) for the MB approach with the respective values of f and Eq. (4.16) for the FV model.

computational demand compared to using a full FV model. Also, there is no change in the algebraic FV variables $\rho_{fv,i}$, $T_{fv,i}$, $p_{fv,i}$ and $\dot{m}_{fv,i}$. For a possible subsequent switch to the nominal case, the equations then remain unaltered.

4.5 Evaluation of solution approaches for the start-up simulation of a condenser

In this section, we present simulation results for the start-up of a condenser used in an ORC for WHR. In particular, we compare the results using a conventional FV model with 20 cells to the two proposed solution approaches, i.e., changing the averaging assumption and the hybrid approach proposed in Chapter 4.4 which also uses 20 cells in SC mode. A simulation with the standard averaging assumption is not shown here as the simulation terminates prematurely when $T_{WF,out}$ drops below physically sensible values. The performance of the approaches is evaluated against measurement data obtained from the test rig described in Chapter 3, using the same model parameters

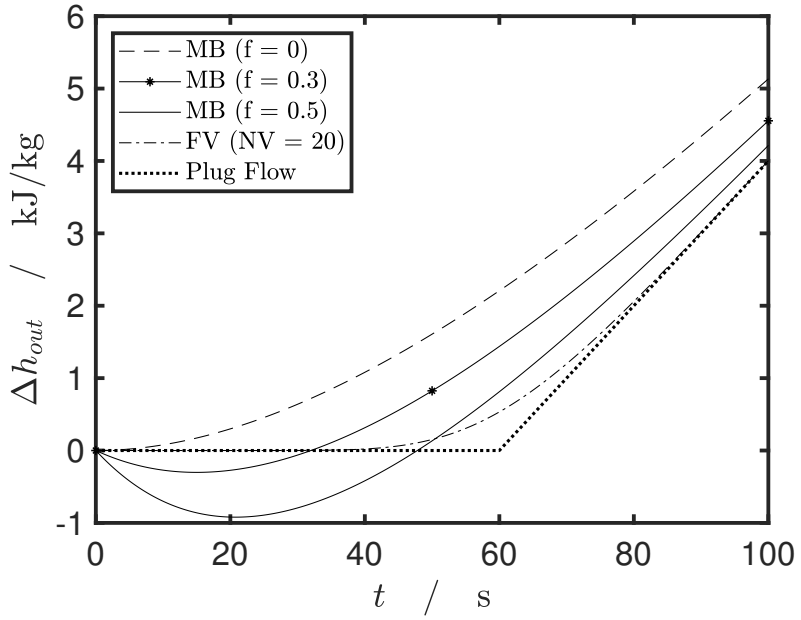

Figure 4.7: Detailed view of the solution assuming no heat transfer and $\mathrm{d}h_{in}/\mathrm{d}t = 100\ \mathrm{J/(kg \cdot s)}$ between 0 s and 100 s for a residence time of $\tau_{HX} = 60$ s.

and correlations. The inputs to the system, which are also obtained from the test rig, are the WF mass flow $\dot{m}_{WF}$, the WF inlet enthalpy h_{in} and its time derivative $\mathrm{d}h_{in}/\mathrm{d}t$, the CW mass flow $\dot{m}_{CW}$ and the CW inlet temperature $T_{CW,in}$. The trajectories of the inputs to the system are depicted in Fig. 4.8. It has to be noted that when the WF fed into the condenser is in two-phase state, the enthalpy cannot be reconstructed from the available measurement data (p, T) provided by the test rig. Hence, a linear increase in enthalpy is assumed for the case of a two-phase inlet state. The system is operated with an open tank valve, thus at constant ambient pressure in the condenser. The resulting WF and CW outlet temperatures for all three models are depicted in Fig. 4.9a and Fig. 4.9b.

The simulations illustrate that, by construction, none of the proposed approaches exhibits an inverse response. For the WF outlet temperature, the FV model captures the measurement data better than the two solution approaches, especially when the start-up is finished and all three zones are present. While a final offset remains for all models, the offset associated with the FV is clearly smaller. The hybrid approach is in accordance with all other models used. For the CW outlet temperature, the behavior during the two-phase inlet transition phase cannot be accurately captured by any modeling approach. When the start-up is finished and the system is working

in nominal operation, all approaches result in similar values. Thus, the two proposed solution approaches allow for robust start-up simulation while maintaining favorable computational demand.

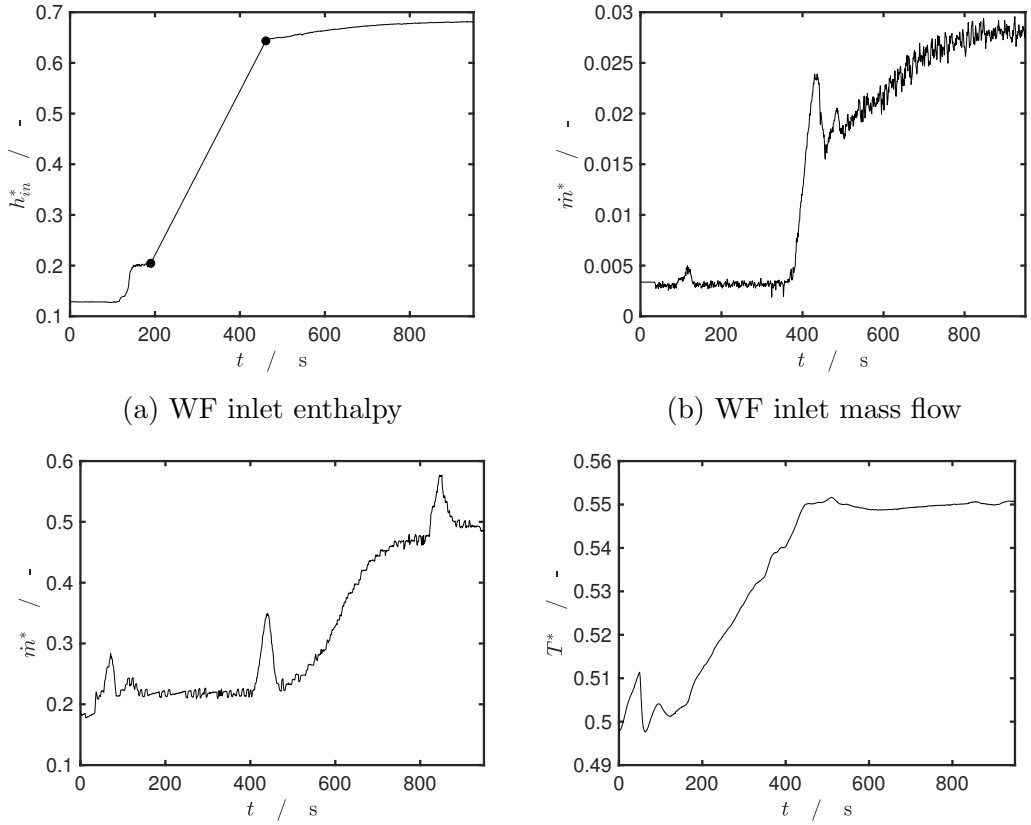

(a) WF inlet enthalpy

(b) WF inlet mass flow

(c) CW mass flow

(d) CW inlet temperature

Figure 4.8: Input variables for cold start case study. The two dots in Fig. 4.8b are the points where the entering WF is at the saturation points.

4.6 Conclusion

In this Chapter, we presented an assessment of dynamic HX models using the MB approach and the FV method. The analysis extends available literature by considering the start-up situation of an ORC for WHR. To enable this analysis, we extended the model presented in Chapter 3 to allow for switches in the model structure and implemented a FV model in gPROMS.

We carried out our analysis for the HXs of a power cycle. We discussed the start-up

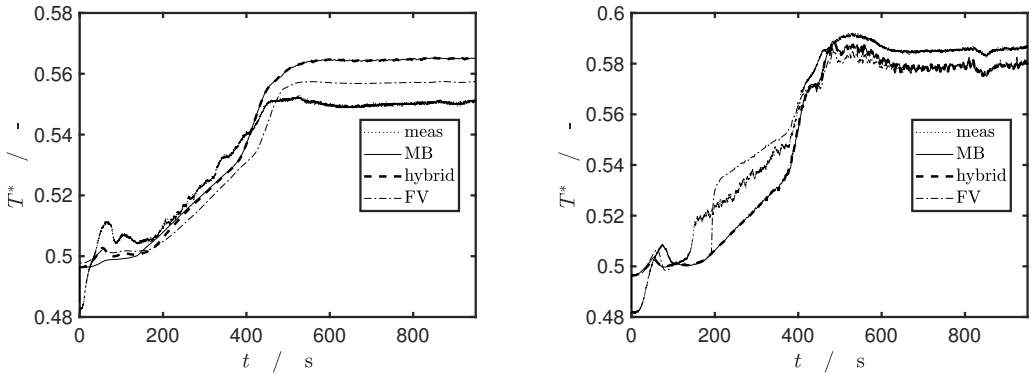

(a) WF temperature

(b) CW temperature

Figure 4.9: Resulting nondimensionalized temperatures of the fluids at the condenser outlet for the case study presented in Chapter 4.5.

of HX models in power cycles where initially only subcooled fluid is present. In a simulation, an inverse response of the MB model outlet temperature to a rise in the inlet enthalpy, which can even result in premature termination of simulations, can be observed. Analysis in the Laplace domain revealed that the inverse response corresponds to a non-minimum phase zero of the model.

We proposed two approaches to circumvent the identified issue. First, by changing the averaging assumption for the enthalpy, the pathological behavior can be avoided. Second, we proposed a hybrid model that uses the FV approach during start-up and the MB approach during nominal operation.

We compared the proposed solutions to the FV model in a case study, in which the start-up of the condenser of an ORC was considered. Measured data was obtained from the test rig presented in Chapter 3. The study shows that both proposed solutions successfully circumvent the identified problem. Hence, under the presented start-up conditions, changing the averaging assumption appears to be the most promising approach, as it preserves the favorable CPU times associated with the MB approach. Our findings indicate that special attention should be paid to the operating conditions that have to be covered when selecting a model type. However, our analysis concerning non-nominal operation is limited to the start-up of a power cycle. In vapor compression systems, for example, state events and high rates of change in enthalpy might occur at the evaporator inlet during start-up and shutdown operation [120].

Chapter 5

Optimal operating policies for the ORC system

5.1 Introduction

In this chapter, we discuss optimal operating policies for the considered ORC system for automotive WHR. In most of the classic ORC applications, the ORC system is operated either with a nearly constant heat source (geothermal), a slowly varying heat source that is predictable (solar-thermal) or with long periods of steady-state operation (ships and trains). Heavy-duty diesel trucks, however, are operated under highly transient heat source conditions due to their use in street traffic.
Available publications on ORC applications with non-transient conditions typically consider optimization of steady-state operating points [165, 166, 115], some including design considerations [167] and working fluid (WF) selection [168, 169, 78]. Sometimes even fluid mixtures are designed [70, 71, 74]. A possibility to account for mild variable operating conditions in design optimization is by clustering operating points [170, 171, 80] and considering off-design behavior with stationary [43] or simplified dynamic models [172, 79]. The publications in [171, 80, 79] consider WHR for a heavy-duty truck, whereas [170] considers a marine application and [172] considers a geothermal application. While steady-state models are used in most of the aforementioned publications, dynamic models might be required depending on the time scales on which changes in the inputs and disturbances occur related to the system inertia. Thus, most publications reporting dynamic ORC models consider waste heat recovery in diesel-trucks [139, 118, 135, 137, 147, 138, 75] but exceptions, e.g., [173], where a geothermal ORC system is considered, exist.

Many interactions between exhaust gas, ORC, cooling water cycle and engine exist [59] and the significance of dynamic effects on optimal system operation is widely accepted [174, 175, 56, 176]. To achieve efficient system operation, maximizing time in power production mode, i.e., maintain sufficient superheating to allow for turbine operation, is of paramount importance [117]. The effect of transient exhaust gas conditions is considered in [177] for an ORC system in a truck with two parallel heat exchangers utilizing the tailpipe exhaust gas and exhaust gas recirculation. The authors examine three strategies for set-point generation and find that a fuzzy logic strategy with flexible superheat exhibits the best performance. The work is extended with respect to real-time application in [178].
In order to adequately control the WHR system, understanding optimal system operation is crucial. Many of the numerous contributions on control design for ORCs consider following predefined set-point trajectories which are often obtained from steady-state optimization, neglecting dynamic effects [153]. The majority of publications on steady-state operation of ORCs finds that operation at minimal superheating is desirable [179]. Consequently, this notion is adopted in many control related publications where the control strategy aims at maintaining a fixed superheat [118, 180, 181, 182] or vapor quality [126]. However, in [43], Ghasemi and coauthors demonstrated that optimal off-design operation of air-cooled geothermal power plants mandates varying the superheat as a function of the ambient temperature. The literature review above indicates that, although many publications on control strategies for ORCs operated in a transient setting are available, a relevant research gap exists with respect to the understanding of economically optimal dynamic ORC operation.
In this Chapter, we address this gap by assessing whether the notion of operation at minimal superheat is optimal for an ORC for WHR in street traffic. Therefore, we apply dynamic optimization to the WHR system subject to transient heat source conditions. From the optimization results, we infer optimal operating policies. The dynamic optimization problem that we solve is closely related to the nonlinear model predictive control (NMPC) formulation, which has been applied to WHR in various publications [183, 47, 184, 153]. Indeed, we solve a similar optimal control problem (OCP) which considers the full length of the respective scenario and assumes full knowledge of the heat source. Thus, it represents an upper bound on the performance of NMPC and allows to draw conclusions for control strategy design. We consider two exemplary cases whose characteristics occur in street traffic. First, we consider exhaust data used for model validation in Chapter 3. For simplicity, we assume that no operational restrictions, beyond safety constraints, are imposed on the system.
Second, we examine a scenario where the permissible turbine power is temporarily limited. This scenario typically occurs in street traffic when the engine torque is neg-

ative or below a certain threshold. Though ORC systems for WHR can include a battery, the permissible turbine power can be limited by the operational constraints of the battery. The dynamic optimization problems are solved using the open-source dynamic optimization tool DyOS [185].
The remainder of this chapter is structured as follows. We provide a brief presentation of the changes to the model from Chapter 3 in Chapter 5.2, followed by a presentation of the optimization procedure in Chapter 5.3. In Chapter 5.4, we examine optimal operation for a typical driving cycle followed by a detailed examination of a scenario where the expander power is temporarily limited (Chapter 5.5). We discuss the results of the case studies and the implications on control strategy design in Chapter 5.6 and present our conclusions in Chapter 5.7.

5.2 Process model

The model representing the WHR system is based on the validated test rig model from Chapter 3 and implemented in Modelica. In addition to the assumptions stated in Chapter 3, we follow the common practice of focusing on the high pressure side of the system, i.e., we omit an elaborate condenser model as it does not significantly influence the high pressure part [176]. Instead, we assume that the condenser operates at ambient pressure and the WF leaves the condenser as a subcooled liquid with fixed subcooling (Fig. 5.1). Under these assumptions, the turbine rotational speed does not influence the high pressure side in our model and solely serves for optimizing turbine efficiency [63]. Further, we neglect heat losses in the pipes which connect the process units. In this Chapter, the WHR system is always operating in "nominal operating mode" as defined in Chapter 3.

5.3 Optimization problem

We solve dynamic optimization problems of the type introduced in Chapter 2.2 ((2.2a)-(2.2f)). Safety-related path constraints are specified as box constraints for the WF superheat ΔT_{sup}, the WF evaporator outlet temperature $T^*_{WF,evap,out}$ and the high pressure p^*. Asterisks indicate quantities that are scaled in the same manner as in Chapter 3. The degrees of freedom (DOF) for optimization are the WF fluid mass flow $\dot{m}^*_{WF,in}$, the turbine rotational speed n^*_{turb} and the exhaust gas valve position x_{BPV}, which are box-constrained as in (2.2f).
A list of the lower and upper bounds for the path constraints and the DOF is provided

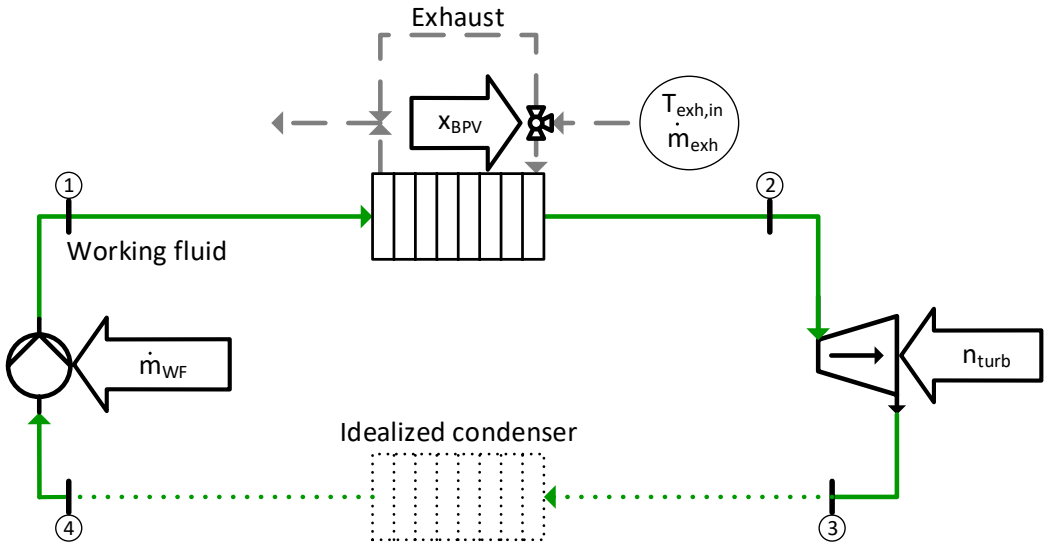

Figure 5.1: Adapted topology of the examined system. The WF is indicated by the solid green line and the exhaust gas by the dashed gray line. The DOFs are indicated by arrows and the disturbances by the circle. The condenser is represented with an idealized model that assumes operation at ambient pressure and fixed subcooling.

in Table 5.1. The constraint on minimal superheat protects the turbine from damage due to droplet formation. The lower bound on pressure reflects a minimal pressure ratio. As the condenser is assumed to operate at ambient pressure, this constraint can be directly expressed for the high pressure side. The upper bound on p^* ensures safe operation as does the maximum WF outlet temperature which prevents WF degradation. We do not specify a lower bound on WF outlet temperature. However, an effective lower bound is provided at any time through the minimal superheat constraint added with the saturation temperature of the pressure at that time. The lower and upper bounds on $\dot{m}^*_{WF,in}$ and n^*_{turb} reflect the limits in which the model is valid and the lower bound on x_{BPV} is included to avoid simulation failure due to very small exhaust gas mass flows.
In the following sections, we compare two operating policies. We assess the examined policies using the resulting net average power $P^*_{net,av}$, which is defined as follows

$$P^*_{net,av} = \frac{\int_{t_0}^{t_f} \left(P^*_{turb}(t) - P^*_{pump}(t)\right) \mathrm{d}t}{t_f - t_0} \tag{5.1}$$

where P^*_{turb} is the scaled turbine power and P^*_{pump} is the scaled pump power.
First, we assess a policy that aims at maintaining minimal superheat while using n^*_{turb}

Table 5.1: Bounds of path constraints and DOF.

Path				DOF			
Variable	Unit	LB	UB	Variable	Unit	LB	UB
ΔT_{sup}	K	10	-	$\dot{m}^*_{WF,in}$	-	0.0073	0.0363
$T^*_{WF,evap,out}$	-	-	0.8719	n^*_{turb}	-	0.73	1.09
p^*	-	0.3	1.5	x_{BPV}	-	0.05	1.00

to optimize turbine efficiency. We refer to this strategy, which is a standard approach in literature, as MSH (minimal superheat). Fixing the superheat to a minimal value is infeasible as it often resulted in integration failure. Furthermore no unique solution that provides minimal superheat exists, due to the availability of the exhaust gas bypass valve. Thus, we use an optimization-based approach. The objective can be expressed as

$$\Phi_1(t_f) = \int_{t_0}^{t_f} \left(\Delta T_{sup}(t) - \Delta T_{sup}^{min}\right)^2 \mathrm{d}t\,. \tag{5.2}$$

As we assess the examined operating policies based on $P^*_{net,av}$, we introduce specific measures that ensure that we find the minimal superheat strategy with highest $P^*_{net,av}$ in Chapter 5.4 and Chapter 5.5.
Second, we examine the thermodynamically optimal policy, i.e., maximizing the net work without consideration of a desired superheat, which we refer to as FSH (flexible superheat). This also corresponds to the economically optimal policy, given that all produced power can be utilized, and can be expressed as

$$\Phi_2(t_f) = -\int_{t_0}^{t_f} P_{net}(t)\,\mathrm{d}t\,. \tag{5.3}$$

We assume the validated model to represent the real system behavior herein. Since we are interested in understanding how to best operate the system, i.e., with FSH or MSH, mismatch between the system and our model is a minor concern. However, when the model is used for the control of a physical system, considerations regarding plant-model mismatch are required. A potential remedy could be the addition of a disturbance model to achieve offset-free model predictive control as practiced in [186]. For all scenarios, the initial state of the system $\boldsymbol{x}_0$ is specified to the economically optimal steady-state, indicated as $\boldsymbol{x}_{ss}^{opt}$, for the heat source conditions at $t = 0$ s

$$\boldsymbol{x}_0 = \boldsymbol{x}_{ss}^{opt}\left(\boldsymbol{d}(t=0), \boldsymbol{u}_{ss}^{opt}\right)\,. \tag{5.4}$$

We determine $\boldsymbol{x}_{ss}^{opt}$ in an a-priori optimization and, as expected, it corresponds to operation with minimal superheat.
The dynamic optimization problems are solved using direct single shooting [23] with the open-source software DyOS [185]. The model is linked to DyOS through the functional mock-up interface (FMI). The sensitivities are calculated through sensitivity integration with the integrator sLimex [187] and the NLPs are solved with SNOPT [89]. All degrees of freedom are discretized on a piecewise linear continuous grid which is determined by the grid adaption algorithm described in [188].

5.4 Optimal operation considering only safety constraints

In this section, we present the optimization of a typical transient driving cycle as it would occur in street traffic. We assume that there is no limit on expander power at any time and only the safety-related path constraints apply. The heat source data is taken from an experiment that includes parts of the World Harmonized Transient Cycle (Fig. 5.2). For FSH we minimize Φ_2.

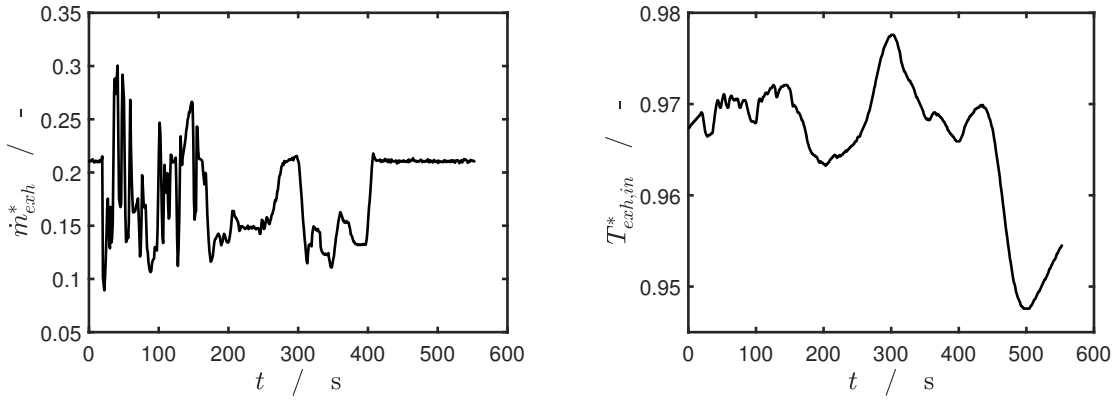

(a) Exhaust gas mass flow

(b) Exhaust gas inlet temperature

Figure 5.2: Heat source data for the WHTC taken from the test rig described in Chapter 3

For MSH, we exploit that n^*_{turb} only optimizes turbine power and use a two-step procedure. We first minimize Φ_1 to obtain minimal superheat and subsequently, we minimize Φ_2, where we fix the trajectory of $\dot{m}^*_{WF,in}$ to the optimal solution of the first step and leave n^*_{turb} as DOF to optimize turbine power. As we can separate the two optimization tasks of achieving minimal superheat and obtaining optimal turbine operation for the resulting operating conditions, we can avoid a weighting between

those objectives. All optimization problems are subject to (2.2b)-(2.2f).
The optimized trajectories for the DOF and key variables are depicted in Fig. 5.3. No trajectories for the exhaust bypass valves are presented as it remains fully opened at all times for both policies. For the examined case, a value of $P^*_{net,av} = 0.5307$ is obtained with FSH and $P^*_{net,av} = 0.5280$ with MSH. In other words, the additional flexibility merely yields a 0.5% increase in net average power. However, the trajectories differ strongly from each other in this case and several deviations from minimal superheat occur for FSH while for MSH only small deviations occur in order to maintain feasibility. Between $t = 0$ s and $t = 100$ s, the peaks for FSH occur at a high frequency and do not exceed 25 K. This might be due to the adaption algorithm as it is well known that a very fine discretization can lead to oscillatory control profiles [188]. More interesting are the two largest deviations in Fig. 5.3c, which do occur between $t = 300$ s and $t = 400$ s with two peaks exceeding 40 K, where the exhaust gas exhibits comparatively mild fluctuations. Apparently, the optimizer exploits the fact that temporarily operating at higher superheat, hence lower pressure level, can be advantageous. Further analysis showed that the amount of the heat recovered from the exhaust gas and transferred to the WF is higher for MSH. Moreover, we ruled out that the behavior is due to the fluid-dependent turbine efficiency map by executing the optimization with a turbine with fixed efficiencies where the behavior persisted. As a test using a different WF (cyclopentane) did not exhibit any peaks in superheat, the behavior appears to be fluid-specific.
As can be seen from Fig. 5.3a and 5.3b, the WF mass flow and turbine speed exhibit fast changes for FSH. It is questionable if a physical unit would be able to follow these trajectories and to what extent the additional strain would results in reduced lifetime of the components. For MSH, actor action is less drastic and less mechanical strain is expected. Further, realizing the peaks in superheat in a control setting would require foresight of the exhaust gas conditions. Considering these observations and the fact that MSH only produces 0.5% less power than FSH, using minimal superheat seems to be an appropriate control objective, when no other constraints apply.

5.5 Optimal operation including limitations on turbine power

The case presented in Chapter 5.4 can be considered as a best case scenario as no constraints beyond the safety constraints are considered. The strongest assumption we made in Chapter 5.4 is that the power produced by the turbine can always be utilized completely. Furthermore, operational constraints, i.e., constraints on maximal WF

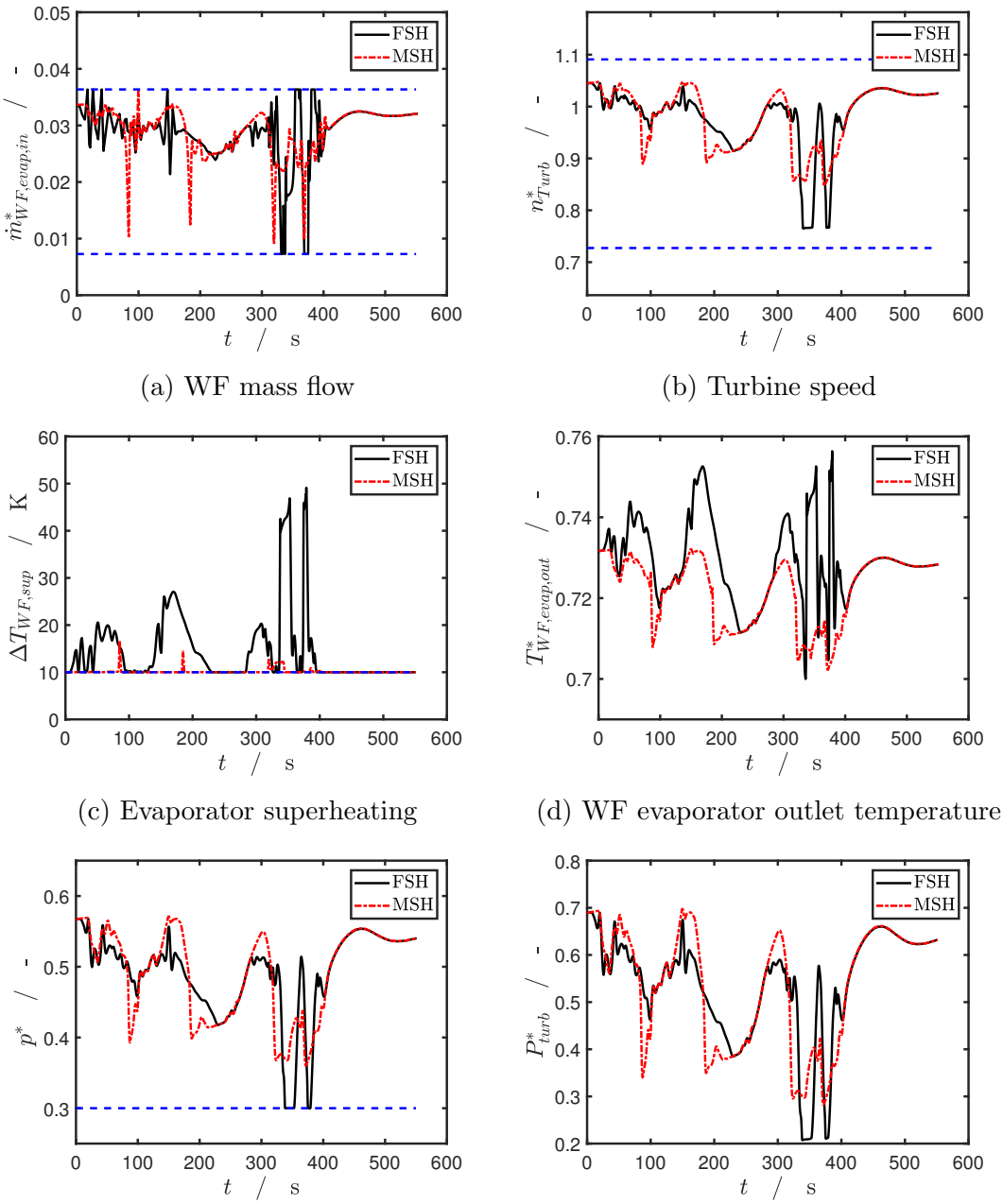

(a) WF mass flow

(b) Turbine speed

(c) Evaporator superheating

(d) WF evaporator outlet temperature

(e) Evaporator pressure

(f) Turbine power

Figure 5.3: Optimization results; dashed blue lines indicate lower and upper bounds.

temperature or pressure, could become active. We consider these scenarios in this section.

5.5.1 Active power constraint

To account for a situation where only a limited turbine power can be utilized, e.g., due to maximal charging current of a battery system, we consider a scenario with $t_f = 800$ s and constant exhaust gas conditions with $\dot{m}^*_{exh} = 0.201$, $T^*_{exh,in} = 0.967$. We assume that the expander power is temporarily limited. Here, we arbitrarily choose $t_1 = 200$ s and $t_2 = 400$ s as the start and end of the interval in which the power limitation applies. We assume knowledge of the times where the power limitation applies as we do with the heat source signals in order to obtain an upper bound on system performance. We realize this scenario by formulating a multistage dynamic optimization problem consisting of three stages. For FSH, we use Φ_2 as objective function. The optimization problem is subject to (2.2b)-(2.2f) and the turbine power constraint, active in the second stage, is added in (5.5)

$$P^*_{turb}(t) \leq P^{*,max}_{turb} \qquad \forall t \in [t_1,\, t_2]\ . \tag{5.5}$$

Due to (5.5), minimizing superheat and maximizing turbine power are not independent for this scenario and we do not use the two-step strategy from Chapter 5.4 for MSH. Instead, we realize MSH by minimizing Φ_2 subject to (2.2b)-(2.2f), (5.5) and adding an upper bound on superheat (5.6):

$$T^{max}_{sup} = 10.7 \text{ K}\,. \tag{5.6}$$

For reference, we consider the case without (5.5), i.e., operation at steady-state to allow for an estimate of the energy that is lost due to the power limitation.
The optimal results of the DOF and path constrained variables are presented in Fig. 5.4. The turbine power for FSH and MSH is presented in Fig. 5.5. Here, the advantages of FSH are evident. The optimizer exploits the thermal capacity of the evaporator to store thermal energy during the power limitation which is released after the power limitation ends. Shortly before the power limitation phase begins, the WF mass flow is reduced (Fig. 5.4a), while the exhaust bypass valve remains fully opened (Fig. 5.4c). Consequently, superheat rises and increases up to more than 100 K at the end of the power limitation phase. Approximately at $t = 390$ s, $T^*_{WF,evap,out}$ reaches its upper bound and the WF mass flow is increased, which decreases superheat. The turbine speed is adjusted to a suboptimal point to satisfy the limitation on power output. When the power limitation ends at $t = 400$ s, the WF mass flow is set to its maximum value which results in a strong increase in pressure and also in power production. The periods in time where the turbine power is lower than at optimal steady-state without power limitation are indicated by the blue cross-hatched area and the periods in time

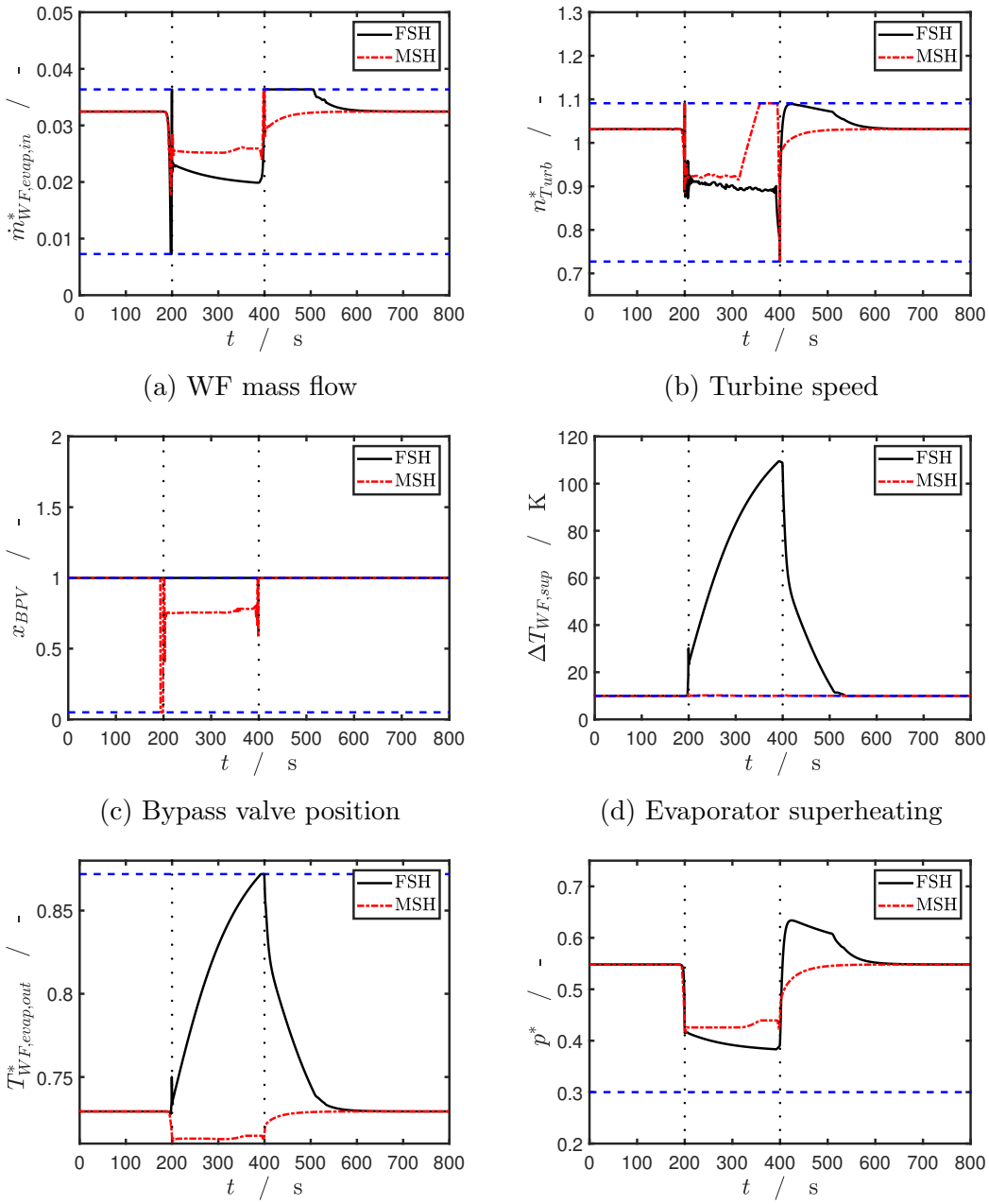

(a) WF mass flow

(b) Turbine speed

(c) Bypass valve position

(d) Evaporator superheating

(e) WF evaporator outlet temperature

(f) Evaporator pressure

Figure 5.4: Results of the optimization for the power limitation case for DOF and path constrained variables, dashed blue lines indicate lower and upper bounds.

where turbine power is higher are indicated by the green hatched area in Fig. 5.5a. The optimizer exploits that the heat exchanger wall temperature has increased during

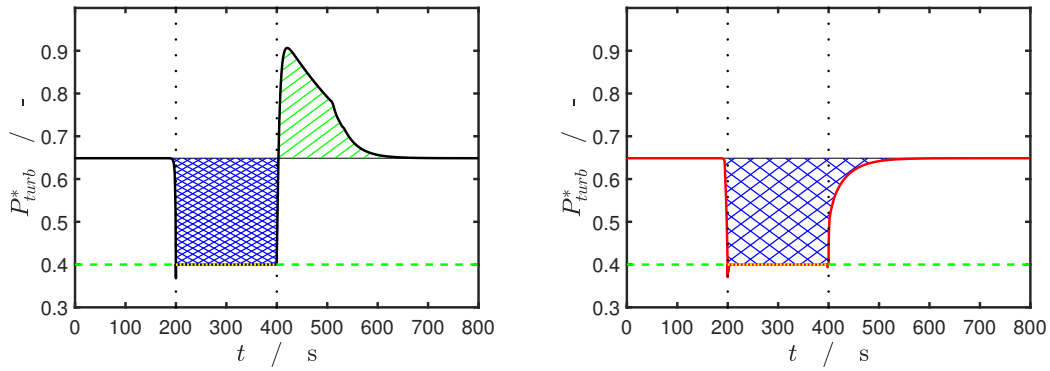

(a) Turbine power for FSH

(b) Turbine power for MSH

Figure 5.5: Turbine power for FSH and MSH for the power limitation case. Bounds that do not apply at all times are depicted as dashed green lines when they do not apply and yellow dotted lines when they apply.

the power limitation. Consequently, a higher WF mass flow can be evaporated as can be seen from Fig. 5.4a. Hence, parts of the energy not used earlier can be recovered. MSH, however, does not exploit this option to save energy, as can be seen in Fig. 5.4d. To allow for the required reduction of turbine power, the exhaust bypass valve opens shortly before the power limitations begins which can be seen in Fig. 5.4c. During the power limitation, it remains partially opened and a part of exhaust gas is bypassed to allow for satisfaction of the superheat path constraint. The system approaches a steady-state at minimal superheat with a partially opened exhaust bypass valve, hence not making full use of the exhaust gas potential. At the end of the power limitation, the valve is closed again and all the exhaust gas passes through the evaporator. In contrast to FSH, however, there is no heat available that can be recovered from the evaporator walls. Consequently, the system takes some time to reach the initial steady-state which results in some additional loss in a period where FSH exceeds the steady-state turbine power.

The results that are obtained from visual inspection are supported by Fig. 5.6 where the resulting $P^*_{net,av}$ for each operating policy is presented. FSH avoids 53% of the losses associated with MSH. This result emphasizes that operating at minimal superheat is not necessarily always the best policy. The behavior can be implemented in a control strategy, albeit imperfectly, without knowledge about the future exhaust conditions.

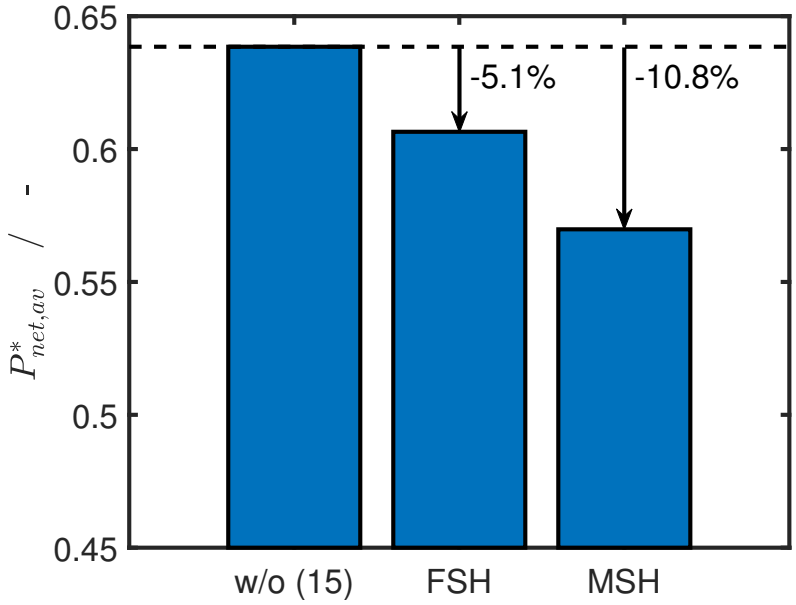

Figure 5.6: Normalized net average power produced for both policies compared to the case where no power limitation occurs (i.e., without constraint (5.5)). Clearly, FSH exhibits superior performance over MSH.

5.5.2 Power limitation with high exhaust gas mass flow

As can be seen from Fig. 5.4e, the WF outlet temperature is briefly maintained at its upper bound. The optimizer is, however, capable of preventing the use of the exhaust bypass valve by increasing the pressure and choosing a suboptimal turbine speed. It is clear that either a higher exhaust gas mass flow, temperature or longer duration of the power limitation will result in a situation, where it will be required to bypass some of the exhaust gas which will reduce the benefits of FSH. To assess such a scenario, we increase the exhaust gas mass flow chosen in Chapter 5.5.1 by 5% to $\dot{m}^*_{exh} = 0.211$ and solve the same optimization problems.
The resulting signal of the exhaust bypass valve position and the resulting trajectory of the WF outlet temperature are presented in Fig. 5.7. For FSH, the exhaust gas bypass valve is partially opened between $t \approx 300$ s and $t \approx 400$ s to avoid the WF from exceeding the temperature limit and a portion of the exhaust gas is bypassed (Fig. 5.7a). It should be noted that the exhaust bypass valve is reopened before $t = 400$ s in anticipation of the end of the power limitation so that the WF temperature reaches its upper bound exactly at that point in time (Fig. 5.7b). This behavior requires a priori knowledge of the exhaust gas profile and cannot be directly included

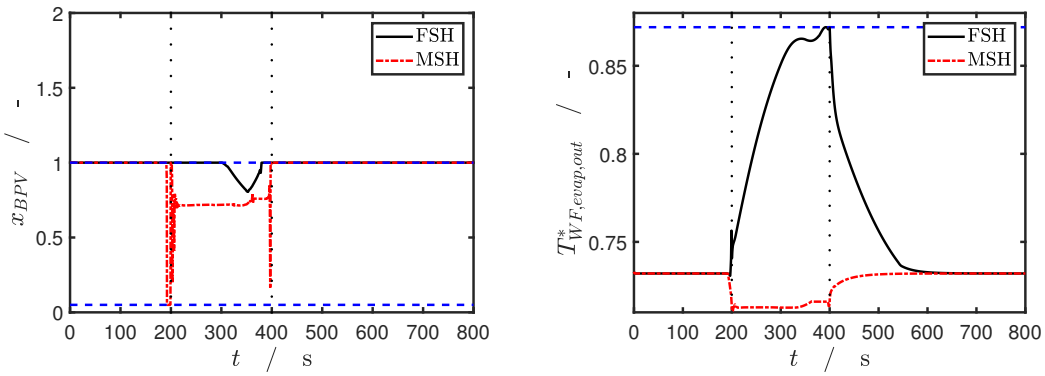

(a) Bypass valve position (b) WF evaporator outlet temperature

Figure 5.7: Results of the optimization for the power limitation case, dashed blue lines indicate lower and upper bounds.

in the control strategy. Rather, the valve would be opened once the power limitation would end. The losses associated with this fact, however, should be negligible.
For MSH, the qualitative behavior is similar to Chapter 5.5.1. As FSH requires bypassing a portion of the exhaust gas for the considered scenario, the avoided losses are smaller than in the previous case study, as can be seen from Fig. 5.8. Here, only 45% of the losses associated with MSH can be avoided. For higher exhaust gas mass flows, FSH consequently results in a reduced relative advantage. This would also apply for longer power limitations or higher exhaust gas temperatures. The results from this section suggest that the exhaust bypass valve will only be required for control as a manipulated variable to maintain safe operation. A general quantitative statement on the benefits of this strategy cannot be made here as it clearly depends on the system at hand and its operating conditions.

5.6 Implications on control strategy

In Chapter 5.4 we found that economically optimal dynamic operation exhibits occasional peaks in superheat for a highly transient exhaust gas profile and ethanol as WF. The gain in produced power, however, is negligible in comparison to operation at minimal superheat. As the knowledge of the exhaust gas conditions is unrealistic but required to exploit the effect and the resulting control action puts unnecessary strain on the actors, it is appropriate to operate the system at minimal superheat during regular operation. To obtain an optimal turbine speed, a separate optimization problem has to be solved. However, this can be approximated with a cheap steady state

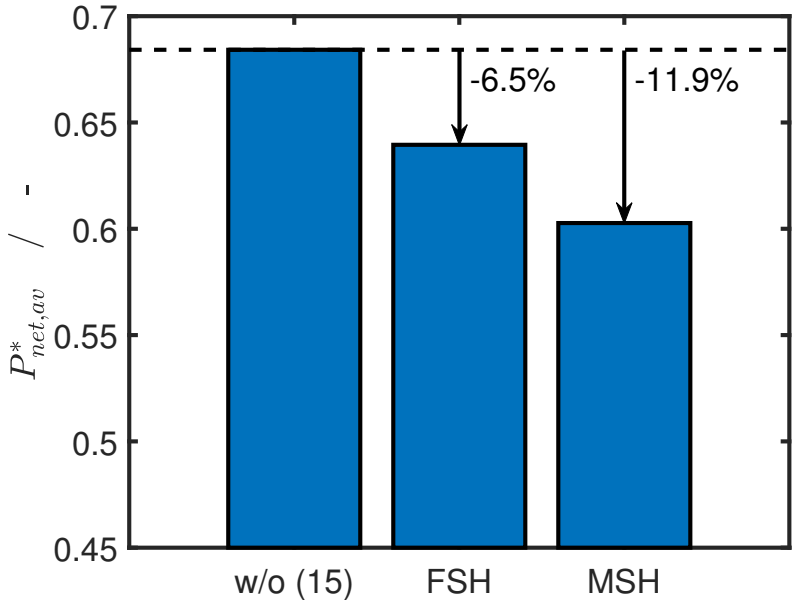

Figure 5.8: Normalized net average power produced for both policies compared to the case where no power limitation occurs (i.e., without constraint (5.5)) with $\dot{m}_{exh}$ increased by 5% compared to Fig. 5.6. The relative advantage of FSH over MSH shrinks when additional constraints become active.

optimization. The implications of further restrictions beyond safety constraints on the control strategy are more severe. In Chapter 5.5 we found that using a flexible superheat operating policy can be significantly more efficient than a minimal superheat operating policy when the turbine power output is temporarily limited. This result does not depend on a priori knowledge and can be implemented in control strategies. It implies to track a turbine power set-point by adjusting WF mass flow and turbine rotational speed. To achieve this, a steady-state optimization could be carried out that aims at satisfying the power constraint while minimizing WF mass flow to guarantee maximal superheat. The exhaust bypass valve should only be used to guarantee satisfaction of safety constraints once another constraint becomes active. The system should then be operated at the steady-state which satisfies this additional constraint.

5.7 Conclusion

In this chapter, we assessed the optimal operation of an ORC system for waste heat recovery in a heavy-duty diesel truck. We obtained optimal trajectories for the DOF

by means of dynamic optimization with the open-source software tool DyOS [185]. We compared an operating policy that maximizes the net work (FSH) with a policy that maintains minimal superheat while maximizing turbine power (MSH).
First, we assessed optimal operation of the WHR system in a transient driving cycle. Results obtained with FSH indicate that, most of the time, it is best to operate the system at minimal superheat, which is in agreement with literature for steady-state operation. However, peaks in superheat do occur but gains in power compared to MSH are negligible. Further, the occurrence of superheat peaks appears to be fluid-specific. Hence, we recommend operating the system at minimal superheat in such situations. This notion is reflected in many published studies on ORC control.
When further limitations apply, MSH can be suboptimal. This is illustrated for the case of a limitation in permissible turbine power. For the scenario where we assume constant exhaust gas mass flow and temperature and a temporary constraint on the turbine power, FSH reveals that during that period, increased superheat is greatly beneficial. The optimizer exploits that thermal energy which cannot be utilized during the power limitation can be stored in the heat exchanger wall for later use. In the examined case, this avoids 53% of the power losses resulting from MSH. Further investigations reveal that the relative advantage of FSH shrinks in scenarios where other constraints become active. Eventually, the exhaust bypass valve has to be opened and part of the exhaust gas cannot be used as otherwise the maximum WF temperature would be exceeded. For the examined case, the avoided losses drop to 45%. A similar effect is expected to apply when the duration of the power limitation is increased. In contrast to the work by Ghasemi and coworkers [43], the behavior observed in this work is due to dynamic effects. The optimizer exploits that, by temporarily storing thermal energy through increased superheat, more power can be produced overall.

Chapter 6

Control system design for the ORC system

6.1 Introduction

As discussed before, ORC operation in vehicles results in challenges, which are not encountered in traditional ORC applications. These require careful consideration of the control system for the ORC systems which is addressed in many publications. The proposed methods range from classical PID-type controllers [124] including feedforward term [118, 189], linear model predictive control (LMPC) with single [125, 127] or multiple models [190, 191], dynamic programming [47], to nonlinear model predictive control (NMPC) with regulatory objective [192] and economic NMPC (eNMPC) [123, 183]. NMPC is associated with high control quality, but also with high computational cost, making on-board implementation questionable. Fast NMPC methods (Chapter 2.3.3) that approximate the NMPC solution have been applied to WHR in vehicles and real-time capability was reported on desktop computers [153, 193]. For an overview of this class of control algorithms we refer to [26]. Furthermore, explicit NMPC [194] has been proposed to address the high computational demand of NMPC. Recent works also compare advanced model-based controllers to PI controllers [153, 193, 178]. In [153], a real-time iteration (RTI) scheme [195] is implemented with ACADO [196] for a parallel heat exchanger WHR system. The NMPC scheme is found to result in a significantly higher net power production (about 9 %) than PID-based control, which is predominantly due to the latter failing to meet the superheat constraint resulting in the turbine being bypassed. In [193], a RTI scheme with economic objective including moving horizon estimation is implemented for a single heat

exchanger system and compared to a PID controller and a LQR. The authors find that the eNMPC scheme only improves power production by about 2 % compared to the other controllers. In [178], three different advanced control strategies are compared for a system with a single heat exchanger. While NMPC with tracking objective and dynamic programming with economic objective yield similar net power production, a PID-based strategy results in significantly lower net power production. This is predominantly due to intermediate bypassing of the turbine as the superheat constraint is not satisfied at all times.

While many control-related contributions focusing on the development and performance evaluation of particular controllers are available, comparatively few publications address what constitutes optimal operation/control for the considered ORC system. Answering this question requires considerations on (i) what are the control objectives and (ii) which degrees of freedom should be employed to control the system. These points are addressed to some extent in [63, 176] and [177]. We used dynamic optimization to find optimal operating policies for characteristic operating scenarios in Chapter 5. There, we compared operation at minimal superheat to optimal economic operation with flexible superheat. For a scenario, where no operational constraints besides minimal superheat become active, we found that economically optimal system operation included several peaks in superheat similar to those in the fuzzy logic strategy in [177]. However, as the additional produced power is small, we proposed to operate at minimal superheat. Further, we found, in line with [63], that working fluid (WF) mass flow should be the main actuator and the evaporator bypass should only be used to satisfy operational constraints. This can for example be necessary when, temporarily, only a limited amount of recovered power can be utilized. In this situation, we found that operating at increased superheat can improve overall power production. Our findings indicate that it is crucial to consider the system dynamics for optimal operation and stress the need for energy management approaches, as e.g., [197].

In this chapter, we transfer our findings from Chapter 5 to a control strategy. We implement a NMPC scheme based on single shooting which solves each instance of the optimal control problem (OCP) to convergence. Using this scheme, we develop (i) a controller with economic objective function and (ii) a controller with regulatory objective function. For comparison, we implement (iii) a PI controller with feedforward term. Subsequently, we test the controllers in-silico with the ORC model used in Chapter 5 on a driving cycle with highly transient disturbances. The aforementioned contributions that include comparisons between advanced model-based controllers and PI controllers [153, 193, 178] focus on developing real-time capable advanced control strategies. In contrast, our focus is on discussing different approaches to the control

problem and assessing the limit of the economic benefit of NMPC over decentralized control strategies under idealized assumptions. We show that (i) the multi-variable control problem can be addressed by a decentralized control structure without significant loss of performance assuming an ideal condenser and (ii) employing a PI controller with feedforward term leads only to small losses in produced power compared to NMPC.
In the case study, we assume that the power produced can be fully utilized at all times. Note that irrespective of whether the expansion machine is mechanically coupled to the powertrain or connected to a generator, situations may occur, where the amount of power that can be utilized is limited. Such a situation would require an energy management system that switches to a different operating regime (as outlined in Chapter 5) and is not considered herein.
The remainder of this chapter is structured as follows. We introduce our modeling assumptions and the process model in Chapter 6.2 followed by a presentation of the examined control strategies in Chapter 6.3. We present a case study based on the World Harmonized Transient Cycle (WHTC) in Chapter 6.4 and present conclusions in Chapter 6.5.

6.2 Investigated system

We consider the model from Chapter 3 with the simplifications introduced in Chapter 5. The available inputs for manipulating the system are the WF mass flow rate $\dot{m}_{WF,in}$ set by the pump, the turbine rotational speed n_{turb} and the exhaust gas bypass valve position x_{BPV}. As the turbine operates at supersonic conditions, n_{turb} does not affect the WF outlet mass flow from the evaporator [63]. Our findings from Chapter 5 indicate that, for a typical driving cycle, the exhaust gas bypass valve position can be fixed so that all exhaust gas passes through the evaporator and power production is maximized. Consequently, we do not consider x_{BPV} as a degree of freedom (DOF) in this chapter. The disturbances are $\dot{m}_{exh}$ and $T_{exh,in}$. We only consider nominal operation, i.e., the fluid enters the evaporator as subcooled liquid and exits as superheated vapor. Thus, we do not require a switching model as developed in Chapter 4.

6.3 Examined control strategies

In this section, we first discuss the control objectives, the DOF considered for controlling the system and we describe the considered control structures based on our findings from Chapter 5 (Chapter 6.3.1). Then, we present (i) the eNMPC, (ii) the

NMPC (both in Chapter 6.3.2) and (iii) PI controller with feedforward term (PI-ff) in Chapter 6.3.3.

6.3.1 Considered control structures, objectives and degrees of freedom

The ultimate objective of a WHR system in a vehicle is to reduce fuel consumption. Assuming that the produced power can always be fully utilized, the control objective is to maximize produced electric power while achieving safe operation by manipulating the considered DOF ($\dot{m}_{WF,in}$, n_{turb}). For eNMPC, we can directly formulate the economic objective function accordingly and for all MPC controllers, we have to determine adequate constraints. Herein, we refer to control structures, where not all DOF are controlled by one controller as decentralized control structures. To translate the objective of maximizing power production into a decentralized control structure, we need to pair controlled variables with the DOF and specify adequate set-points.
A variety of decentralized control structures has been suggested in literature and distinction has to be drawn between ORC system with volumetric expanders, where the expander speed influences the WF mass flow rate [198] and supersonic turbines, where this is not the case [63]. For volumetric expanders, it is proposed to use pump mass flow to control superheat and expander speed to control evaporating temperature [118]. For turbines, using pump mass flow to control superheat is a sensible choice [63]. The control structure can be extended by using the exhaust bypass to additionally control pressure [176]. This additional control loop could be used by an energy management system to adjust the power output. In works with MPC, authors either choose a regulatory objective function that minimizes the deviation from a superheat set-point [153] or a desired WF temperature [192] (NMPC) or an economic objective function [183, 193] which maximizes net power production (eNMPC).
We assess the differences between MPC formulations with (i) economic objective function (eNMPC) and (ii) regulatory objective function (NMPC), with turbine operation being optimized separately in the latter case. Furthermore, we implement (iii) a PI controller with feedforward term that tracks a constant superheat set-point and uses the same turbine optimization procedure as (ii).

6.3.2 Nonlinear model predictive control (NMPC)

As discussed in Chapter 2.3, NMPC relies on a repeated solution of an OCP on a finite horizon. We solve the following OCP

$$\min_{\boldsymbol{u},s} \quad \int_{t_0^{OCP}}^{t_f^{OCP}} L\left(\boldsymbol{x}\left(t\right),\boldsymbol{y}\left(t\right),\boldsymbol{u}\left(t\right)\right) + \rho_{T_{sup}} s\left(t\right)\,\mathrm{d}t \tag{6.1a}$$

$$\text{s. t.} \quad \text{(2.2b)-(2.2f)}$$

$$\Delta T_{sup}^{min} - \Delta T_{sup}\left(t\right) - s\left(t\right) \leq 0 \qquad \forall t \in \left[t_0^{OCP}, t_f^{OCP}\right] \tag{6.1b}$$

$$0 \leq s\left(t\right) \qquad \forall t \in \left[t_0^{OCP}, t_f^{OCP}\right] \tag{6.1c}$$

on a horizon from initial time t_0^{OCP} to final time t_f^{OCP}. The objective function (6.1a) is of Lagrange-type with running cost function L. The running cost functions for eNMPC and NMPC are presented in Chapter 6.3.2.1 and Chapter 6.3.2.2, respectively. For WF superheat, we employ a soft constraint (6.1b) by introducing a non-negative slack variable s and adding a L1 penalty, weighted by $\rho_{T_{sup}}$, in the objective. Here, the path constraints are enforced at the control grid points. The horizon is divided into N_P control intervals of length Δt_C with $t_f^{OCP} = t_0^{OCP} + N_P \Delta t_C$. The optimizer can change the DOF for the first N_C intervals after which they are held constant. The DOF are discretized as continuous piece-wise linear functions in open-loop optimization. Note that this does allow for discontinuities of the controlled variables in closed-loop. After a solution is found, the control signal is sent to the process and the problem is re-solved after one sampling interval Δt_S with t_0^{OCP} and t_f^{OCP} shifted by Δt_S.
We solve the optimal control problems with the open-source tool DyOS [185] using single shooting and warm-start the algorithm with the optimal solution from the previous time-step. The integrator is NIXE [199] and the optimizer is SNOPT [89]. Since we aim to show that similar control performance as with NMPC can be achieved using simpler methods, we use full state feedback for specifying the initial state $\boldsymbol{x}_0$ in (2.2d), as it provides an upper bound on NMPC performance. The application of state estimation to an ORC system is shown in [153] with an unscented Kalman filter, in [178] with an extended Kalman filter and in [193] with moving horizon estimation. We determine the slack penalty weights based on the Lagrange multipliers of the hard constrained problem [200].

6.3.2.1 Economic NMPC

Assuming that the power produced by the turbine can be fully utilized, optimal economic operation is equivalent to maximizing net power output. Thus we set

$L(t) := -(P_{turb}(t) - P_{pump}(t))$ in (6.1a) for eNMPC. The controller adjusts $\dot{m}_{WF,in}$ and n_{turb} simultaneously. A schematic control structure is provided in Fig. 6.1.

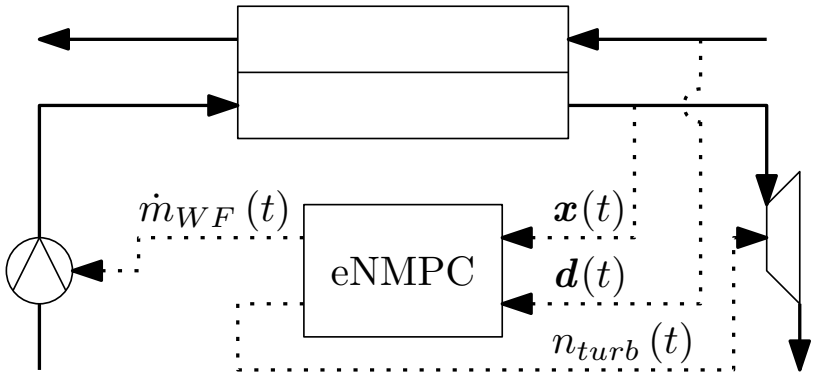

Figure 6.1: Control structure for eNMPC. Dotted lines indicate measurement and control signals.

6.3.2.2 Standard NMPC

In order to obtain good economic performance from NMPC, we have to choose a suitable controlled variable. Following ideas from self-optimizing control [164], we use the NMPC to force the process to operate a constraint. We design the NMPC to enforce minimal superheat, i.e., we set $L(t) := \left(\Delta T_{sup}(t) - \Delta T_{sup}^{min}\right)^2$ in (6.1a) as it is typically the active constraint in economically optimal operation (Chapter 5). Controlling the superheat constraint is convenient, as the set-point is independent of the operating conditions as opposed to, e.g., tracking an optimal pressure trajectory, but still leads to inherently optimal operation. For this objective, NMPC uses only $\dot{m}_{WF,in}$ as DOF.
Since the turbine rotational speed does not affect the WF conditions at the evaporator outlet, the objective function does not exhibit a sensitivity with respect to n_{turb}. Consequently, we determine n_{turb} in an online steady-state optimization, solved at each sampling instance of the NMPC, using `fmincon` in Matlab to optimize turbine performance. Although, the problem is non-convex, we use a local solver to maintain comparability to eNMPC where also a local solver is used. Thereby, we reduce the control problem to a single-output problem in contrast to many publications in literature where two quantities out of $T_{WF,out}$, ΔT_{sup} and p are controlled. Splitting the two optimizations is possible as the turbine rotational speed only serves to optimize turbine operation [63], which is typical for turbine expansion, but cannot be generalized to any expansion machine. A schematic representation of the control structure

is provided in Fig. 6.2.

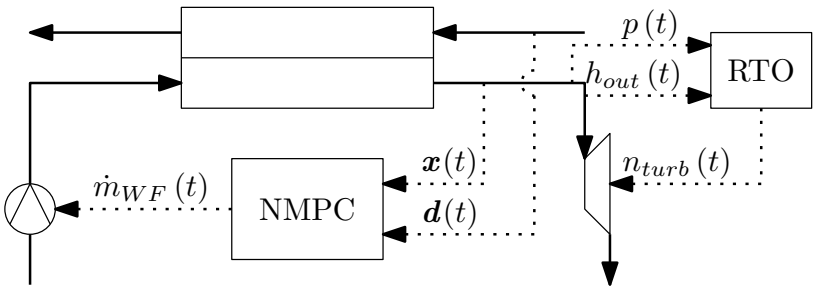

Figure 6.2: Control structure for NMPC. Dotted lines indicate measurement and control signals.

6.3.2.3 Operating constraints

In the considered case study, the scaled pressure p^*, the scaled WF evaporator outlet temperature $T^*_{WF,evap,out}$ and the evaporator superheat ΔT_{sup} are path constrained. The lower bound on p^* reflects the minimal pressure ratio of the turbine. Since we assume condenser operation at ambient pressure, we can directly express this as a function of the high pressure. The upper bound on p^* is a safety constraint, the upper bound on $T^*_{WF,evap,out}$ prevents WF degradation and the lower bound on ΔT_{sup} prevents damage to the turbine by droplet formation. We formulate the path constraint for ΔT_{sup} as a soft constraint and the constraints for $T^*_{WF,evap,out}$ and p^* as hard constraints. We implement the soft constraint since, in contrast to the dynamic optimization case study in Chapter 5, no prediction of the disturbances is available in a control setting. We expect that, as a consequence, it will not be possible to satisfy the constraint at all times. The lower and upper bounds for the path constraints and the input constraints are listed in Tab. 6.1. Our choice of the lower bound of ΔT_{sup}

Table 6.1: Bounds of path constraints and DOF.

Path				DOF			
Variable	Unit	LB	UB	Variable	Unit	LB	UB
ΔT_{sup}	K	20	-	$\dot{m}^*_{WF,in}$	-	0.0073	0.0363
$T^*_{WF,evap,out}$	-	-	0.8719	n^*_{turb}	-	0.82	1.09
p^*	-	0.3	1.5				

is more conservative than in the previous Chapter, due to the unknown exhaust gas

conditions in a control setting. The rationale is to provide additional back-off so that the controllers are able to maintain superheat above the limit of 10 K defined in Chapter 5.

6.3.3 PI with feedforward term (PI-ff)

We use a PI controller with feedforward term to track a superheat set-point using the WF mass flow as DOF

$$\dot{m}_{WF,in}(t) = K_P \cdot e(t) + K_I \int_{t_0}^{t} e(t)\,\mathrm{d}t + \dot{m}_{WF,ff}(t)\ , \tag{6.2}$$

where $e(t) = \Delta T_{sup}^{set} - \Delta T_{sup}(t)$ is the control error, t_0 indicates the initial time of the simulation and $\dot{m}_{WF,ff}$ is the feedforward term. Since we want the feedforward term to account for the dynamic response of the system, it tracks the optimal steady-state input $\dot{m}_{WF,ss}^{opt}$ according to the following differential equation

$$\dot{m}_{WF,ff}(t) + \tau_{ff}\frac{\mathrm{d}\dot{m}_{WF,ff}}{\mathrm{d}t} = \dot{m}_{WF,ss}^{opt} + \tau_z\frac{\mathrm{d}\dot{m}_{WF,ss}^{opt}}{\mathrm{d}t}\ , \tag{6.3}$$

where τ_{ff} and τ_z are time constants, which can be tuned to obtain a suitable dynamic behavior of the feedforward term. Accordingly, in offset-free steady-state operation the PI-ff control action is $\dot{m}_{WF,in} = \dot{m}_{WF,ss}^{opt}$. Note that also the rate of change of the disturbances is considered on the right hand side of (6.3). This feedforward policy is in accordance with [178], where the exhaust gas temperature rate of change was found to be an important input in the dynamic programming strategy.
We provide the optimal steady state input as a map $f_{map}(\dot{m}_{exh}, T_{exh,in})$ which we determine by solving steady-state optimizations with varying heat source conditions offline and fitting the correlation with a polynomial cubic in $\dot{m}_{exh}$ and linear in $T_{exh,in}$ (Fig. 6.3). Similar to NMPC, PI-ff controls the WF mass flow rate only. We determine n_{turb} in a separate online steady-state optimization to obtain optimal turbine operation. A schematic representation of the PI-ff control structure is provided in Fig. 6.4.

6.4 Case study

6.4.1 Exhaust gas data

In this case study, we consider exhaust gas data (Fig. 6.5) used in Chapter 3 for model validation and in Chapter 5 as a dynamic optimization case study. The disturbance

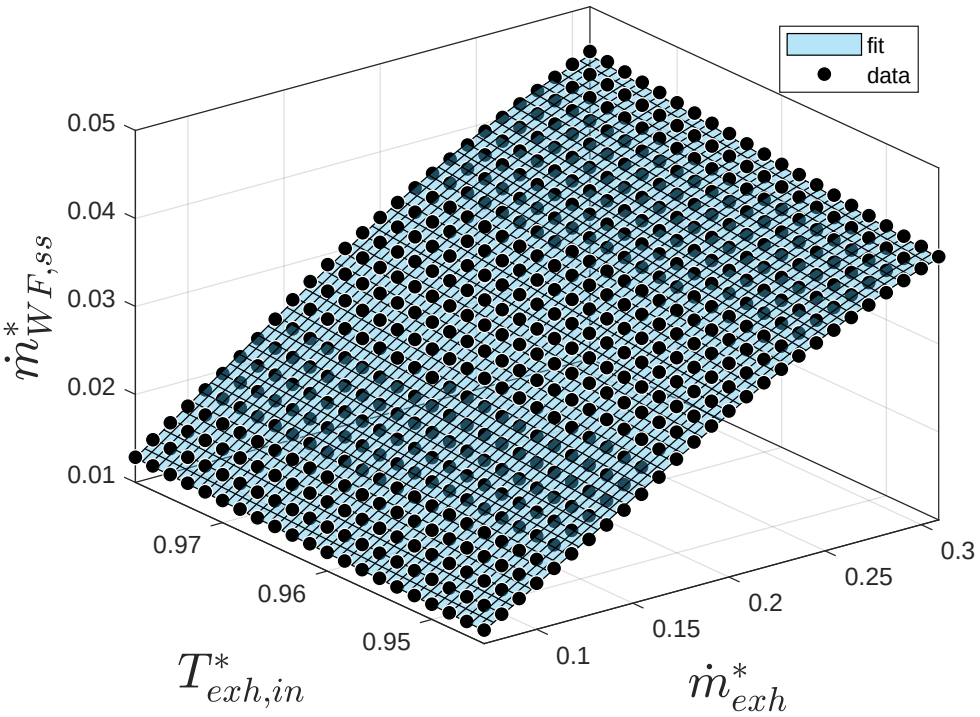

Figure 6.3: Polynomial fit of optimal steady-state WF flowrate as function of disturbances. The data points were obtained by steady-state optimization.

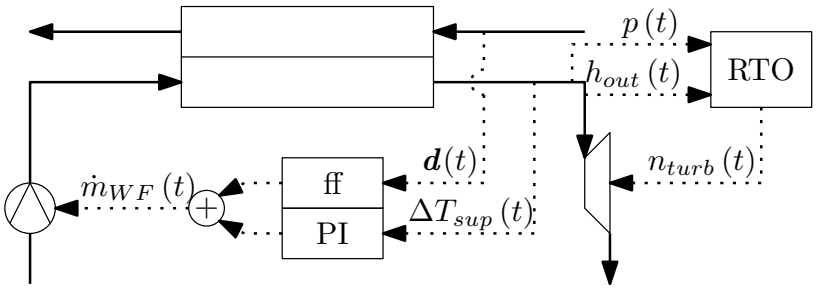

Figure 6.4: Control structure for PI-ff. Dotted lines indicate measurement and control signals.

values and their time derivatives are measured at every controller sampling instant but no prediction of the disturbances is available. The same exhaust gas mass flow and temperature data is used with all three controllers. We assume no feedback delay and no plant-model mismatch, i.e., we use the ORC system model for the controller and as a plant surrogate, to obtain an upper bound on NMPC performance.

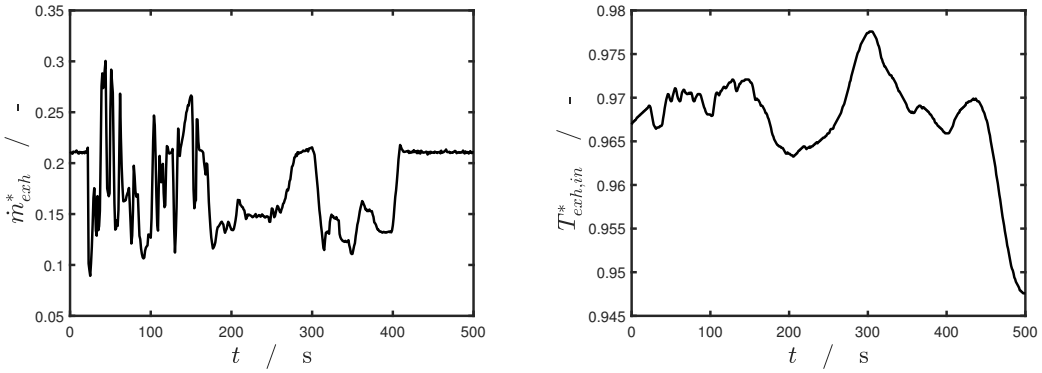

(a) Exhaust gas mass flow

(b) Exhaust gas temperature

Figure 6.5: Exhaust gas data for the case study.

6.4.2 Tuning of the controllers

Tuning parameters for the controllers are presented in Tab. 6.2. For NMPC, we

Table 6.2: Parameters for NMPC and PI-ff controller used in the case study.

	Parameter	Value	
PI-ff	K_P	-8.64×10^{-4} kg K^{-1} s^{-1}	
	K_I	1.65×10^{-6} kg K^{-1} s^{-2}	
	τ_{ff}	12.0 s	
	τ_z	1.35 s	
	ΔT^{set}_{sup}	20 K	
NMPC		economic	tracking
	N_P	5	5
	N_C	5	5
	Δt_C	8 s	8 s
	Δt_S	1 s	1 s
	$\rho_{T_{sup}}$	8 kW K^{-1}	75 K
	ΔT^{set}_{sup}	-	20 K

determined N_P and Δt_C by implementing various combinations and choosing the parameters that gave a feasible solution at the smallest computational cost (i.e., small N_P at given Δt_C). We set $N_P = N_C$ as is commonly done in nonlinear model predictive control [97].

We tuned PI-ff using dynamic optimization with the objective of minimizing the squared deviation from the superheat set-point and the same exhaust gas data as in the test cycle. To validate the control law, we used data from another cycle and found PI-ff to work well. We choose $\Delta T_{sup}^{set} = 20$ K in accordance with the lower bound specified in Chapter 6.3.2.3.

6.4.3 Simulation results

The results for eNMPC, NMPC and the PI-ff are presented in Fig. 6.6. As can be

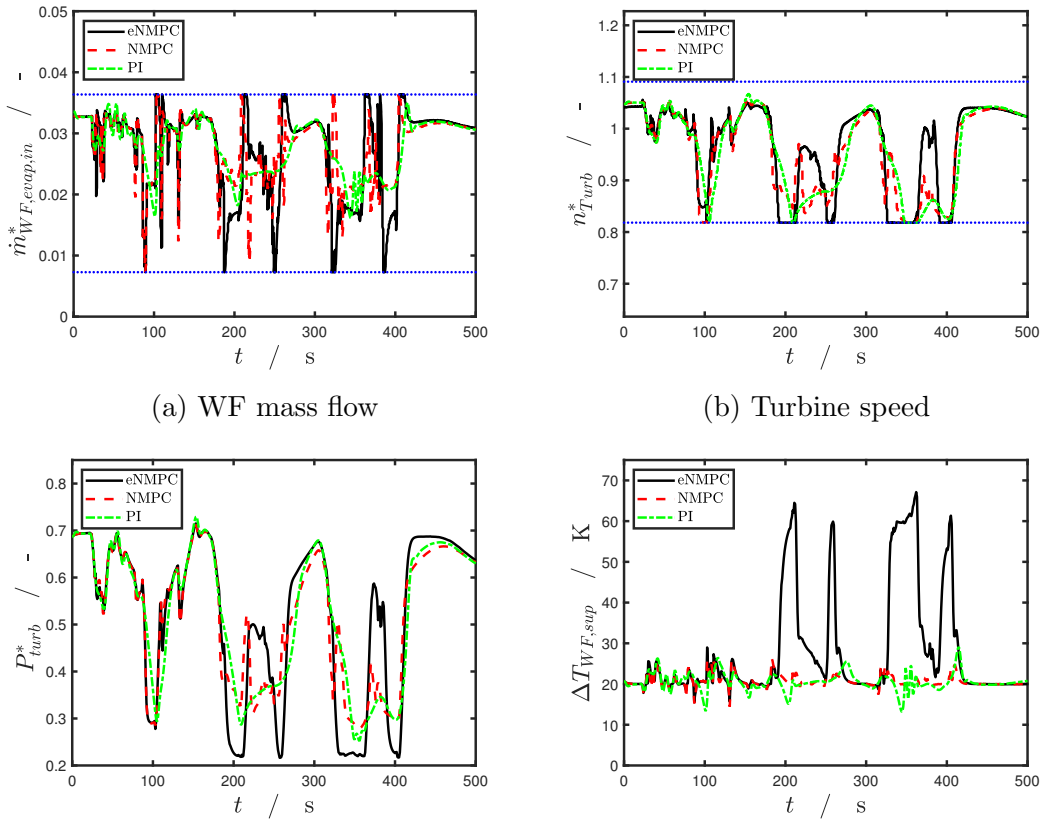

(a) WF mass flow

(b) Turbine speed

(c) Turbine power

(d) Superheat

Figure 6.6: Results for eNMPC, NMPC and PI-ff. Input constraints are indicated by the blue dotted lines.

seen, significant peaks in superheat occur in eNMPC (Fig. 6.6d). This reflects results found in Chapter 5 and similar results can be seen in [201], however, since no disturbance prediction is available, this behavior is surprising. Apparently, the advan-

tages of temporarily operating at increased superheat observed in Chapter 5 can also be leveraged without knowledge of future disturbances. Every new measurement of the disturbance is a step change for the optimizer compared to the previous instant. When we researched the phenomenon for Chapter 5, we found that superheat peaks are present in the optimal solution for step experiments when the steps in $\dot{m}_{exh}$ are of sufficient duration. In agreement with this observation, the peaks in superheat occur from $t \approx 200\,\mathrm{s}$ on, where the profile for $\dot{m}_{exh}$ is smoother than in earlier periods.
PI-ff is able to track the superheat set-point well and maintains the system above a superheat threshold of $\Delta T_{sup} = 10$ K. The performance is mostly comparable to NMPC which is also able to track the superheat set-point with a maximum deviation of less than 10 K. Since, all controllers stay above this threshold, we do not consider bypassing the turbine herein. However, PI-ff operates below the superheat set-point more often and for more prolonged periods than NMPC. This is mostly in situations where a fast decrease in $\dot{m}_{WF,in}$ is required and the PI controller does not act with the same speed as the idealized model-based controllers (Fig. 6.6a). In a case where the violation of the superheat constraints results in the turbine being bypassed, these periods would significantly decrease power production. Thus, it is important to find good tuning parameters and to choose sufficient back-off for the superheat set-point. On the other hand, the PI-ff control profile for $\dot{m}_{WF,in}$ (Fig. 6.6a) is much smoother than for the eNMPC and NMPC. Consequently, operation is less straining for the components and a longer lifetime could be expected.
The separation of the turbine optimization in the tracking NMPC strategy appears to have no detrimental effect on system performance. In fact, notable differences in turbine speed for eNMPC and NMPC (Fig. 6.6b) only occur in concordance with peaks in eNMPC superheat. Before the first peak occurs (shortly before 200 s), there is no visible difference in turbine power production for eNMPC and NMPC (Fig. 6.6c).
As in Chapter 5, we assess the examined strategies by comparing average scaled net power (5.1), presented in Tab. 6.3. From the table, we make two main observations.

Table 6.3: Average scaled net power for eNMPC, NMPC and PI-ff.

	$P^*_{net,av}$
eNMPC	0.516
NMPC	0.514
PI-ff	0.513

First, splitting the control problem in a superheat set-point tracking task and separate turbine optimization yields similar power production to eNMPC while reducing the

control problem to a single-input single-output problem. In fact, the losses in power produced are less than 0.5 %. Second, the decoupled problem can be conveniently addressed with a PI controller with marginal performance losses compared to much more complex model-based control. This finding is in agreement with literature where 2 % losses of PI controller compared to eNMPC are reported [193]. The much higher losses associated with a PI controller in [153] and [178] are mostly due to intermediate turbine bypassing when the superheat constraint is violated. This implies that for a PI controller, a set-point with sufficient back-off from the superheat constraint should be chosen as the resulting losses in produced power are moderate compared with the losses of temporarily bypassing the turbine. We found that increasing the superheat set-point by 5 K reduces produced power by about 1 %. Note that in [153] a double heat exchanger system was examined which is harder to control.
Using a prediction of the disturbance in NMPC is proposed in [186]. In case of a perfect disturbance prediction, we find that PI-ff produces roughly 2 % less power than eNMPC and NMPC. Furthermore, the improved NMPC superheat constraint compliance would allow to reduce the superheat set-point, a result also observed in [186].
Our results imply that NMPC has only small advantages over more traditional control strategies. Due to the specific system topology, the control problem effectively reduces to a SISO problem, thus eliminating potential advantages of a centralized control structure. Furthermore, the economically optimal control policy can be approximated with small losses by tracking minimal superheat. Finally, sufficient back-up can compensate for the slightly poorer tracking performance of a PID-type controller and ensure that the turbine is not bypassed at moderate economic cost.

6.5 Conclusion

Controlling an ORC on board of a vehicle operated in street traffic is a challenging task. The system has to be operated safely and efficiently under highly transient heat source conditions. Control updates have to be made at high frequency and the control algorithm has to be executed on on-board hardware with limited computational resources.
Based on our findings from Chapter 5, we proposed and assessed several control strategies in this Chapter. We compared the performance of a nonlinear model predictive control algorithm (NMPC) and a PI controller with feedforward term (PI-ff). Furthermore, we discussed how the economic optimal control problem with two DOF can be recast as a single-input single-output tracking control problem and an additional

steady-state optimization.
We compared the proposed controllers in a case study containing parts of the WHTC. From the results we deduced two main findings. First, decomposing the control problem into two simpler subproblems results only in small losses with respect to power production. This decomposition reduces the optimal control problem to a single-input single-output problem which reduces the computational load for model-based algorithms and allows for convenient use of a single PI controller. Second, losses from using the PI controller with feedforward term are small with 0.5 % less energy recovered than with economic NMPC. Even when we assumed perfect disturbance predictions, this value only increased to about 2 %.
These results imply that it is unlikely that a vehicle manufacturer would use NMPC for ORC in a vehicle. It has to be considered that the benefits of NMPC only apply to the amount of fuel saved which optimistic estimates put in the range of 5 % so that the additional overall fuel saving resulting from using NMPC would be in the range of 0.1 %. Our idealized NMPC framework is not real-time capable. Others have achieved real-time capability using fast-update algorithms with ACADO [153] and their own RTI implementation [193], albeit on desktop computers. However, even if real-time capability could be achieved on-board, it is questionable whether the small gains in power production are sufficient to outweigh the advantages of PID control, including small development cost compared to NMPC.
When a decentralized control structure is chosen, designing an overall energy management system [197] is an important task. This system should consider all conceivable conditions (e.g., limited cooling capacity) which could affect ORC operation. As shown in Chapter 5, dynamic optimization can be a valuable tool to understand optimal system behavior and draw conclusions on a suitable decentralized control strategies. In this Chapter, we have not considered a scenario where the amount of power that can be utilized is temporarily limited. For this, we would require an energy management system that first reduces power production through manipulation of WF mass flow and turbine speed and switches to a mode where the exhaust bypass valve can be utilized when other constraints (e.g. maximum WF temperature) become active. An interesting extension would be the consideration of the condenser, which to date has not been adequately addressed in literature. In particular, it would be interesting to assess the effects on the economically optimal operation when a cost for cooling could be quantified (e.g., additional power consumption of radiator fan).

Chapter 7

Approximate NMPC for the ORC system using machine learning

7.1 Introduction

As we have seen in Chapter 6, the ORC system considered in this thesis can be efficiently controlled using a PI controller with feedforward term. For more complex architectures or systems with fixed-displacement expanders, however, this might not be the case as the number of DOF increases. Here, NMPC might be required to achieve safe and efficient operation. Albeit CPU times of less than 100 ms for solving an NMPC problem for WHR in a truck have recently been reported on a desktop computer [201], implementation on in-vehicle hardware remains questionable. In general, NMPC is increasingly investigated for automotive applications and limited computational resources on in-vehicle hardware can be prohibitive [202]. Thus, we use our ORC system in this chapter to examine one approach to reduce the online computational demand for NMPC.

Several ideas to reduce the computational costs of NMPC are available. Explicit MPC [25] exploits that the solution of MPC is parametric in the systems state variables and to solve the parametric problem a priori. While the approach exhibits strong theoretical foundations in terms of its stability properties, solving the parametric problem scales badly for increasing state vector size. Another method, which has been revisited recently, is to learn the NMPC control policy using machine learning techniques e.g., [203, 27, 204, 205, 206]. The approach is straightforward to implement, however, it suffers from the typical weaknesses of machine learning approaches, i.e., the course of dimensionality and little or no extrapolation capability.

Hence, it is of great significance to obtain a dense sampling of the state space and to ensure that the controller does not operate outside the sampled region. Lucia and Karg [27] showed that, in practice, an ANN-based controller might exhibit some extrapolation capabilities. In [206], it is proposed to combine an ANN-based controller with manifold learning techniques to achieve a simpler correlation to learn, especially for large-scale systems. In this Chapter we apply an ANN-based controller to an ORC waste heat recovery system for a heavy-duty diesel truck to establish a proof-of-concept for the application. Our focus is on maintaining a desired superheat set-point. The remainder of this chapter is structured as follows. We present the system considered and its model in Chapter 7.2. The method for gathering the training data and the training procedure are described in Chapter 7.3 followed by an evaluation of the controller performance in Chapter 7.4. We give our conclusions in Chapter 7.5.

7.2 Model description

We use the model equation from Chapter 3 with the simplifications made in Chapter 5. We focus on maintaining a desired superheat set-point at the heat exchanger WF outlet. As the turbine speed does not influence the WF state at the HX outlet, we did not implement a turbine model and the WF inlet massflow $\dot{m}_{WF,in}$ is the sole degree of freedom. The corresponding system boundary is depicted in Fig. 7.1. For

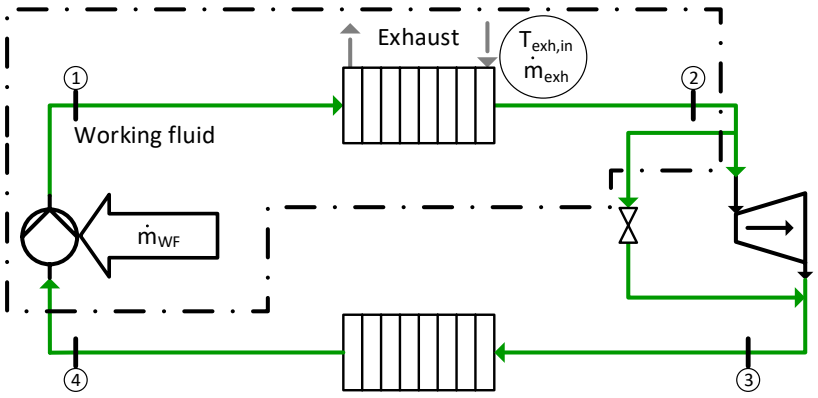

Figure 7.1: Topology of the examined system. The WF is indicated by the solid green line and the exhaust gas by the dashed gray line. The manipulated variable is indicated by the arrow and the disturbances by the circle. The system boundary for this work is indicated by the dot-dashed black line.

simplicity we assume constant heat transfer coefficients and a simple geometry typical for waste heat recovery in a truck instead of using our parameters from Chapter 3.

Key parameters for the model are specified in Tab. 7.1. Again, we assume "nominal

Table 7.1: Key heat exchange and geometry model parameters.

$\alpha_{i,0}$	$\alpha_{i,1}$	$\alpha_{i,2}$	α_{exh}	A	A_w	A_{Laval}	b_{WF}	b_{exh}	l_{tot}
	$\mathrm{W/\,(m^2K)}$				$\mathrm{m^2}$			m	
100	900	50	45	0.004	0.03	0.00002	12	80	0.3

operation" as defined in Chapter 3.

7.3 Method: Data acquisition and training

To learn the NMPC control law, it is of great significance to provide a set of data for training which adequately samples the state space. Recent efforts on ANN-based MPC, e.g., [27, 206], present chemical reactions in stirred tank reactors as a case study. Sampling the state space by providing a set of practically relevant initial conditions is straightforward for such systems and can be achieved by simply altering initial concentrations and reactor volume.
In contrast, it is complicated to provide a variety of physically meaningful initial conditions for the ORC system, in particular for wall temperatures and zone lengths. For example, it would make little sense to initialize the wall temperature of the superheated zone at a smaller value than the wall temperature of the subcooled zone. Such an initialization might even result in an infeasible DAE initialization or integration failure. We use an optimization-based procedure to address this issue. We solve 200 dynamic optimization problems using the open source tool DyOS [185], each starting from the same feasible initial point but with a different time-invariant exhaust gas massflow $\dot{m}_{exh}$. The optimizer minimizes the deviation of the superheat ΔT_{sup} at final time t_f from a desired superheat ΔT_{sup}^{des}, which is different in each run, thus achieving a set of well distributed initial points. As a degree of freedom, the optimizer can choose $\dot{m}_{WF,in}$ which is constant for each run. Thereby, and by choosing $t_f = 2000$ s we achieve that the system is effectively at steady-state at t_f. We provide 200 combinations of $\dot{m}_{exh} \in [0.1\ \mathrm{kg/s}, 0.6\ \mathrm{kg/s}]$ and a desired superheat $\Delta T_{sup}^{des} \in [10\ \mathrm{K}, 50\ \mathrm{K}]$ through latin hypercube sampling (LHS) and assume a constant exhaust gas inlet temperature of $T_{exh,in} = 600$ K. The objective function of the dynamic optimization problem reads

$$\min_{u} \quad \left(\Delta T_{sup}\left(t_f\right) - \Delta T_{sup}^{\ des,k}\right)^2 \tag{7.1}$$

$$\text{s. t.} \quad \text{(2.2b)-(2.2d), (2.2f)}$$

which is subject to (2.2b)-(2.2d) and (2.2f). For simplicity, we impose no path constraints.
We use the resulting steady-state optimal state vectors $\boldsymbol{x}^{opt,k}\left(d^k\right)$ as initial values for the following NMPC runs and combine them with a different LHS of $\dot{m}_{exh}$. We then carry out NMPC with these sets, minimizing the devations of the superheat trajectory from desired superheat of 30 K. The NMPC problem is solved repeatedly with a sampling time of $\Delta t = 5$ s and minimizes the integral over the prediction horizon N_P of the deviation from desired superheat.

$$\begin{aligned} \min_{\boldsymbol{u}(t),\boldsymbol{x}(t)} \quad & \int_{t_0}^{t_f} \left(\Delta T_{sup}\left(t\right) - 30 \text{ K}\right)^2 \mathrm{d}t \\ \text{s. t.} \quad & \text{(2.2b)-(2.2d), (2.2f)} \end{aligned} \tag{7.2}$$

Here, we chose a piecewise-constant discretization of the inputs $\boldsymbol{u}\left(t\right)$. We chose a control horizon $N_C = 8$ and a prediction horizon $N_P = 10$. The dynamic optimization problem was solved with DyOS at every sampling instant and the total duration of each run was 200 s, resulting in 40 samples per simulation.
A projection of the trajectories in the state space on pressure p and WF outlet enthalpy h_{out} of all 200 NMPC simulations is depicted in Fig. 7.2. We can see that we achieve a dense sampling in the state-space and that the trajectories converge to the desired superheat. The data is used for training the ANN and the amount of data is considered to be sufficiently dense to allow for effective interpolation. In total, we obtained the datasets $\mathbf{u}^* \in \mathbb{R}^{8000\times1}$, $\mathbf{x}^* \in \mathbb{R}^{8000\times7}$ and $\mathbf{d}^* \in \mathbb{R}^{8000\times1}$. The solution to the NMPC problem for our scenario is parametric in $\boldsymbol{x}$ and d. Consequently, we learn the mapping from those quantities to the optimal control policy. The NMPC controller provides the optimal sequence $\mathbf{u_k} := \left(u\left(t_k\right), u\left(t_k + \Delta t\right), \ldots, u\left(t_k + \left(N_c - 1\right)\Delta t\right)\right)$ over the control horizon consisting of N_C elements at every instance. However, as only the first calculated input of this sequence is applied to the plant before the NMPC problem is re-solved, we only learn the mapping for this quantity. The training process is illustrated in Fig. 7.3. We did not include ΔT_{sup}^{des} as an input to the ANN as it is fixed to 30 K. We trained the ANNs using the Levenberg-Marquardt algorithm in Matlab's Neural Network Toolbox [207] and assumed all states to be measurable, thus eliminating the need to implement state estimation.
Due to the parametric nature, the mapping is only dependent on the measured state and disturbance at the current time. Hence, we used a feedforward neural network with the hyperbolic tangent activation function. We tested several different ANN architectures by varying the number of hidden layers and the number of neurons per

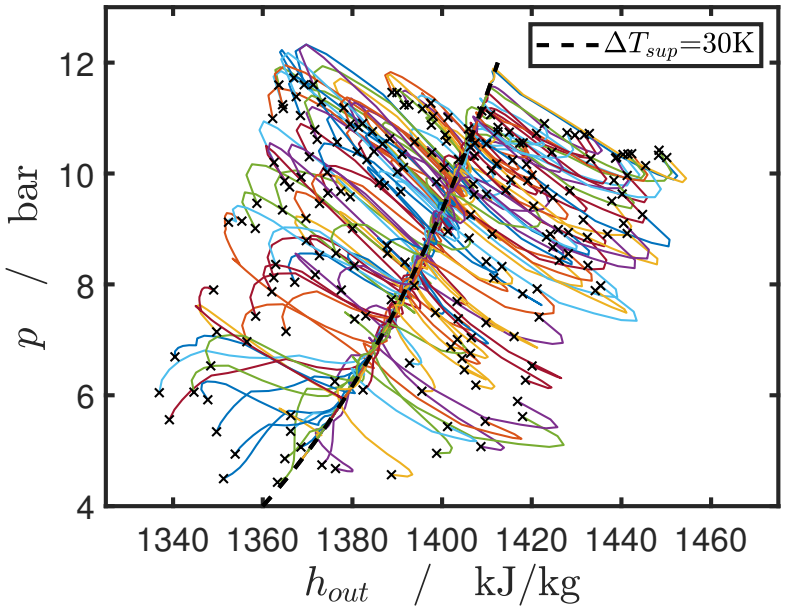

Figure 7.2: State space projection on p and h_{out} of the 200 NMPC simulations. Crosses indicate initial values. The controllers regulates the system to achieve the desired superheat.

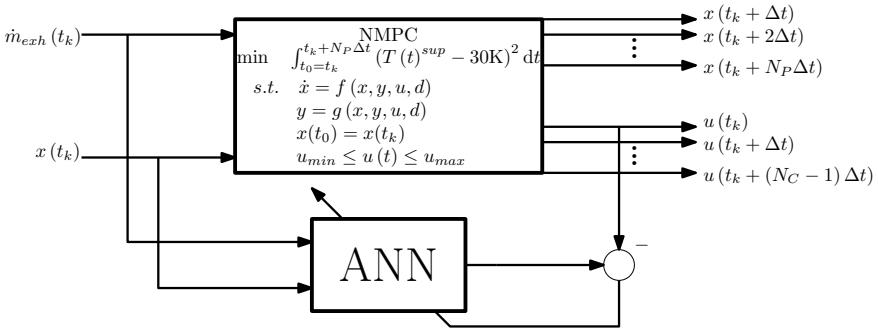

Figure 7.3: Illustration of the training process of the ANN. Only the first control input $u(t_k)$ is considered.

layer. In total we tested architectures consisting of one to four hidden layers consisting of 10, 20 and 30 neurons each. To obtain reliable results, we executed five training runs for each architecture.

We found that all trained ANNs achieved good results, differences in performance were small and even a shallow network with only one hidden layer consisting of ten neurons exhibited satisfactory performance. While this is an interesting observation,

we do not claim that it is generally true for learning NMPC policies as we solved a rather simple problem with only one manipulated variable here.

7.4 Case study

We test our proposed ANN-based controller in further scenarios in silico. To assess its performance, we compare the resulting control policy and deviations from desired superheat to the solution obtained by solving (7.2), (2.2b)-(2.2d), (2.2f). We used an ANN consisting of two hidden layers of 20 neurons each and we examined a total of ten structurally similar scenarios. All scenarios include two steps in the exhaust gas mass flow which, however, do occur at different times. To generate the different exhaust gas profiles, we sampled a LHS with three values for the different levels of $\dot{m}_{exh}$ and another LHS for the time-points where the steps occur. We obtained initial values with the procedure described in Chapter 7.3. However, to test the robustness of the ANN-based controller with respect to conditions not encountered during training, we sampled $\Delta T_{sup}^{des} \in [10\text{ K}, 60\text{ K}]$ and $\dot{m}_{exh} \in [0.1\text{ kg/s}, 0.65\text{ kg/s}]$.
We then solved these scenarios with the ANN-based controller and with NMPC and assumed that the solution can be computed without time delay. To compare both approaches we use the average deviation from the desired superheat ϵ_{avg}.

$$\epsilon_{avg} = \frac{\int_0^{t_f} \sqrt{\left(\Delta T_{sup}\left(t\right) - 30\text{ K}\right)^2}\mathrm{d}t}{t_f} \tag{7.3}$$

Tab. 7.3 presents the values of ϵ_{avg} for all executed simulations. In general, both con-

Table 7.2: Average deviation from desired superheat for all ten runs.

$\epsilon_{\mathbf{avg}}$ [**K**]										
Run	1	2	3	4	5	6	7	8	9	10
ANN	.109	.722	.447	.241	.996	.410	.847	.101	.280	.276
NMPC	.096	.636	.431	.241	.848	.319	.809	.100	.271	.244

Table 7.3: Average deviation from desired superheat for all ten runs.

trollers perform well in all scenarios with the average deviation always smaller than 1 K. However, NMPC exhibited slightly better performance for each run. Higher average deviation in certain runs does not necessarily indicate bad controller performance. In fact, it is predominantly due to deviations of the superheat from 30 K at the initial

point of the respective run. The average CPU time for obtaining the ANN-based control policy was 20 ms on a desktop computer with an Intel(R) Core(TM) i7-4790 CPU and 16 GB RAM.

For further assessment, we examine the scenario with the highest relative deviation between the ANN-based controller and NMPC controller, i.e., Run 6. The exhaust gas mass flow is provided in Fig. 7.4a. Interestingly, it is a scenario where one of the exhaust gas mass flow levels is outside the training set. This is in agreement with intuition as it can be expected that the loss in controller performance is larger for disturbances outside the training set. As in all scenarios in this manuscript, $T_{exh,in}$ remains constant at 600 K. Fig. 7.4c depicts the control action taken by the ANN-based controller and the NMPC controller. The resulting superheat is shown in Fig. 7.4d. The control policy computed by the ANN is initially identical to the sequence pro-

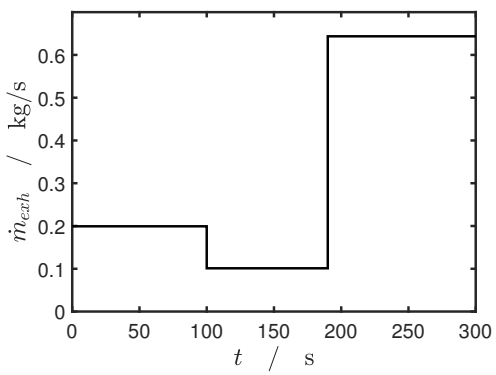

(a) Exhaust gas mass flow disturbance profile

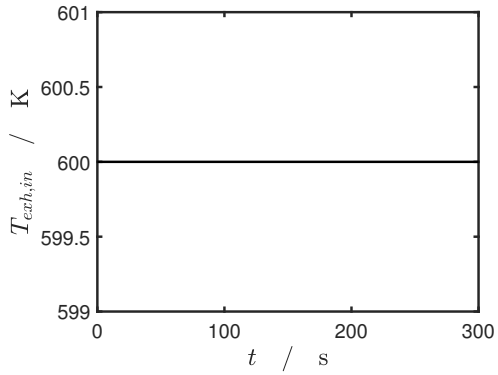

(b) Exhaust gas temperature disturbance profile

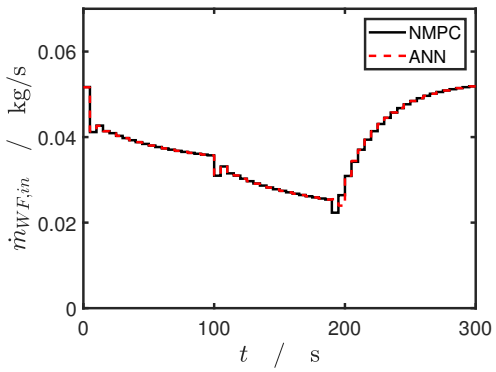

(c) Control input $\dot{m}_{WF,in}$

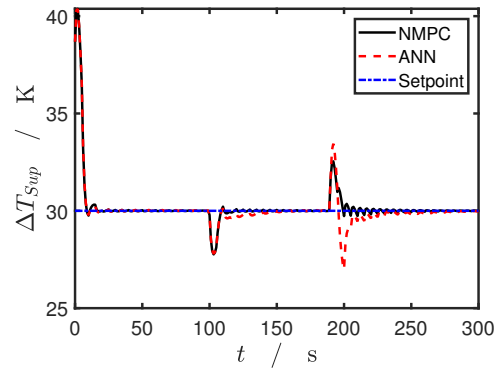

(d) Superheat

Figure 7.4: Disturbances, controls and resulting superheat for Run 6.

vided by NMPC. Both controllers react well to the change in $\dot{m}_{exh}$ at $t = 100$ s though

the ANN-based controller takes marginally longer to reach the desired superheat. The second step in $\dot{m}_{exh}$ occurs at $t = 190$ s and reaches a level outside the training set. Though the ANN-based controller is capable to reject this disturbance, the NMPC exhibits superior performance. The deviations for the ANN-based Controller remain, however, sufficiently small.

7.5 Conclusion

Nonlinear model predictive control of ORCs for waste heat recovery in vehicles is a challenging problem due to the transient and unpredictable heat source conditions, the limited computational resources and necessary high sampling rates. NMPC has been proposed for this system by several authors but typically requires significant model simplification. Large computational cost is a well known issue in many other NMPC applications and several approaches to overcome it have been developed.
In this Chapter, we presented a machine learning approach, where an ANN was used to learn the NMPC control policy as function of the system state and the measured disturbance. To obtain data for training, we solved to 200 NMPC simulations with varying initial conditions and exhaust gas mass flow. In those cases, we aimed to track a superheat set-point of 30 K. We trained the ANN-based controller using shallow and deep ANNs consisting of up to four hidden layers and up to 30 neurons per layer. Differences in performance were small and even the result for the smallest ANN with one hidden layer of ten neurons showed satisfactory performance. We then performed a case study where we executed ten NMPC simulations and compared the results to the ANN-based controller. Two steps of random height at random time-points occurred in the exhaust gas mass flow during these simulations. Further we included initial values and exhaust gas mass flows which were slightly outside of the training set. Our results show that the control policy learned by the ANN exhibits only small deviations from the solution of NMPC while requiring negligible computational expense. However, small deviations do occur, in particular when the disturbance changes while the system is at desired superheat but not yet at steady-state. This might improve when the training scenarios are modified.

Chapter 8

Accelerating NMPC through machine learning

8.1 Introduction

LMPC is the most frequently used advanced process controller in industry [92]. Explicit consideration of process constraints and natural handling of MIMO systems are among the prime properties for its success. NMPC and in particular eNMPC promise better results with respect to control performance [208] but are rarely used in industry, in part due to their high computational requirements. In many real-world applications, especially on embedded hardware, real-time capability cannot be achieved. eNMPC is also an interesting approach for combining scheduling and control, which is considered critical in the context of achieving sustainability targets [93]. Several methods exist to reduce or shift the computational demand of NMPC. Fast-update methods, e.g., [101, 209] do not solve the problem to full convergence, and thus reduce the time required for online computation. These methods rely on notions of continuity of the optimal solution and try to track the optimality conditions. A comprehensive review of fast-update methods can be found in [26]. Other authors use model reduction techniques, e.g., based on proper orthogonal decomposition [210], ML [211] or simplifications based on physical insight of the system at hand [47] in order to obtain a tractable problem.
A well-investigated method for reducing the online computational demand of MPC is explicit MPC [25]. It exploits the fact that the solution to the optimization problem for finding the optimal control sequence is parametric in the vector of differential states. Consequently, the parametric problem is solved offline prior to deploying the

controller and the only task during online operation is to determine the correct polytopic region and to apply the corresponding controls. For problems with linear models, quadratic cost functions and constraints, the optimal control policy is known to be piecewise affine. The approach, however, scales unfavorably with the number of states and constraints [212].

Learning the control policy of NMPC with ML methods has been proposed as early as the 1990s [213]. These ideas have been recently revisited [206, 204, 27, 214], typically in a supervised learning context, where the reference data is obtained from solving multiple NMPC problems offline. This is the method we used in the previous Chapter. Lovelett et al. [206] propose to use diffusion maps to find an intrinsic lower dimensional manifold of the mapping from the state space to the control policy space which allows for simplified learning of the control policy. Lucia and Karg [27] learn the control policy of a robust framework [99] with an artificial neural network (ANN) and show on a batch polymerization case study that the resulting ANN does not perform worse than NMPC when the occurring uncertainty is larger than assumed. They further find that deep ANNs exhibit superior performance compared to shallow ANNs with the same total number of neurons. This work was extended in [214] where ANNs are used to approximate the cost function beyond the robust horizon. In another effort, Karg and Lucia [205] show that deep ANNs with rectifier linear unit (ReLU) activation functions can exactly describe the piecewise-affine control policies resulting from linear MPC. Further, they present a feasibility-recovering step for the linear problem. The authors have also applied their methods to mixed integer model predictive control [215]. In [216] it is proposed to learn the control policy of a NMPC algorithm which is robust to input disturbances and the authors provide conditions under which probabilistic stability guarantees for the approximation of the control law can be given. In [203] it is proposed to train the ANN directly on the cost function which resembles ideas from reinforcement learning. In a reinforcement learning (RL) context it has been proposed to use MPC as a function approximator [217] and considerations include constraint satisfaction [218]. Comparison with methods that use MPC for RL is beyond the scope of our manuscript and we refer to [219] for an overview of recent developments.

Note that in addition to approaches where ML is used to approximate the control policy, several MPC approaches where the controller uses a ML model (e.g., [220, 221, 222, 223]) or a hybrid model that contains ML model parts (e.g., [224]) exist. A detailed review is beyond the scope of this manuscript.

While methods which approximate the NMPC control policy relying only on ML with supervised learning mostly eliminate the online computational demand, they have several drawbacks. First, the required amount of data grows with the number of states.

This can be partially mitigated for problems whose closed-loop dynamics can be reduced, so that data can be represented by a low dimensional manifold [206]. Second, constraints can be violated even if the control signal is only interpolated. Finally, no extrapolation beyond the training set range can be guaranteed.
We propose two ML-based MPC methods that address the two latter problems while facilitating fast solution of the NMPC problem. Both methods rely on learning the open-loop control trajectory from offline NMPC simulations with an ANN which is then used to provide an initial guess for a subsequent algorithm. In the first method, we use the initial guess to solve the NMPC optimal control problem (OCP) to full convergence. In the second, we instead solve a single quadratic program (QP) to correct the control trajectories provided by the ANN before applying them to the plant. The first method aims at achieving convergence to the optimal solution of the NMPC problem with reduced solution times by using knowledge from offline simulations. A variety of initialization approaches for NMPC exist that try to exploit typical solution structures. The simplest method, called warm-starting, is to reuse the results from the previous time-step [90]. The so-called shift initialization strategy is motivated by Bellman's principle of optimality and is typically used in shrinking-horizon settings [225]. There, the first time-step is discarded and the problem is initialized with the remaining trajectory. When used in receding horizon settings, the trajectory is appended with a copy of the final time-step. Finally, an initialization strategy based on the insight that many eNMPC problems exhibit turnpike properties has been proposed by Würth [226]. In contrast to available initialization methods, our proposed initialization strategy does not rely on assumptions about the solution structure. Note that somewhat similar ideas have been presented for warm-starting of the integers for hybrid MPC [227] and for finding the correct active set when solving quadratic programs (QP) associated with MPC [228].
The second method aims at improving the objective function and feasibility with little computational effort by correcting the controls calculated by the ANN. We use the control trajectories provided by the ANN and update the control profile approximations by solving a QP with exact first and second order gradients, i.e., based on a mechanistic model. The rationale is to reduce the potential deterioration of control performance due to interpolation of the ANN or extrapolation when disturbances outside the training set range occur. Although the QP is inspired by neighboring extremal updates [101, 102], the method is conceptually different as all calculations are performed after the measurements from the current time-step are available.
To illustrate the performance of the proposed ANN-based methods, we apply them to an established control case study. Here, we choose a polymerization process in a CSTR. For comparison, we use two benchmarks: (i) NMPC with shift-initialization

strategy [225] and (ii) implementing the controls provided by the ANN without further correction, a method also used in literature [206, 205, 204, 27, 214]. The first benchmark represents an upper bound to the achievable control performance. However, it is the method with highest computational cost. The second benchmark can be obtained with small computational effort but the quality of the control signal can be expected to be worse as the method interpolates between training data points or even extrapolates when the current state or disturbance values are outside of the training set range.
An application of these method to the ORC system is not considered in this chapter as the feedback delay of our second method would still be too large for real-time application. We discuss how our methods could be extended, in order to be used for the ORC system, in the conclusion of this chapter.
The remainder of this chapter is structured as follows. We briefly introduce the examined process and the corresponding mathematical model in Chapter 8.2 followed by a description of the benchmark controllers and presentation of our proposed methods in Chapter 8.3. We discuss the data acquisition process in Chapter 8.4. Training results and results of the proposed control schemes for the CSTR reactor are discussed in Chapter 8.5 followed by concluding remarks in Chapter 8.6.

8.2 Styrene polymerization process description and control task

In the case study, we consider styrene polymerization in a CSTR (Fig. 8.1). Styrene monomer is polymerized using azobisisobutyronitrile as initiator which is dissolved in benzene. We select this process as it is commonly used as a control benchmark, e.g., in [229, 230, 231]. Our aim is to illustrate how our proposed methods can achieve significant speed-up of the NMPC solution while maintaining good control performance, although real-time capability of NMPC is not an issue for the examined system. Further description of the process and the full model are provided in Appendix C. Constraints on input and state variables are listed in Tab. C.1.
The degrees of freedom are the monomer flow-rate Q_m, the initiator flow-rate Q_i and the coolant flow-rate Q_c. The solvent flow-rate is fixed. Considered disturbances are the feed temperature T_f and the initiator feed concentration C_{if}. The disturbances are measured but not predicted, i.e., the controller assumes the disturbances to be constant over the control and prediction horizons with the value registered at the beginning. The control objective Φ is to minimize a weighted sum of the deviation from a desired polymer number average molecular weight (polymer grade) P_{NAMW} and the

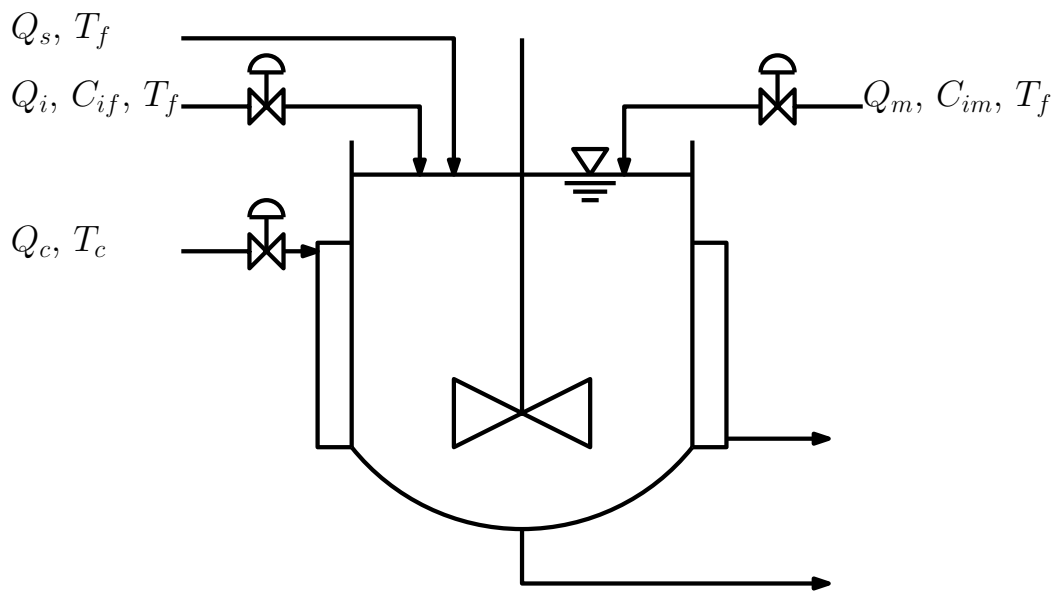

Figure 8.1: Styrene polymerization reactor. Manipulated variables are indicated by the control valves

negative production rate, i.e.,

$$\Phi(t) = \int_{t_0}^{t} w_{NAWM} \left(P_{NAMW}^{des}(t) - P_{NAMW}(t)\right)^2 - w_{Prod} \left(Q_m(t) + Q_i(t)\right) \mathrm{d}t \quad (8.1)$$

where w_{NAWM} and w_{Prod} are weighting factors for the two objectives. The desired grade is known but time-dependent.

8.3 NMPC approaches

We start with a brief description of the NMPC software implementation in Chapter 8.3.1 as it is essential for generating the data. We then present the direct implementation of the ANN signals to the plant, which is our second benchmark, in Chapter 8.3.2 followed by our two proposed methods in Chapter 8.3.3 and Chapter 8.3.4.

8.3.1 NMPC with shift initialization (sNMPC)

In the considered case study, the desired polymer grade trajectory P_{NAMW}^{des} is the time-dependent parameter which is available to the optimizer.

We solve the OCP (8.1), (2.2b)-(2.2f) with direct single-shooting using DyOS [185]. The DAE-integrator is NIXE [199] and the optmizer is SNOPT [89]. The time horizon is divided into N_P time intervals of duration Δt with $t_f = t_0 + N_P \Delta t$. The controls $\boldsymbol{u}(t)$ are discretized as piecewise constant on a grid with N_C points where the last interval has length $(N_P - N_C + 1)\Delta t$ and all other intervals have length Δt. We define $\underline{\mathbf{u}}(t) := \left(\boldsymbol{u}_{t|0}, \boldsymbol{u}_{t|1}, \ldots, \boldsymbol{u}_{t|N_c-1}\right)$ as the open-loop control sequence of the OCP. The notation $\boldsymbol{u}_{t|k}$ indicates that the signal is in the k^{th} interval of the OCP solved at time t. Only the first control signal $\boldsymbol{u}_{t|0}$ is implemented before the horizon is shifted and the problem is re-solved. We use the shift initialization strategy [26] for initializing subsequent OCPs, i.e., $\underline{\mathbf{u}}^{init}(t + \Delta t) := \left(\boldsymbol{u}^*_{t|1}, \boldsymbol{u}^*_{t|2}, \ldots, \boldsymbol{u}^*_{t|N_c-1}, \boldsymbol{u}^*_{t|N_c-1}\right)$ which reuses the optimal solution from the previous instance, indicated by superscript *, shifted by the sampling time Δt and copies the last control signal. In the remainder of this Chapter we only discuss signals at time t and therefore we will refer to $\boldsymbol{u}_{t|k}$ as $\boldsymbol{u}_k$. We neglect plant-model mismatch and the computational delay associated with solving the OCP. Further, we assume full state feedback.

8.3.2 Direct application of ANN signals learned from NMPC (dANN)

In order to reduce the computational demand associated with solving the NMPC problem repeatedly online, our second benchmark consists of solving a large number of instances offline, learning the resulting control policy and deploying the resulting ML model to control the process. As only the first control signal $\boldsymbol{u}_0$ is applied to the plant before the problem is re-solved, it is only necessary to learn the control mapping to this signal, thus simplifying the training problem. The number of variables that the ML model has to approximate (targets) is equal to the number of manipulated variables, i.e., the control horizon does not influence the number of targets. We use an ANN to learn $\boldsymbol{u}_0$ with the inputs reflecting that, in our case, the solution of the NMPC problem is parametric in $\boldsymbol{x}$, $\boldsymbol{p}$ and $\boldsymbol{d}$. This implies that the required data amount does not scale with the number of algebraic variables

$$\hat{\boldsymbol{u}}_0(t) = \boldsymbol{f}^{\mathrm{dANN}}(\boldsymbol{x}(t), \boldsymbol{p}(t), \boldsymbol{d}(t)) \ . \tag{8.2}$$

The training process is depicted in Fig. 8.2a. When the controller is deployed, $\boldsymbol{f}^{\mathrm{dANN}}$ predicts the inputs $\hat{\boldsymbol{u}}_0$ after $\boldsymbol{x}$, $\boldsymbol{p}$ and $\boldsymbol{d}$ are available. The predicted inputs are clipped so that they satisfy the input constraints and then applied to the plant

$$\boldsymbol{u}_0(t) = \max(\boldsymbol{u}_{min}, \min(\hat{\boldsymbol{u}}_0(t), \boldsymbol{u}_{max})) \ . \tag{8.3}$$

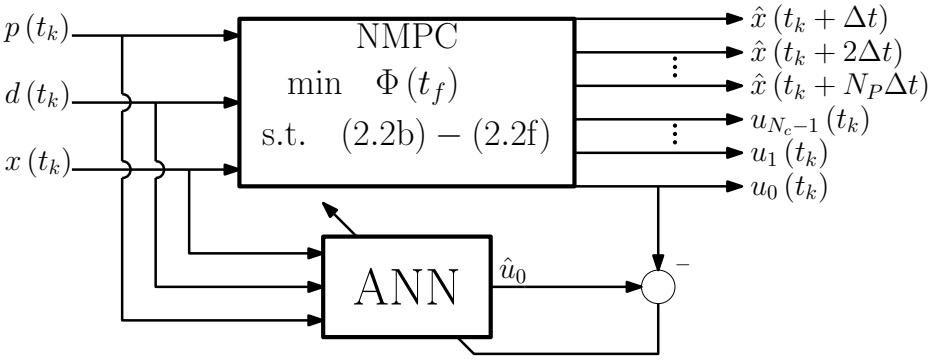

(a) Training process for $\boldsymbol{f}^{\mathrm{dANN}}$. Only $\boldsymbol{u}_0$ is a target.

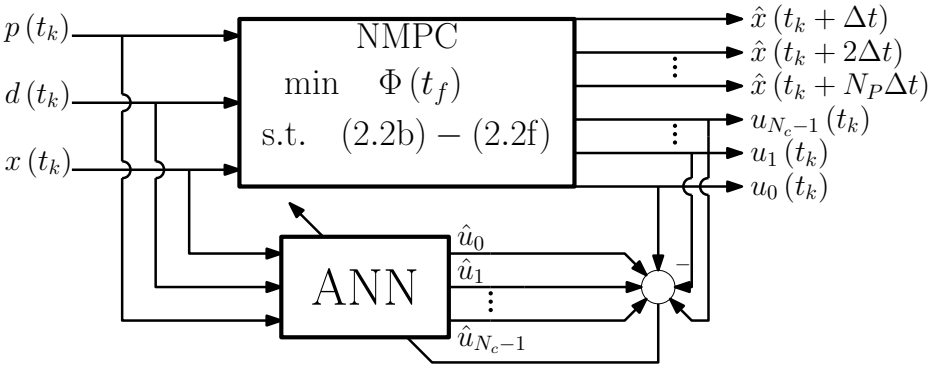

(b) Training process for $\boldsymbol{f}^{\mathrm{iANN}}$. All components of $\underline{\mathbf{u}}$ are targets.

Figure 8.2: Training of $\boldsymbol{f}^{\mathrm{dANN}}$ required for dANN and $\boldsymbol{f}^{\mathrm{iANN}}$ required for iANN and uANN. While for the former method only the first control signal has to be learned, for the two latter methods the complete control trajectory is required.

8.3.3 ANN initialization (iANN)

The solution of the OCP (8.1), (2.2b)-(2.2f) with single-shooting requires an initial guess for the trajectories of the control variables in each instance. The quality of the initial guess influences the number of iterations required for convergence and, thus, the time required for solving the OCP. A poor initial guess might also result in a poor local optimum.

Our first proposal aims at utilizing the observations from offline NMPC simulations to provide an accurate initial guess which fosters fast convergence of the OCP solution. In contrast to the method presented in Chapter 8.3.2, we have to learn the complete open-loop optimal control sequence in order to provide an initial guess

$$\hat{\underline{\mathbf{u}}}(t) = \boldsymbol{f}^{\mathrm{iANN}}(\boldsymbol{x}(t), \boldsymbol{p}(t), \boldsymbol{d}(t)) \ . \tag{8.4}$$

and use the prediction from $\boldsymbol{f}^{\mathrm{iANN}}$ to initialize the OCP. The predictions of the open-loop input trajectory $\underline{\hat{\mathbf{u}}}$ are filtered as in (8.3) in order to satisfy the input constraints. While available initialization strategies [90, 225, 226] rely on some understanding of the problem structure and are suitable only when the underlying assumptions are fulfilled, the ANN initialization strategy promises to be efficient irrespective of problem structure, given that sufficient data to cover the operational domain was available during training. The training process to obtain $\boldsymbol{f}^{\mathrm{iANN}}$ is depicted in Fig. 8.2b. It should be noted that in contrast to $\boldsymbol{f}^{\mathrm{dANN}}$ in (8.2) the number of targets scales also with the control horizon length N_C.

8.3.4 ANN update (uANN)

The strategy presented in the previous section aims at reducing the NMPC solution time by providing a smart initialization. For many problems, however, solving the NMPC problem to full convergence might not be tractable, irrespective of the initialization strategy. In such cases, using dANN would be possible at negligible cost. However, as mentioned before, no safeguards to ensure path or endpoint constraint satisfaction and convergence to local optimality exist. Thus, we propose a method that aims at finding a compromise between reduced computational demand and constraint satisfaction and optimality. Therefore, we use the approximation of the open-loop control trajectory $\boldsymbol{f}^{\mathrm{iANN}}$ (8.4) as the initial guess in each time-step for a suboptimal algorithm that solves a single OP approximation of the NMPC problem. We first approximate $\underline{\hat{\mathbf{u}}}(t)$ using the trained $\boldsymbol{f}^{\mathrm{iANN}}$. We then construct and solve the following quadratic program (QP)

$$\min_{\Delta \boldsymbol{u}} \quad \frac{1}{2} \Delta \boldsymbol{u}^T \boldsymbol{\mathcal{L}}_{\boldsymbol{uu}} \left(\underline{\hat{\mathbf{u}}}, \boldsymbol{\lambda} \right) \Delta \boldsymbol{u} + \boldsymbol{\Phi}_{\boldsymbol{u}}^T \left(\underline{\hat{\mathbf{u}}} \right) \Delta \boldsymbol{u} \tag{8.5a}$$

$$\text{s. t.} \quad \boldsymbol{h} \left(\underline{\hat{\mathbf{u}}} \right) + \boldsymbol{h}_{\boldsymbol{u}} \left(\underline{\hat{\mathbf{u}}} \right) \Delta \boldsymbol{u} \leq \mathbf{0} \tag{8.5b}$$

to improve the control signal provided by the ANN. The solution of the QP satisfies a first-order approximation of the constraints (8.5b), thus facilitating feasibility. We obtain the Hessian $\boldsymbol{\mathcal{L}}_{\boldsymbol{uu}}$ of the Lagrangian

$$\mathcal{L} \left(\underline{\hat{\mathbf{u}}}, \boldsymbol{\lambda} \right) = \Phi \left(\underline{\hat{\mathbf{u}}} \right) - \boldsymbol{\lambda}^T \boldsymbol{h} \left(\underline{\hat{\mathbf{u}}} \right) \tag{8.6}$$

as well as the gradients of the objective and constraints functions with respect to the inputs $\boldsymbol{\Phi}_{\boldsymbol{u}}$ and $\boldsymbol{h}_{\boldsymbol{u}}$ by integrating the DAE with first and second order sensitivities for the predicted $\underline{\hat{\mathbf{u}}}(t)$ using DyOS with composite adjoints [232] and NIXE. We hence require one integration with first and second order sensitivities and one QP solution

instead of a full optimization. To obtain $\mathcal{L}_{\boldsymbol{uu}}$ a guess for the Lagrange multipliers $\boldsymbol{\lambda}$ is required. We obtain this guess through a simple warm start, i.e., we use the Lagrange multiplier from the previous QP solution. For the first iteration we set $\boldsymbol{\lambda} = \mathbf{0}_{N_C \cdot N_{PC} \times 1}$ where N_{PC} is the number of path constraint as no previous solution is available. We also investigated shifting the Lagrange multipliers but found this to perform worse. The employed QP solver requires the problem to be convex, thus, in case $\mathcal{L}_{\boldsymbol{uu}}$ is not positive definite, we iteratively add an increasing value to the diagonal until the Hessian is positive definite so that we obtain a convex QP. In case the QP (8.5a)-(8.5b) is infeasible, we solve a feasibility restoring QP

$$\min_{\Delta \boldsymbol{u}, \xi} \quad \frac{1}{2} \cdot \begin{bmatrix} \Delta \boldsymbol{u}^T & \xi \end{bmatrix} \cdot \begin{bmatrix} \epsilon \boldsymbol{I}_{N_u \cdot N_C} & \mathbf{0}_{N_u \cdot N_C \times 1} \\ \mathbf{0}_{1 \times N_u \cdot N_C} & 1 \end{bmatrix} \cdot \begin{bmatrix} \Delta \boldsymbol{u} \\ \xi \end{bmatrix} \tag{8.7a}$$

$$\text{s. t.} \quad \boldsymbol{h}\left(\underline{\hat{\mathbf{u}}}\right) + \boldsymbol{h}_{\boldsymbol{u}}\left(\underline{\hat{\mathbf{u}}}\right) \Delta \boldsymbol{u} \leq \mathbf{1}_{N_C \cdot N_{PC} \times 1} \cdot \xi \tag{8.7b}$$

which aims at minimizing the maximum constraint violation ξ and bears some resemblance to the QP proposed in [205] for guaranteeing feasibility when approximating the control policy for linear time-invariant systems. Note that small numbers ϵ are placed on the diagonal of the appended matrix in order to maintain a positive definite matrix and, thus, a convex QP. After solving either (8.5a)-(8.5b) or (8.7a)-(8.7b), $\Delta \boldsymbol{u}$ is added to the predicted input

$$\underline{\mathbf{u}} = \underline{\hat{\mathbf{u}}} + \Delta \boldsymbol{u} \tag{8.8}$$

and the first control signal $\boldsymbol{u}_0$ in $\underline{\mathbf{u}}$ is applied to the plant before the time is shifted. The algorithm requires, in addition to evaluating the ANN, one second-order sensitivity integration and one QP solution. A pseudo-code description of the algorithm discussed in this section is provided in Appendix D. The training process is identical to the one for the method presented in Chapter 8.3.3.

It is important to highlight the subtle differences between fast-update methods and uANN. While fast-update methods such as neighboring extremal updates [101, 102] account for changes in disturbances and parameters in the QP, uANN incorporates these in the ANN approximation. As this can only be done after the values have been measured, the second-order sensitivity integration can only be carried out after the measurements are available, whereas it is carried out during the sampling time interval in fast-update methods.

8.4 Data generation

As discussed in Chapter 8.3, our proposed methods rely on learning the control policy of the NMPC controller by means of supervised learning with samples from NMPC

simulations. To generate the data for training, we executed 5000 closed-loop NMPC simulations as explained in Chapter 8.3.1. As general guidelines on the required amount of data are hard to provide, we iteratively increased the number of considered NMPC solutions until we stopped noticing significant improvements in the ability of the trained ANN to approximate the control policy within in the training set range. Generating the data took more than two days on a desktop computer. From trial simulations, we obtained $\Delta t = 5$ h, $N_C = 5$, $N_P = 7$ as tuning parameters that yielded good performance for the NMPC controller. The sampling time is equal to the dynamic real time optimization sampling time used in [231] and shorter than the smallest time constant at the reported steady-state [230]. Each run had a total simulation time of $t_f = 100$ h as in [231], corresponding to 20 samples per NMPC simulation. Consequently, we obtained $\underline{\underline{\mathbf{u}}} \in \mathbb{R}^{100000\times15}$, $\underline{\boldsymbol{u}_0} \in \mathbb{R}^{100000\times3}$, $\underline{\boldsymbol{x}} \in \mathbb{R}^{100000\times6}$, $\underline{\boldsymbol{p}} \in \mathbb{R}^{100000\times5}$ and $\underline{\boldsymbol{d}} \in \mathbb{R}^{100000\times2}$. The additional underlines indicate that the matrices result from concatenating the vectors of all OCP solutions.
For sampling the state-space, we used latin hypercube sampling. To avoid a redundant initial point in the data, we sampled the initial values of the differential states with a deviation of ±10% from the nominal steady-state reported in [229, 230, 231] for the initiator concentration C_i, the monomer concentration C_m, zeroth moments D_0 and first moments D_1. Further, we sampled between the lower and upper bound for the reactor temperature T_r. We did not sample the cooling jacket temperature T_c in order to avoid situations where due to T_c being higher than T_f infeasibilities might be unavoidable. Based on the different disturbances and desired grades described in the following the trajectories then evolve to cover the state space. Each run included one polymer grade transition that occurred at random times. The desired grades were in the range from 52.2 kg/mol to 73.08 kg/mol. Further, two steps in the disturbances initiator feed concentration C_{if} and feed temperature T_f occurred randomly distributed with random step size and the resulting values within ±2% of the nominal values of $T_{f_0} = 330$ K and $C_{if_0} = 0.5888$ mol/l.

8.5 Results

During training of $\boldsymbol{f}^{\mathrm{dANN}}$ and $\boldsymbol{f}^{\mathrm{iANN}}$ we found that deep ANNs achieved better approximation of the control policy than shallow ANNs with validation mean squared errors smaller than 0.003 for both ANNs. Based on the training results, we chose an ANN with four hidden layers for $\boldsymbol{f}^{\mathrm{dANN}}$ and an ANN with three hidden layers for $\boldsymbol{f}^{\mathrm{iANN}}$. Detailed training results are provided in Appendix E.
To assess the performance of the proposed control strategies, we investigate 10 sce-

narios structurally similar to those encountered during training, i.e., two step changes in both disturbances and one step change in the desired polymer grade. To test the robustness of the proposed approaches, we include disturbances outside the training set range. We compare the results of our proposed methods iANN and uANN with the two standard strategies sNMPC and dANN as benchmark. We discuss the results regarding their control performance and closed-loop constraint satisfaction in Chapter 8.5.1 and the required computational times in Chapter 8.5.2. We neglect the computational cost for evaluating ANNs in the remainder of this manuscript as the times were often not measurable with the Python clock which has a precision of 16 milliseconds. This pertains to the introduced feedback delay and analysis regarding the solution time.

8.5.1 Control performance

For the 10 scenarios for assessing controller performance, we allowed the disturbances to be within ±3% around their nominal values, i.e., we increased the bounds of the training set by 50%. The initial values were sampled within the training set range. An overview of the closed-loop objective function and the maximum reactor temperature constraint violation $T_{vio,max}$ is presented in Tab. 8.1 for all 10 runs

$$T_{vio,max} = \max\left(\max\left(0, T_r\left(t\right) - 325\ \mathrm{K}, 315\ \mathrm{K} - T_r\left(t\right)\right)\right) . \tag{8.9}$$

sNMPC and iANN both achieve closed-loop constraint satisfaction in all ten runs. For most runs they reach the same objective function value and the control signals coincide. However, small differences in objective function value exist in some cases. This can be explained by multimodality of the problem. For the two instances where different objective functions are reached, using sNMPC provides a slightly better objective. However, during further trials not presented here, we did not find any pattern indicating that either initialization method generally achieves consistently superior results. Directly applying the control signals provided by the ANN (dANN) results in closed-loop infeasibility for many runs. Moreover, the obtained objective function value is often much worse than those obtained by sNMPC and iANN. Apparently, the ANN is not able to provide sufficiently accurate prediction of the control inputs. In the instances where the differences in objective value between dANN and sNMPC/iANN are large and constraint violations occur using dANN, the disturbances are typically outside the training set range. Hence, no improvement by providing a more densely sampled training set or by using a larger ANN can be guaranteed. Applying a QP update to the ANN prediction (uANN) yields controls that are closed-loop feasible

Table 8.1: Closed-loop objective values and constraint satisfaction for all ten runs.

Run	sNMPC		dANN		iANN		uANN	
	Φ [−]	$T_{vio,max}$ [K]	Φ [−]	$T_{vio,max}$ [K]	Φ [−]	$T_{vio,max}$ [K]	Φ [−]	$T_{vio,max}$ [K]
1	-2.34	0.00	3.28	1.02	-2.34	0.00	-1.09	0.00
2	-0.10	0.00	0.52	0.00	-0.10	0.00	-0.04	0.00
3	-6.20	0.00	-3.13	0.42	-6.20	0.00	-6.14	0.00
4	-0.75	0.00	1.79	0.14	-0.74	0.00	-0.74	0.00
5	-5.18	0.00	-2.59	0.16	-5.18	0.00	-4.21	0.00
6	-6.26	0.00	-5.04	0.65	-6.26	0.00	-6.13	0.00
7	-4.36	0.00	60.03	2.04	-4.36	0.00	-3.86	0.07
8	3.03	0.00	4.57	0.05	3.03	0.00	3.09	0.00
9	60.96	0.00	72.70	0.11	61.04	0.00	61.21	0.00
10	-5.03	0.00	30.03	0.46	-5.03	0.00	-4.74	0.00

except for one run. In the run that exhibits closed-loops infeasibilitiy, it is orders of magnitudes smaller than obtained with dANN and practically negligible. Further, the obtained objective function value is better than the value obtained with dANN in all runs and typically very close to the value obtained with sNMPC and iANN.
We discuss in the following one of the runs in more detail. We focus on run 7 where dANN exhibits the largest constraint violation. This is to showcase the risks associated with using the ANN predictions without further correction and to highlight that uANN can provide a significant improvement at little additional cost. Additional figures on all other runs are provided in the supplementary material of [7]. The feed temperature and initiator feed concentration disturbance for run 7 are depicted in Fig. 8.3. The feed temperature exhibits values both higher and lower than the training set limits and the initiator feed concentration exceeds the training set limit from $t = 65$ h on.
The control inputs calculated by the controllers sNMPC, dANN, iANN and uANN are depicted in Figs. 8.4a-8.4c and the resulting polymer grades, reactor temperatures and objective function values are depicted in Figs. 8.4d-8.4f. NMPC with shift initialization strategy (sNMPC), which provides the best achievable control policy, precisely tracks the desired polymer grade (Fig. 8.4d) and no constraint violations occur (Fig. 8.4e). It should be noted that the path constraints are only evaluated on the control grid points, i.e., with a resolution of 5 h and therefore can be visibly violated at time points not considered on the grid without being infeasible. For visualization,

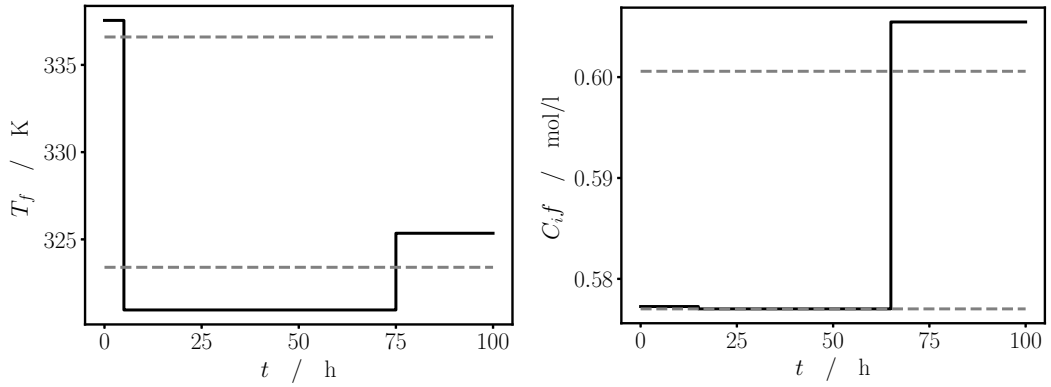

(a) Feed temperature

(b) Initiator feed concentration

Figure 8.3: Disturbance signals for run 7. The training set bounds of the disturbances are indicated by the dashed gray lines.

grid points are indicated by the green crosses on the dANN trajectory. Methods to guarantee path constraint satisfaction at all times exist (e.g., [87]) but are not considered here. Using the predictions from $\boldsymbol{f}^{\mathrm{dANN}}$ directly results in deterioration of the control performance. Especially during those periods where the feed temperature disturbance is outside the training set range, dANN is not able to track the desired polymer grade. The reactor temperature violates the upper bound at $t = 5$ h and the lower bound later on. The polymer grade initially overshoots the desired set-point and then exhibits a permanent offset. After the second step in the feed temperature disturbance at $t = 75$ h, where it is within the training set range, the control performance improves. Using $\boldsymbol{f}^{\mathrm{iANN}}$ to initialize the NMPC problem (iANN) yields identical control signals as sNMPC for this run. Note that in those runs where the control signals occasionally differ, these differences do not result in vastly different P_{NAMW} trajectories. Using the uANN approach, we observe a large improvement compared to dANN. Especially during the period from $t = 20$ h to $t = 75$ h the controller is able to maintain a polymer grade close to the set-point. Further, the constraint violation is small. In conclusion, uANN appears to offer a good compromise between computational rigor and computational demand which we will assess next.

8.5.2 Solution times

As already mentioned, the ANN can be evaluated at negligible computational cost. Further, the solution time of (8.5a)-(8.5b) was too short to be reliably measured with the Python clock on Windows. Thus, we do not present statistics for dANN and

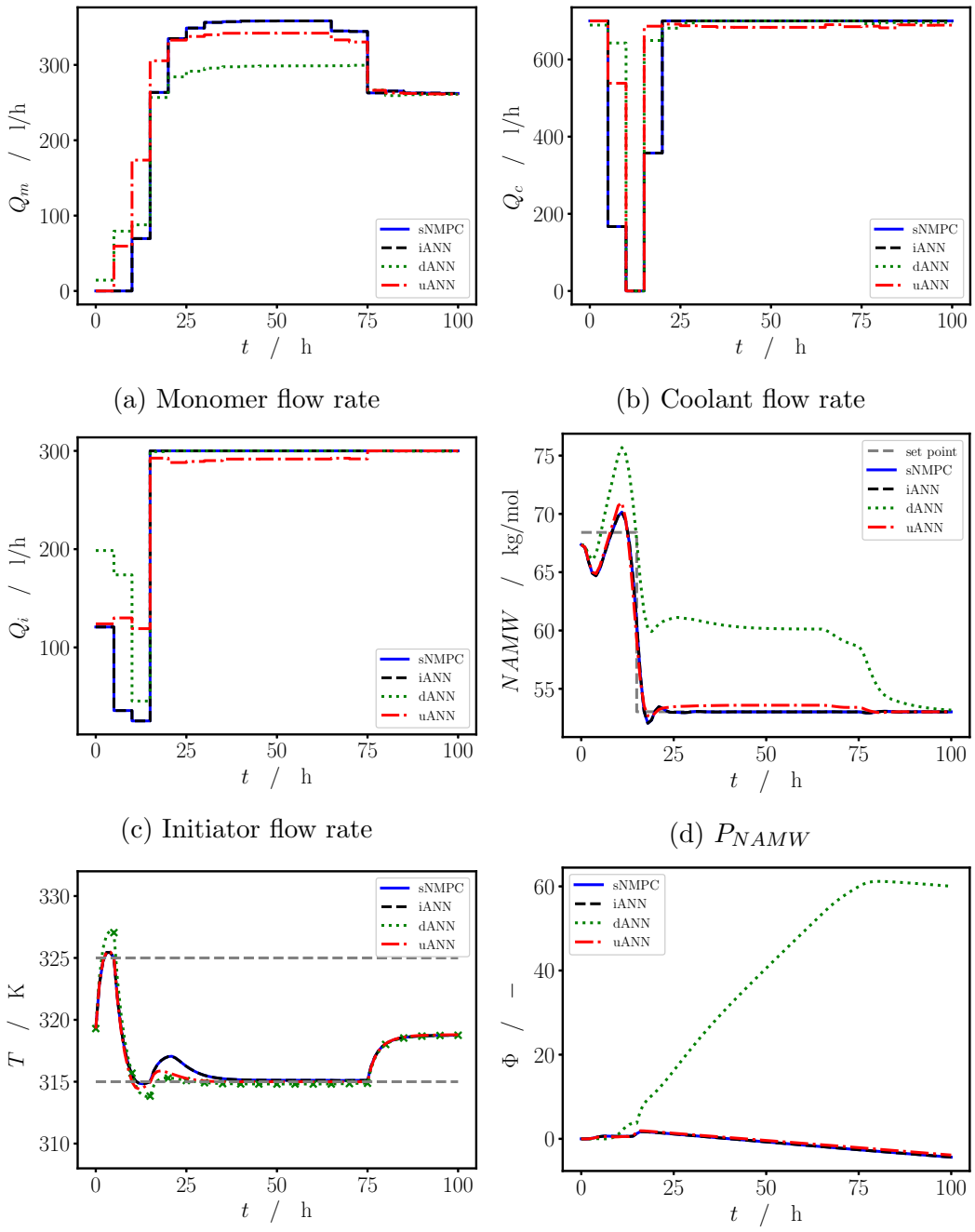

(a) Monomer flow rate

(b) Coolant flow rate

(c) Initiator flow rate

(d) P_{NAMW}

(e) Reactor temperature

(f) Objective function

Figure 8.4: Controls and results from run 7

only account for the computational demand of the NMPC solution of iANN and the demand for the second-order sensitivity integration for uANN.

An overview of solution times is presented in Tab. 8.2. sNMPC has lower average

Table 8.2: Time for solving the respective problems. The shortest and longest solution time over all runs are printed in bold face for each method. The time required to evaluate the ANNs is neglected.

Run	sNMPC (s)			iANN (s)			uANN Integration (s)		
	min.	max.	avg.	min.	max.	avg	min.	max.	avg
1	0.56	4.08	1.58	1.42	3.47	2.20	0.05	0.08	0.06
2	0.41	3.78	1.11	1.47	3.23	2.18	**0.03**	**0.11**	0.06
3	0.42	4.08	1.37	1.22	3.45	1.95	**0.03**	0.08	0.05
4	**0.08**	3.66	0.99	**0.41**	3.05	1.95	**0.03**	0.08	0.05
5	0.47	4.22	1.82	0.47	**3.72**	2.15	**0.03**	0.09	0.06
6	0.37	4.64	1.21	0.98	2.64	1.57	**0.03**	0.09	0.05
7	0.41	**6.44**	1.10	1.09	3.64	1.96	**0.03**	0.09	0.06
8	0.64	4.28	1.76	1.30	3.67	1.91	**0.03**	0.09	0.06
9	0.42	4.61	1.47	0.42	3.59	2.27	**0.03**	0.09	0.05
10	0.44	3.94	1.28	1.03	2.50	1.77	**0.03**	0.08	0.06

solution times than iANN for all runs and lower minimum solution times for all runs except two where the times are equal. However, for all runs, iANN exhibits lower maximum times. When deploying an NMPC algorithm, reasonable slack to the expected maximum run time must exist. From this perspective, using iANN might hold an advantage. The solution times for uANN are an order of magnitude smaller than those of sNMPC and iANN.

Fig. 8.5 provides boxplots of all runs for sNMPC and iANN for further analysis. Each boxplot contains the solution times for the 20 OCP instances of the respective problem. It is evident that while sNMPC generally behaves better, i.e. the median solution times are lower, iANN exhibits fewer outliers. Closer inspections of the NMPC outliers reveals that these either occur when the disturbance changes or in the first iteration when no shifted solution is available. The observation that the solution times increase when the disturbances changes is in agreement with intuition as the assumptions that motivate the shift initialization strategy are not valid in those situations. More frequent changes in the disturbances than the two steps occuring in our case study would emphasize the strengths of the ANN initialization strategy (iANN). This notion is supported by additional results, provided in the supplementary information, where the disturbances change at every sample.

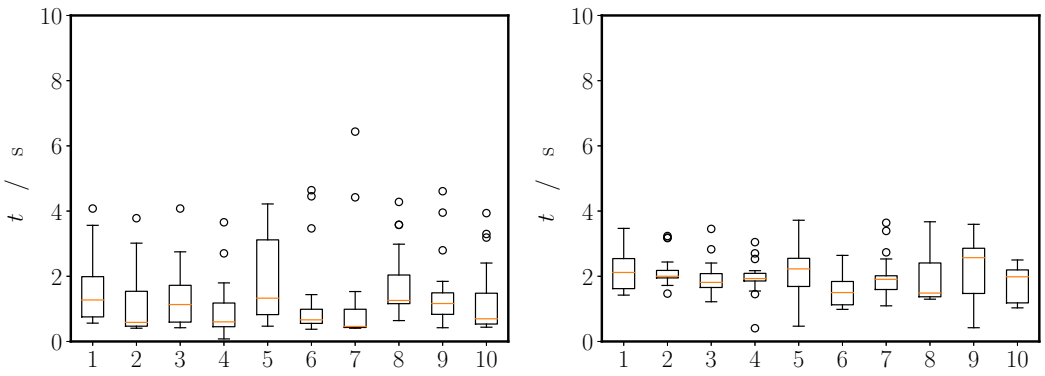

(a) sNMPC (b) iANN

Figure 8.5: Solution times for all ten runs.

8.6 Conclusion

We proposed two ML-based methods based on learning the open-loop control trajectory with an ANN to reduce the computational demand associated with NMPC. Both methods use the control policy predicted by the ANN for initializing an algorithm. First, we proposed to use the initial guess from the ANN prediction to solve the NMPC problem to convergence (iANN). Second, we proposed to solve a single QP based on the initial guess (uANN) to obtain a compromise between the optimal control policy and reduced computational demand.
We applied our proposed methods to a polymerization case study. We benchmarked against two well-known approaches, i.e., NMPC with shift-initialization (sNMPC) and the use of the ANN predictions without further correction (dANN).
After training, we applied our two proposed controllers and the two benchmark controllers to ten additional NMPC runs which included disturbances outside the training set. Using the ANN to initialize the NMPC (iANN) problem mostly results in identical control action and state trajectories as using the shift-initialization strategy (sNMPC), albeit, small differences occasionally exist. Using the ANN prediction directly (dANN) to control the process resulted in a deterioration of the control performance with respect to the objective function value for all runs and with respect to closed-loop feasibility in some runs. This result is unsurprising, especially outside the training set and is a drawback of any method that solely relies on ML. Using the ANN predictions and solving a single QP (uANN) always resulted in superior objective function values compared to (dANN) and negligible constraint violations.
While minimum runtime was lower with shift-initialization (sNMPC), iANN exhibited

tighter distribution of runtimes and shorter worst-case runtime for most cases. Thus, application of iANN is more consistent and predictable which is an advantage for application in the field. For uANN, the computational time required for the second-order sensitivity integration was typically an order of magnitude smaller than the time required for solving sNMPC or iANN. An overview of our findings is provided in Tab. 8.3.

Table 8.3: Overview of the capabilities and limitations of the examined methods. Very good performance is indicated by ++, good performance is indicated by +, average performance is indicated by o and poor performance is indicated by -.

	objective value	computational demand		constraint satisfaction
		offline	online	
sNMPC	++	++	-	++
iANN	++	++	o/-	++
uANN	+	-	+	+
dANN	-	-	++	-

An important aspect is analysis of the data demand with respect to the system size. With an increasing dimension of the state-space, the number of required samples grows, which could make the data acquisition intractable. This issue pertains to all methods that use ML for learning the optimal control policy and has been scarcely covered in literature. Consequently, the methods proposed herein should be applied to a larger example to explore the limits of the approach. Ideally, such a case study should allow for simple scaling of the problem size, e.g., by adding trays in a rectification column. As mentioned by Lovelett et al. [206], many typical large scale chemical engineering unit operations, e.g., heat exchangers or rectification columns, may include redundant information in the state space which can be exploited by learning the optimal control policy in a latent space. Furthermore, a case study where the time required for the second-order sensitivity integration of uANN is too long to achieve real-time capability could be considered in future work. There, uANN could be used in an advanced-step setting [233]. This could also be applied to the ORC system. In [12], we observed that the fast-update method used to control the ORC system required a full prediction of the exhaust gas conditions on the considered horizon. Here, an initialization of the fast-update algorithm with the learned control policy could remedy this issue.

Chapter 9

Conclusions & outlook

In this thesis, we have examined the optimal operation and control of an ORC for WHR. Furthermore, we have examined approximate NMPC through machine learning, a topic that has received significant attention recently. For our contribution to optimal operation of an ORC for WHR, we followed a model-based approach. We covered model development and comparison, design of optimal operating policies through dynamic optimization and comparison of various control strategies. Regarding the use of ML in NMPC, we first applied a published method to our ORC example. In a second step, we proposed two novel methods that tackle shortcomings of established methods.

We started with model development for the considered ORC system in Chapter 3. There, we introduced a model for the cycle that consists of submodels for every major unit operation connected by pipe models. As the dominant dynamics are associated with the thermal inertia of the heat exchanger, we chose a dynamic model for the evaporator and condenser and steady-state models for the pump and turbine. More specifically, we used the MB approach for modeling the heat exchangers. Since the heat exchanger is discretized into zones according to the WF aggregate state, no discrete events occur and the model is twice continuously differentiable, thus suitable for gradient-based optimization techniques. Accordingly, we directly implemented a Helmholtz free energy equation of state for the thermodynamic WF properties instead of relying on a database. We employed dynamic optimization for parameter estimation, using flexible custom heat transfer correlations. We found that the model showed small prediction errors for all quantities and found that it also performed well on additional validation data.

The model developed in Chapter 3 requires all three phases of the WF to be present in the heat exchangers. Thus, situations like start-up, shutdown and temporary loss

of superheat cannot be simulated. In Chapter 4, we examined extensions to the model that allow for consideration of these scenarios. Therefore, we extended the MB model by adding adequate equations for modes of operation where not all phases are present. However, we restricted ourselves to scenarios that can be expected during operation of power cycles. As the model switches between different operation modes with if/else clauses, the extended model cannot directly be used for gradient-based dynamic optimization. For comparison, we implemented a heat exchanger based on the FV approach. For model comparison, we focused on the start-up situation. There we found that the MB model can exhibit unphysical behavior due to the enthalpy averaging assumption. Through simplifying assumptions, we arrived at a linear model and showed that the system exhibits a positive zero which is associated with an inverse response. We proposed two remedies that eliminate this behavior and preserve the low computational cost of the MB model in nominal operation, i.e., when all three phases are present.
In Chapter 5, we examined optimal operating policies for the ORC system. Therefore, we considered two relevant scenarios for the operation in street traffic. First, we used data reflective of a real-world driving cycle that was recorded on a test rig and used in Chapter 3 for parameter estimation. Second, we considered the case where the produced power that can be utilized is temporarily limited. This scenario can occur when the engine torque is below a certain threshold, e.g., when the vehicle is going downhill. Here, we assumed constant heat source conditions. To identify the optimal operating policies, we used dynamic optimization, employing the open-source solver DyOS. Steady-state operation of power cycles is typically most efficient at minimal superheat. Thus, to examine whether this also holds under transient conditions, we compared a minimal superheat strategy to a flexible superheat strategy that maximizes produced power. In the first scenario, we found that the flexible superheat strategy often operates at minimal superheat, however, exhibits some significant peaks in superheat. However, the differences in produced power compared to minimal superheat are small. More relevant are the differences for the second examined scenario. Here, the flexible superheat strategy allows for temporal storage of thermal energy in the heat exchanger walls during the power limitation.
In Chapter 6, we examined control strategies for the ORC system. Our findings from Chapter 5 provided the necessary insight into optimal system operation to develop the proposed strategies. We developed two NMPC strategies and one strategy that uses a PI controller with feedforward term. We showed that the MIMO control problem can be reduced to a SISO superheat tracking control problem and a decoupled real-time turbine optimization for the considered system. Thus, we compared an economic NMPC that manipulates both degrees of freedom to a superheat tracking NMPC,

where the turbine rotational speed is determined by the real-time optimization. Similarly, the PI controller with feedforward term only manipulates the WF mass flow to achieve minimal superheat. We found that splitting the control problem is possible without substantial losses in economic performance. Furthermore we found that the PI controller with feedforward performed almost as good as the much more sophisticated NMPC controllers.
Although we achieved good performance with a PI controller for our considered system, for more complex ORC architectures, NMPC might be required. Generally, the application of NMPC in the automotive industry is often prevented due to the limited computational resources available. Thus, we use our ORC system as a simple example to examine a method to reduce the online computational demand of NMPC. The NMPC controllers we developed in Chapter 6 are far from real-time capable. As a remedy, learning the optimal control policy from simulation data is a promising approach for challenging problems with short sampling intervals and limited computational power. Instead of the optimization-based controller, a machine learning model is used in the online application which is able to provide feedback in negligible time. In Chapter 7, we applied this approach to an ORC system for waste heat recovery. Therein, we restricted ourselves to the regulatory control problem. We carried out 200 NMPC simulations where the controller stabilized the system at a fixed superheat setpoint. With the accumulated data, we trained an ANN that was used to replace the controller in validation tests. Here, we used disturbance values that exceeded the training set bounds. Still, the ANN-based controller was able to stabilize the system. Although this is a promising result, the employed method generally suffers from the fact that no guarantees for constraint satisfaction exist.
This motivated the work presented in Chapter 8. There, we examined methods that use the learned optimal control policy for initialization of a control algorithm. In particular, we proposed two novel methods. The first method (iANN) uses the control policy predicted by an ANN to initialize the NMPC problem which is then solved to convergence. The idea here is that the ANN might be able to provide an initial guess closer to the optimal solution than established methods, such as shifting the solution from the previous time-step. We expected this method to work best in case the disturbances change strongly between subsequent instances of the control problem. Second, we proposed a method that implements the controls after correcting the inital guess with a single QP iteration (uANN). This methods aim at improving the ANN prediction at little computational cost and satisfies a first-order approximation of the constraints. To illustrate our methods, we used a control benchmark instead of our ORC process. In particular, we applied our method to a CSTR case study for the production of polystyrene. In our simulation case study, we found that iANN has an

advantageous distribution of solution times, i.e., the distribution is more narrow and maximum runtimes are smaller, than NMPC with shift initialization. Furthermore, uANN significantly improves the control policy compared to the prediction of the ANN with respect to objective function value and constraint satisfaction, while providing the solution an order of magnitude faster than NMPC. Thus, our two proposed methods succeed in their aims to accelerate the solution of nonlinear model predictive control problems.

Many interesting avenues for future research can be outlined.
As discussed, neither the MB approach nor the FV approach are suitable for gradient-based optimization when phases appear or disappear in a heat exchanger. This is due to (i) discrete events that occur when a phase appears or disappears in the extended MB model and (ii) discrete events when a cell switches from one aggregate state to another in the FV approach. To mitigate this behavior, adequate smoothing is necessary so that the models are twice continuously differentiable. Recently, researchers from our lab proposed to formulate similar problems with smoothed nonlinear complementarity problem functions and showed that the resulting problems can be solved with standard solvers in single shooting [234]. We attempted to apply the proposed methodology to the FV approach in the master thesis of Ashutosh Manchanda [14]. It should be noted that besides replacing the if/else clauses for switching, also the heat transfer correlations and the WF thermodynamics must be smoothed. The resulting model has a large number of complementarities and adequate choice of smoothing parameters is cumbersome. Dynamic optimization was possible, however, convergence was slow and the results were very sensitive to good initial guesses. Future work should therefore focus on improving the problem formulation. Another possibility is to use the non-smooth modeling and optimization framework developed by the Barton group, see [235] and references therein. Preliminary studies indicate that the modeling approach is applicable to the FV model. However, neither of the mentioned approaches has been applied to the MB approach and from intuition, it appears to be more complex to find a smoothed formulation compared to the FV approach.
An adequate smoothed model, however, is key to examine further scenarios for optimal operating strategies. Although relevant scenarios with nominal operation are conceivable, a model covering non-nominal operation is necessary for many interesting scenarios, e.g., start-up or temporal loss of superheat. We believe that assessing optimal operation through dynamic optimization provides valuable insight for control strategy design. Thus, many more scenarios should be assessed in order to build a comprehensive energy management system. Moreover, the peaks in superheat observed in Chapter 5 warrant further investigation.

Although we found no great improvement for the NMPC controllers over a PI controller with feedforward term in Chapter 6, further efforts towards real-time capability of NMPC for the ORC system are indicated. As discussed, more complex ORC architectures have been proposed which are harder to control. To this end, fast-update methods [26] should be examined. We implemented such a method in the master thesis of Jan Schulze [12]. We found that neighboring extremal updates were not real-time capable and a further step to reduce the computational demand would be to approximate the Hessian instead of computing it exactly. Furthermore, the fast-update method required full prediction of the exhaust gas conditions. Otherwise, the unexpected changes in the exhaust gas conditions could not be compensated. Here, using the methods discussed in Chapter 8 promises to alleviate this problem.
Our findings from Chapter 7 indicate that NMPC controllers for the ORC system can be replaced by ANN-based controllers. Although our results are promising, the case study is merely a proof-of-concept and the method should be applied to more challenging scenarios.
The methods proposed to accelerate NMPC through machine learning in Chapter 8 offer many options for extension. Although uANN drastically reduces computational demand, the bulk of the time consumed by the method arises through the sensitivity integration in the feedback phase, i.e., after a measurement has been recorded. For systems with very short sampling intervals, the associated delay might be too long and reduce the quality of the control significantly or even render it completely worthless in case hard real-time constraints apply. For these situations, it is desirable to shift the sensitivity integration into the preparation phase. Essentially, this would mean that we would have to use the ANN prediction to initialize a fast-update strategy, e.g., neighboring extremal updates [101, 102]. An attempt at this can be found in the master thesis of Aron Zingler [15]. The findings there indicate that using an ANN as initialization can result in a control performance with similar performance to the optimal initialization strategy (or advanced step [134]) with a computational cost similar to the shift-initialization strategy. The thesis further examines the option to regularize the training of the ANN by including the sensitivities of the optimal control policy with respect to the parameters of the discretized dynamic optimization problem (2.4a)-(2.4c) in the loss function. Furthermore, a variety of efficient sampling algorithms is examined. As outlined in Chapter 8, the main limitation of methods that learn the optimal control policy from data is the curse of dimensionality as the optimal control policy is a function of the initial state. Thus, the methods are not readily applicable to large-scale problems and methods to alleviate this limitation should be a major focus of future work. For many typical chemical engineering processes, e.g., distillation columns, it is conceivable that a latent space of smaller dimensionality

than the differential state vector can be found. There, learning the optimal control policy in a latent space is a promising idea [206].

Appendix A

Pipe model parameter estimation and parameters for HX models

The parameter estimation for the pipe models is carried out with data from the temperature sensors depicted in Fig. 3.4. We use the data collected from the sensor before the respective pipe segments as the input to (3.22) and (3.23), while the data from the sensor behind the respective element is the desired output. For all segments, measurements from a number of experiments are taken into account. Fig. A.1 shows trajectories for one of the experiments using the obtained parameters for the pipe segment between evaporator and turbine, with the WF outlet temperature of the evaporator as a model input. It can be seen that the model is able to sufficiently capture the dynamics of the temperature at the turbine inlet. For all other pipe segments, results of similar quality are achieved by the parameter estimation.

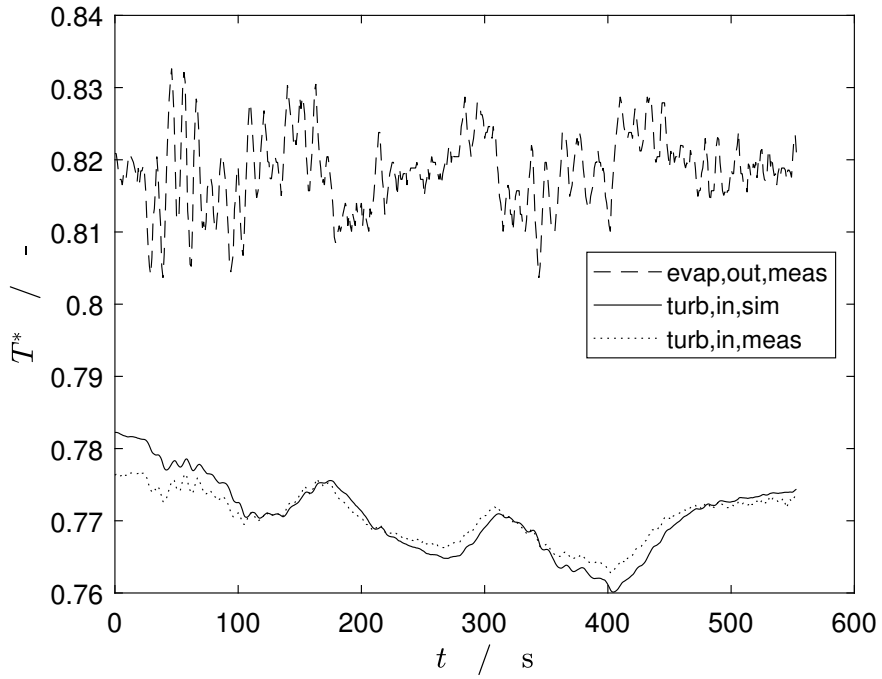

Figure A.1: Result of pipe model between evaporator outlet and turbine inlet, showing the measured temperatures of the evaporator outlet and turbine inlet together with the simulated turbine inlet temperature.

Table A.1: Overview of all estimated parameters for the pipe and turbine models, including bounds and final values. Missing bounds indicate fixed values.

parameter	lower bound	upper bound	final value
$(\alpha \cdot A)_{evap,turb}$ [W/ K]	$1 \cdot 10^{-4}$	100	9.24782
$(\alpha \cdot A)_{cond,pump}$ [W/ K]	$1 \cdot 10^{-4}$	100	17.061
$(\alpha \cdot A)_{pump,evap}$ [W/ K]	$1 \cdot 10^{-4}$	100	15.4042
$(\alpha \cdot A)_{turb,cond}$ [W/ K]	$1 \cdot 10^{-4}$	100	1.64795
$\tau_{evap,turb}$ [s]	0.001	150	56.6023
$\tau_{cond,pump}$ [s]	0.001	150	14.8807
$\tau_{pump,evap}$ [s]	0.001	150	150
$\tau_{turb,cond}$ [s]	0.001	150	0.188313
T_{amb} [K]			300

Table A.2: Overview of all estimated parameters for the evaporator model, including bounds and final values.

parameter	lower bound	upper bound	final value
$\alpha_{liq,0}$ [W/ (m^2 K)]	0	1000	427.287
$c_{liq,1}$ [−]	0	1	0
$c_{liq,2}$ [−]	1	10	3.67548
d_{liq} [W/ (m^2 K)]	-1000	1000	-2.3888
b_{liq} [−]	0.01	10	0.01
u_{liq} [kg/s]	$1 \cdot 10^{-4}$	0.0499	0.005803
$\alpha_{trans,0}$ [W/ (m^2 K)]	0	$1 \cdot 10^{5}$	278.844
$c_{trans,1}$ [−]	0	1	0.458011
$c_{trans,2}$ [−]	1	10	8.83129
d_{trans} [W/ (m^2 K)]	-1000	$1 \cdot 10^{4}$	158.358
b_{trans} [−]	0.01	10	0.088959
u_{trans} [kg/s]	$1 \cdot 10^{-4}$	0.0499	0.02759
$\alpha_{vap,0}$ [W/ (m^2 K)]	0	1000	57.6655
$c_{vap,1}$ [−]	0	1	0
$c_{vap,2}$ [−]	1	10	2.46687
d_{vap} [W/ (m^2 K)]	-1000	1000	17.2663
b_{vap} [−]	0.01	10	0.062251
u_{vap} [kg/s]	$1 \cdot 10^{-4}$	0.0499	0.01665
$\alpha_{exh,0}$ [W/ (m^2 K)]	0	1000	153.173
$c_{exh,1}$ [−]	0	10	0.976345
$c_{exh,2}$ [−]	0	10	1.21767
d_{exh} [W/ (m^2 K)]	-1000	1000	-1.09746
$\dot{m}_{WF,0}$ [kg/s]	0.05	0.05	0.05
$\dot{m}_{exh,0}$ [kg/s]	0.4	0.4	0.4
$T_{exh,0}$ [K]	923	923	923
α_{amb} [W/ (m^2 K)]	0	300	*

*depending on experiment conditions

Table A.3: Overview of all estimated parameters for the condenser model, including bounds and final values.

parameter	lower bound	upper bound	final value
$\alpha_{liq,0}$ [W/ (m^2 K)]	0	$1 \cdot 10^4$	93.7257
$c_{liq,1}$ [−]	0	10	2.55708
$c_{liq,2}$ [−]	0	10	2.86173
d_{liq} [W/ (m^2 K)]	0	1000	6.69519
$\alpha_{trans,0}$ [W/ (m^2 K)]	0	$1 \cdot 10^6$	36411.7
$c_{trans,1}$ [−]	0	10	5.0614
$c_{trans,2}$ [−]	0	10	6.02665
d_{trans} [W/ (m^2 K)]	$-1 \cdot 10^4$	$1 \cdot 10^5$	16491.6
$\alpha_{vap,0}$ [W/ (m^2 K)]	0	300	86.1252
$c_{vap,1}$ [−]	0	10	1.37435
$c_{vap,2}$ [−]	0	10	0.963504
d_{vap} [W/ (m^2 K)]	0	$1 \cdot 10^4$	1862.48
$\alpha_{CW,0}$ [W/ (m^2 K)]	100	5000	2722.54
d_{CW} [W/ (m^2 K)]	$1 \cdot 10^{-5}$	350	108.122
c_{CW} [−]	0	10	0.503491
h_{plate} [m]	$1 \cdot 10^{-5}$	$5 \cdot 10^{-4}$	$3.74 \cdot 10^{-4}$
h_{WF} [m]	$1 \cdot 10^{-5}$	$3 \cdot 10^{-4}$	$1.85 \cdot 10^{-4}$
b_{plate} [m]	0.2	0.4	0.283959
N_{plates} [−]	100	200	141.98
l_{tot} [m]	0.2	0.5	0.343441
$\dot{m}_{WF,0}$ [kg/s]	0.05	0.05	0.05
$T_{WF,0}$ [K]	503	503	503
$\dot{m}_{CW,0}$ [kg/s]	2	2	2

Appendix B

Finite volume heat exchanger model equations

The coupled partial differential equations representing mass (B.1) and energy balance (B.2) are

$$A \cdot \frac{\partial \rho}{\partial t} + \frac{\partial \dot{m}}{\partial z} = 0\,, \tag{B.1}$$

$$A \cdot \frac{\partial \rho h}{\partial t} + \frac{\partial \dot{m} h}{\partial z} = \dot{q}_z \tag{B.2}$$

$$\frac{\partial \rho}{\partial t} = \left(\frac{\partial \rho}{\partial p}\right)_h \frac{\partial p}{\partial t} + \left(\frac{\partial \rho}{\partial h}\right)_p \frac{\partial h}{\partial t}. \tag{B.3}$$

Besides partial derivatives of the density in the single-phase regions, the FV approach also requires partial derivatives in the two-phase region, which are obtained from [142]. The second order derivatives required for the smooth-density method [155] are approximated via finite differences. For the discretization, a first order upwind scheme is applied for all thermodynamic quantities ζ_i (B.4). It has to be noted that flow reversal is not considered in here.

$$\hat{\zeta}_i = \zeta_{i+1/2} = \zeta_i \quad \text{for} \quad \zeta \in \{h, \rho, T, ...\}. \tag{B.4}$$

A grid with a uniform control volume length Δz is using the cross sectional area A according to (B.5):

$$\Delta z = \frac{V}{NV \cdot A} = const. \tag{B.5}$$

where NV is the number of volumes chosen for discretization. The resulting partial differential equations (PDEs) can be reformulated to a set of ordinary differential equations (ODEs) (B.6) and (B.7), equivalent to a 1-D PDE discretization, using backward differences:

$$\left[\left(\frac{\partial \rho_i}{\partial p}\right)_h \frac{dp}{dt} + \left(\frac{\partial \rho_i}{\partial h}\right)_p \frac{dh_i}{dt}\right] A\Delta z + \dot{m}_i - \dot{m}_{i-1} = 0 \quad \text{for} \quad i = 2, \ldots, NV \tag{B.6}$$

$$A\Delta z \left(h_i \frac{\partial \rho_i}{\partial p} - 1\right) \frac{\mathrm{d}p}{\mathrm{d}t} + A\Delta z \left(h_i \frac{\partial \rho_i}{\partial h} + \rho_i\right) \frac{\mathrm{d}h_i}{\mathrm{d}t} = m_{i-1}h_{i-1} - m_i h_i + q_{r,i} A\Delta z \tag{B.7}$$

Appendix C

Polystyrene CSTR model description

We consider a CSTR for the production of polystyrene by polymerization. The model was initially presented in [229] and augmented in [230] to allow for the calculation of number average molecular weight. We make use of the scaling recommendations in [236]. All constrains on inputs and state variables are listed in Tab. C.1.

		LB	UB
Q_m	l/h	0	400
Q_c	l/h	0	700
Q_i	l/h	0	300
T	K	315	325

Table C.1: Lower and upper bounds for inputs and constrained variables.

Model equations The unscaled model equations are

$$\frac{\mathrm{d}C_i}{\mathrm{d}t} = \frac{Q_i \cdot C_{if} - Q_t \cdot C_i}{V} - k_d \cdot C_i$$
$$\frac{\mathrm{d}C_m}{\mathrm{d}t} = \frac{Q_m \cdot C_{im} - Q_t \cdot C_m}{V} - k_p \cdot C_m \cdot C_{gp}$$
$$\frac{\mathrm{d}T}{\mathrm{d}t} = \frac{Q_t \cdot (T_f - T)}{V} - \frac{\Delta H_r}{\rho \cdot c_p} \cdot k_p \cdot C_m \cdot C_{gp} - \frac{U \cdot A}{\rho \cdot c_p \cdot V} \cdot (T - T_c)$$
$$\frac{\mathrm{d}T_c}{\mathrm{d}t} = \frac{Q_c \cdot (T_{cf} - T_c)}{V_c} + \frac{U \cdot A}{\rho_c \cdot c_{p_c} \cdot V_c} \cdot (T - T_c)$$
$$\frac{\mathrm{d}D_0}{\mathrm{d}t} = 0.5 \cdot k_t \cdot C_{gp}^2 - \frac{Q_t \cdot D_0}{V}$$

$$
\begin{aligned}
\frac{\mathrm{d}D_1}{\mathrm{d}t} &= k_p \cdot C_m \cdot C_{gp} - \frac{Q_t \cdot D_1}{V} \\
Q_t &= Q_m + Q_i + Q_s \\
C_{gp} &= \sqrt{\frac{2 \cdot f \cdot k_d \cdot C_i}{k_t}} \\
k_i &= k_{0i} \exp\left(-\frac{E_i}{T}\right) && i \in \{d, p, t\} \\
P_{NAMW} &= \frac{D_1}{D_0} \cdot MW_m
\end{aligned}
$$

where C_{if} is the initiator feed concentration, Q_i the initiator flow rate, Q_t the total flow rate, C_i the initiator concentration, V is the reactor volume and k_d is the reaction rate of the initiation reaction. C_{mf} is the monomer feed concentration, Q_m the monomer flow rate, C_m the monomer concentration, k_p the reaction rate of the propagation reaction and C_{gp} the concentration of growing polymer. T is the reactor temperature, T_f the feed temperature, ΔH_r the propagation reaction enthalpy, ρ the reactor content density, c_p the reactor content heat capacity, U the heat transfer coefficient from the reactor content to the coolant, A the area of heat exchange between the reactor and cooling jacket and T_c the coolant temperature in the jacket. Q_c is the coolant flow rate, T_{cf} the coolant feed temperature, ρ_c is the coolant density, c_{p_c} the coolant heat capacity and V_c the jacket volume. k_t is the reaction rate of the termination reaction, D_0 is the zeroth moment and D_1 the first moment. The initiator efficiency is denoted by f, E_i with $i \in \{d, p, t\}$ are the activation energies for initiation, propagation and termination and MW_m is the monomer molecular weight. For implementation, we use the dimensionless model as stated in [236, 231].

$$
\begin{aligned}
\frac{\mathrm{d}x_1}{\mathrm{d}t} &= q_i \cdot x_{1f} - q_t \cdot x_1 - \phi_d \cdot k_d \cdot x_1 \\
\frac{\mathrm{d}x_2}{\mathrm{d}t} &= q_m \cdot x_{2f} - q_t \cdot x_2 - \phi_p \cdot k_p \cdot x_2 \cdot x_{gp} \\
\frac{\mathrm{d}x_3}{\mathrm{d}t} &= q_t \cdot (x_{3f} - x_3) + \beta \cdot \phi_p \cdot k_p \cdot x_2 \cdot x_{gp} - \delta \cdot (x_3 - x_4) \\
\frac{\mathrm{d}x_4}{\mathrm{d}t} &= \delta_1 \cdot (q_c \cdot (x_{4f} - x_4) + \delta \cdot \delta_2 \, (x3 - x4)) \\
\frac{\mathrm{d}x_5}{\mathrm{d}t} &= \frac{1}{2} \cdot \phi_t \cdot k_t \cdot x_{gp}^2 - q_t \cdot x_5 \\
\frac{\mathrm{d}x_6}{\mathrm{d}t} &= \phi_p \cdot k_p \cdot x_2 \cdot x_{gp} - q_t \cdot x_6 \\
q_t &= q_i + q_m + q_s
\end{aligned}
$$

$$x_{gp} = \sqrt{\frac{2 \cdot f \cdot \phi_d \cdot k_d}{\phi_t \cdot k_t} \cdot x_1}$$
$$p_{NAMW} = \frac{x_6}{x_5}$$

where x_1 is the dimensionless initiator concentration, x_2 is the dimensionless monomer concentration, x_3 is the dimensionless reactor temperature, x_4 is the dimensionless cooling jacket temperature and x_5 and x_6 are the dimensionless zeroth and first moments.

Appendix D

uANN pseudo code implementation

The implementation of uANN is described in Algorithm 1.

Algorithm 1 uANN

for iTimeStep **do**
  obtain $\boldsymbol{x}$, $\boldsymbol{d}$, and $\boldsymbol{p}$
  predict $\underline{\hat{\mathbf{u}}} = f^{iANN}(\boldsymbol{x}, \boldsymbol{d}, \boldsymbol{p})$
  calculate $\mathcal{L}_{\boldsymbol{uu}}$, $\Phi_{\boldsymbol{u}}$ and $\boldsymbol{h}_{\boldsymbol{u}}$
  while $\Delta \boldsymbol{u}$ not found **do**
    obtain $\Delta \boldsymbol{u}$ by solving (8.5a)-(8.5b)
    if $\mathcal{L}_{\boldsymbol{uu}}$ not positive definite **then**
      Modify $\mathcal{L}_{\boldsymbol{uu}}$
    end if
    if (8.5a)-(8.5b) infeasible **then**
      solve (8.7a)-(8.7b)
    end if
  end while
  $\underline{\mathbf{u}} = \underline{\hat{\mathbf{u}}} + \Delta \boldsymbol{u}$
  apply $\boldsymbol{u}_0$ to plant and shift time
end for

Appendix E

Training results for $\boldsymbol{f}^{\mathrm{dANN}}$ and $\boldsymbol{f}^{\mathrm{iANN}}$

$\boldsymbol{f}^{\mathrm{dANN}}$ and $\boldsymbol{f}^{\mathrm{iANN}}$ were trained with TensorFlow [237] using the Keras interface [238] and the `adam` [239] optimizer. The mean squared error (mse) was used as loss function. We tested several configurations of shallow and deep neural networks ranging from one to six dense hidden layers with hyperbolic tangent activation function. All configurations consisted of a total of 60 neurons. To obtain reliable results, we carried out five training runs for each configuration. The maximum number of epochs was 1000. We used early stopping after 50 epochs without improvement of the mse on the validation set which contained 20% of the data. The targets for the ANNs, i.e., the entries of $\underline{\boldsymbol{u}_0}$ and $\underline{\underline{\mathbf{u}}}$ were scaled to be in between 0 and 1.

The validation loss for $\boldsymbol{f}^{\mathrm{dANN}}$ is illustrated in Fig. E.1a and for $\boldsymbol{f}^{\mathrm{iANN}}$ in Fig. E.1b. We

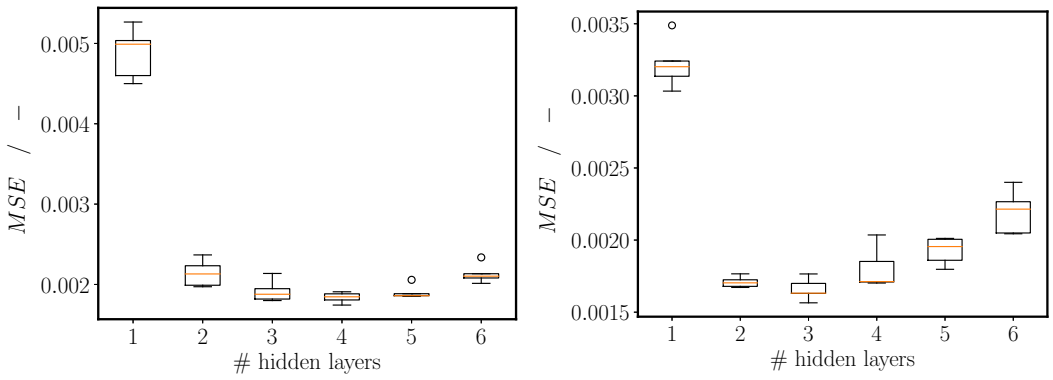

(a) $\boldsymbol{f}^{\mathrm{dANN}}$ (b) $\boldsymbol{f}^{\mathrm{iANN}}$

Figure E.1: Validation losses for $\boldsymbol{f}^{\mathrm{dANN}}$ and $\boldsymbol{f}^{\mathrm{iANN}}$. Deep ANNs perform better than shallow ANNs.

can see that shallow network performs significantly worse than deep networks as was also found in [27]. Moreover, the shallow networks required more epochs for training which is in accordance with the state-of-the-art in deep learning [109]. We can see that neither for $\boldsymbol{f}^{\mathrm{dANN}}$ nor for $\boldsymbol{f}^{\mathrm{iANN}}$ the largest number of hidden layer yields the best result. However, unless a shallow ANN is chosen, the differences in performance are small. We found that using ReLU as activation functions yielded larger mse values than the hyperbolic tangent. We select an ANN with four hidden layers for $\boldsymbol{f}^{\mathrm{dANN}}$ and an ANN with three hidden layers for $\boldsymbol{f}^{\mathrm{iANN}}$ for the remainder of this manuscript, as these exhibited the best validation performances. In both cases, the instances with the smallest validation loss also exhibited the smallest loss on the training set.

Bibliography

[1] W. R. Huster, Y. Vaupel, A. Mhamdi, and A. Mitsos, "Validated dynamic model of an organic Rankine cycle (ORC) for waste heat recovery in a diesel truck," *Energy*, vol. 151, pp. 647–661, 2018.

[2] Y. Vaupel, W. R. Huster, F. Holtorf, A. Mhamdi, and A. Mitsos, "Analysis and improvement of dynamic heat exchanger models for nominal and start-up operation," *Energy*, vol. 169, pp. 1191–1201, 2019.

[3] Y. Vaupel, W. R. Huster, A. Mhamdi, and A. Mitsos, "Optimal operating policies for organic Rankine cycles for waste recovery under transient conditions," *Submitted*, 05 March 2020.

[4] Y. Vaupel, W. R. Huster, A. Mhamdi, and A. Mitsos, "Optimal operating policies for organic Rankine cycles for waste heat recovery under transient conditions," *arXiv:2101.03381*, 2021.

[5] Y. Vaupel, J. C. Schulze, A. Mhamdi, and A. Mitsos, "Nonlinear model predictive control of organic Rankine cycles for automotive waste heat recovery: Is it worth the effort?," *Journal of Process Control*, vol. 99, pp. 19–27, mar 2021.

[6] Y. Vaupel, A. Caspari, N. C. Hamacher, W. R. Huster, A. Mhamdi, I. G. Kevrekidis, and A. Mitsos, "Artificial neural networks for real-time model predictive control of organic Rankine cycles for waste heat recovery," in *Proceedings of the 5th international seminar on ORC power systems*, 2019.

[7] Y. Vaupel, N. C. Hamacher, A. Caspari, A. Mhamdi, I. G. Kevrekidis, and A. Mitsos, "Accelerating nonlinear model predictive control through machine learning," *Journal of Process Control*, vol. 92, pp. 261–270, 2020.

[8] L. A. Mey, "Process modeling and comparative assessment of separation techniques for high salinity brine treatment," Project thesis, RWTH Aachen University, 2016.

[9] J. Wiebe, "Online stress estimation for plate fin heat exchangers – a data-driven approach," Master's thesis, RWTH Aachen University, 2016.

[10] C. Köhler, "Dynamic optimization and nonlinear model predictive control of an automotive waste heat recovery system," Master's thesis, RWTH Aachen University, 2017.

[11] N. C. Hamacher, "Real-time capable model predictive control employing artificial neural networks," Bachelor's thesis, RWTH Aachen University, 2019.

[12] J. C. Schulze, "Nonlinear model predictive control of a waste heat recovery system using fast-update methods," Master's thesis, RWTH Aachen University, 2019.

[13] B. Bier, "Comparison of advanced control methods for optimal operation of a waste heat recovery system in a heavy-duty diesel truck," Master's thesis, RWTH Aachen University, 2020.

[14] A. Manchanda, "Modelling and dynamic optimization of organic rankine cycle with complementarity constraints," Master's thesis, RWTH Aachen University, 2020.

[15] A. Zingler, "Combination of machine learning and fast-update methods in model predictive control," Master's thesis, RWTH Aachen University, 2020.

[16] R. K. Pachauri, M. R. Allen, V. R. Barros, J. Broome, W. Cramer, R. Christ, J. A. Church, L. Clarke, Q. Dahe, P. Dasgupta, N. K. Dubash, O. Edenhofer, I. Elgizouli, C. B. Field, P. Forster, P. Friedlingstein, J. Fuglestvedt, L. Gomez-Echeverri, S. Hallegatte, G. Hegerl, M. Howden, K. Jiang, B. J. Cisneroz, V. Kattsov, H. Lee, K. J. Mach, J. Marotzke, M. D. Mastrandrea, L. Meyer, J. Minx, Y. Mulugetta, K. O'Brien, M. Oppenheimer, J. J. Pereira, R. Pichs-Madruga, G.-K. Plattner, H.-O. Pörtner, S. B. Power, B. Preston, N. H. Ravindranath, A. Reisinger, K. Riahi, M. Rusticucci, R. Scholes, K. Seyboth, Y. Sokona, R. Stavins, T. F. Stocker, P. Tschakert, D. van Vuuren, and J.-P. van Ypserle, *Climate Change 2014: Synthesis Report. Contribution of Working Groups I, II and III to the Fifth Assessment Report of the Intergovernmental Panel on Climate Change*. Geneva, Switzerland: IPCC, 2014.

[17] G. Santos, "Road transport and CO 2 emissions: What are the challenges?," *Transport Policy*, vol. 59, pp. 71–74, 2017.

[18] European Parliament, "Regulation (EC) No 715/2007 of the European Parliament and of the Council of 20 June 2007 on type approval of motor vehicles with respect to emissions from light passenger and commercial vehicles (Euro 5 and Euro 6) and on access to vehicle repair and maintenance information (Text with EEA relevance)," 2007.

[19] D. W. Stanton, "Systematic development of highly efficient and clean engines to meet future commercial vehicle greenhouse gas regulations," *SAE International Journal of Engines*, vol. 6, no. 3, pp. 1395–1480, 2013.

[20] A. A. Boretti, "Energy recovery in passenger cars," *Journal of Energy Resources Technology*, vol. 134, no. 2, 2012.

[21] V. Zare, "A comparative exergoeconomic analysis of different ORC configurations for binary geothermal power plants," *Energy Conversion and Management*, vol. 105, pp. 127–138, 2015.

[22] F. Campana, M. Bianchi, L. Branchini, A. D. Pascale, A. Peretto, M. Baresi, A. Fermi, N. Rossetti, and R. Vescovo, "ORC waste heat recovery in european energy intensive industries: Energy and GHG savings," *Energy Conversion and Management*, vol. 76, pp. 244–252, 2013.

[23] L. T. Biegler, *Nonlinear programming: Concepts, algorithms, and applications to chemical processes*. Philadelphia: Society for Industrial and Applied Mathematics and Mathematical Programming Society, 2010.

[24] M. Ellis, H. Durand, and P. D. Christofides, "A tutorial review of economic model predictive control methods," *Journal of Process Control*, vol. 24, no. 8, pp. 1156–1178, 2014.

[25] A. Bemporad, M. Morari, V. Dua, and E. N. Pistikopoulos, "The explicit linear quadratic regulator for constrained systems," *Automatica*, vol. 38, no. 1, pp. 3–20, 2002.

[26] I. J. Wolf and W. Marquardt, "Fast NMPC schemes for regulatory and economic NMPC – a review," *Journal of Process Control*, vol. 44, pp. 162–183, 2016.

[27] S. Lucia and B. Karg, "A deep learning-based approach to robust nonlinear model predictive control," *IFAC-PapersOnLine*, vol. 51, no. 20, pp. 511–516, 2018.

[28] J. M. Jensen, *Dynamic modeling of thermo-fluid systems: With focus on evaporators for refrigeration*, vol. 2003-01 of *MEK-ET-PHD*. Lyngby: Department of Mechanical Engineering, Technical University of Denmark, 2003.

[29] A. C. Askin, G. E. Barter, T. H. West, and D. K. Manley, "The heavy-duty vehicle future in the united states: A parametric analysis of technology and policy tradeoffs," *Energy Policy*, vol. 81, pp. 1–13, jun 2015.

[30] C. Sprouse, III and C. Depcik, "Review of organic Rankine cycles for internal combustion engine exhaust waste heat recovery," *Applied Thermal Engineering*, vol. 51, no. 1–2, pp. 711–722, 2013.

[31] A. T. Hoang, "Waste heat recovery from diesel engines based on organic rankine cycle," *Applied Energy*, vol. 231, pp. 138–166, 2018.

[32] A. Cozzolini, M. C. Besch, D. Littera, H. Kappanna, P. Bonsack, M. Gautam, S. Cordiner, and V. Mulone, "Waste heat recovery in heavy-duty diesel engines: A thermodynamic analysis of waste heat availability for implementation of energy recovery systems based upon the organic rankine cycle," in *ASME 2012 Internal Combustion Engine Division Spring Technical Conference*, American Society of Mechanical Engineers, 2012.

[33] J. Fu, J. Liu, R. Feng, Y. Yang, L. Wang, and Y. Wang, "Energy and exergy analysis on gasoline engine based on mapping characteristics experiment," *Applied Energy*, vol. 102, pp. 622–630, 2013.

[34] N. Espinosa, M. Lazard, L. Aixala, and H. Scherrer, "Modeling a thermoelectric generator applied to diesel automotive heat recovery," *Journal of Electronic Materials*, vol. 39, no. 9, pp. 1446–1455, 2010.

[35] D. Hountalas, C. Katsanos, and V. Lamaris, "Recovering energy from the diesel engine exhaust using mechanical and electrical turbocompounding," in *SAE Technical Paper Series*, SAE International, 2007.

[36] L. E. Bell, "Cooling, heating, generating power, and recovering waste heat with thermoelectric systems," *Science*, vol. 321, no. 5895, pp. 1457–1461, 2008.

[37] B. Orr, A. Akbarzadeh, M. Mochizuki, and R. Singh, "A review of car waste heat recovery systems utilising thermoelectric generators and heat pipes," *Applied Thermal Engineering*, vol. 101, pp. 490–495, 2016.

[38] H. Goldsmid, "Bismuth telluride and its alloys as materials for thermoelectric generation," *Materials*, vol. 7, no. 4, pp. 2577–2592, 2014.

[39] R. Stobart and D. Milner, "The potential for thermo-electric regeneration of energy in vehicles," in *SAE Technical Paper Series*, SAE International, 2009.

[40] J. LaGrandeur, D. Crane, S. Hung, B. Mazar, and A. Eder, "Automotive waste heat conversion to electric power using skutterudite, TAGS, PbTe and BiTe," in *2006 25th International Conference on Thermoelectrics*, IEEE, 2006.

[41] Q. E. Hussain, D. R. Brigham, and C. W. Maranville, "Thermoelectric exhaust heat recovery for hybrid vehicles," *SAE International Journal of Engines*, vol. 2, no. 1, pp. 1132–1142, 2009.

[42] M. Mori, T. Yamagami, M. Sorazawa, T. Miyabe, S. Takahashi, and T. Haraguchi, "Simulation of fuel economy effectiveness of exhaust heat recovery system using thermoelectric generator in a series hybrid," *SAE International Journal of Materials and Manufacturing*, vol. 4, no. 1, pp. 1268–1276, 2011.

[43] H. Ghasemi, M. Paci, A. Tizzanini, and A. Mitsos, "Modeling and optimization of a binary geothermal power plant," *Energy*, vol. 50, pp. 412–428, 2013.

[44] S. Quoilin, M. Orosz, H. Hemond, and V. Lemort, "Performance and design optimization of a low-cost solar organic Rankine cycle for remote power generation," *Solar Energy*, vol. 85, no. 5, pp. 955–966, 2011.

[45] R. Pili, A. Romagnoli, K. Kamossa, A. Schuster, H. Spliethoff, and C. Wieland, "Organic rankine cycles (ORC) for mobile applications – economic feasibility in different transportation sectors," *Applied Energy*, vol. 204, pp. 1188–1197, 2017.

[46] D. V. Singh and E. Pedersen, "A review of waste heat recovery technologies for maritime applications," *Energy Conversion and Management*, vol. 111, pp. 315–328, 2016.

[47] J. Peralez, P. Tona, M. Nadri, P. Dufour, and A. Sciarretta, "Optimal control for an organic rankine cycle on board a diesel-electric railcar," *Journal of Process Control*, vol. 33, pp. 1–13, 2015.

[48] E. Macchi and M. Astolfi, *Organic rankine cycle (ORC) power systems: technologies and applications*. Woodhead Publishing, 2016.

[49] J. Bao and L. Zhao, "A review of working fluid and expander selections for organic Rankine cycle," *Renewable and Sustainable Energy Reviews*, vol. 24, pp. 325–342, 2013.

[50] B. Xu, D. Rathod, A. Yebi, Z. Filipi, S. Onori, and M. Hoffman, "A comprehensive review of organic rankine cycle waste heat recovery systems in heavy-duty diesel engine applications," *Renewable and Sustainable Energy Reviews*, vol. 107, pp. 145–170, 2019.

[51] S. Lion, C. N. Michos, I. Vlaskos, C. Rouaud, and R. Taccani, "A review of waste heat recovery and organic rankine cycles (ORC) in on-off highway vehicle heavy duty diesel engine applications," *Renewable and Sustainable Energy Reviews*, vol. 79, pp. 691–708, 2017.

[52] K. Eichler, *Development of a Holistic Simulation Methodology for an Organic Rankine Cycle Using the Example of a Commercial Vehicle Application.* PhD thesis, RWTH Aachen University, 2020.

[53] T. Endo, S. Kawajiri, Y. Kojima, K. Takahashi, T. Baba, S. Ibaraki, T. Takahashi, and M. Shinohara, "Study on maximizing exergy in automotive engines," in *SAE Technical Paper Series*, SAE International, 2007.

[54] J. Ringler, M. Seifert, V. Guyotot, and W. Hübner, "Rankine cycle for waste heat recovery of IC engines," *SAE International Journal of Engines*, vol. 2, no. 1, pp. 67–76, 2009.

[55] T. A. Horst, H.-S. Rottengruber, M. Seifert, and J. Ringler, "Dynamic heat exchanger model for performance prediction and control system design of automotive waste heat recovery systems," *Applied Energy*, vol. 105, pp. 293–303, 2013.

[56] T. A. Horst, W. Tegethoff, P. Eilts, and J. Koehler, "Prediction of dynamic Rankine Cycle waste heat recovery performance and fuel saving potential in passenger car applications considering interactions with vehicles' energy management," *Energy Conversion and Management*, vol. 78, pp. 438–451, 2014.

[57] A. Boretti, "Recovery of exhaust and coolant heat with R245fa organic Rankine cycles in a hybrid passenger car with a naturally aspirated gasoline engine," *Applied Thermal Engineering*, vol. 36, pp. 73–77, 2012.

[58] S. Lecompte, H. Huisseune, M. van den Broek, B. Vanslambrouck, and M. D. Paepe, "Review of organic rankine cycle (ORC) architectures for waste heat

recovery," *Renewable and Sustainable Energy Reviews*, vol. 47, pp. 448–461, 2015.

[59] V. Grelet, T. Reiche, V. Lemort, M. Nadri, and P. Dufour, "Transient performance evaluation of waste heat recovery rankine cycle based system for heavy duty trucks," *Applied Energy*, vol. 165, pp. 878–892, 2016.

[60] H. Teng, J. Klaver, T. Park, G. L. Hunter, and B. van der Velde, "A rankine cycle system for recovering waste heat from HD diesel engines - WHR system development," in *SAE Technical Paper Series*, SAE International, 2011.

[61] C. Yue, D. Han, W. Pu, and W. He, "Comparative analysis of a bottoming transcritical ORC and a kalina cycle for engine exhaust heat recovery," *Energy Conversion and Management*, vol. 89, pp. 764–774, 2015.

[62] L. Shi, G. Shu, H. Tian, and S. Deng, "A review of modified organic rankine cycles (ORCs) for internal combustion engine waste heat recovery (ICE-WHR)," *Renewable and Sustainable Energy Reviews*, vol. 92, pp. 95–110, 2018.

[63] P. Tona and J. Peralez, "Control of Organic Rankine Cycle Systems on board Heavy-Duty Vehicles: a Survey," *IFAC-PapersOnLine*, vol. 48, no. 15, pp. 419–426, 2015.

[64] A. P. Weiß, "Volumetric expander versus turbine–which is the better choice for small orc plants," in *3rd International Seminar on ORC Power Systems, Oktober*, pp. 12–14, 2015.

[65] F. Pantano and R. Capata, "Expander selection for an on board ORC energy recovery system," *Energy*, vol. 141, pp. 1084–1096, 2017.

[66] M. Hatami, D. D. Ganji, and M. Gorji-Bandpy, "A review of different heat exchangers designs for increasing the diesel exhaust waste heat recovery," *Renewable and Sustainable Energy Reviews*, vol. 37, pp. 168–181, 2014.

[67] V. Pandiyarajan, M. C. Pandian, E. Malan, R. Velraj, and R. V. Seeniraj, "Experimental investigation on heat recovery from diesel engine exhaust using finned shell and tube heat exchanger and thermal storage system," *Applied Energy*, vol. 88, no. 1, pp. 77–87, 2011.

[68] P. Linke, A. Papadopoulos, and P. Seferlis, "Systematic methods for working fluid selection and the design, integration and control of organic rankine cycles—a review," *Energies*, vol. 8, no. 6, pp. 4755–4801, 2015.

[69] T. C. Hung, S. K. Wang, C. H. Kuo, B. S. Pei, and K. F. Tsai, "A study of organic working fluids on system efficiency of an ORC using low-grade energy sources," *Energy*, vol. 35, no. 3, pp. 1403–1411, 2010.

[70] M. Lampe, M. Stavrou, H. M. Bücker, J. Gross, and A. Bardow, "Simultaneous Optimization of Working Fluid and Process for Organic Rankine Cycles Using PC-SAFT," *Ind. Eng. Chem. Res.*, vol. 53, no. 21, pp. 8821–8830, 2014.

[71] U. Lee and A. Mitsos, "Optimal multicomponent working fluid of organic Rankine cycle for exergy transfer from liquefied natural gas regasification," *Energy*, vol. 127, pp. 489–501, 2017.

[72] F. Heberle and D. Brüggemann, "Exergy based fluid selection for a geothermal Organic Rankine Cycle for combined heat and power generation," *Applied Thermal Engineering*, vol. 30, no. 11-12, pp. 1326–1332, 2010.

[73] G. Angelino and P. Colonna di Paliano, "Multicomponent Working Fluids For Organic Rankine Cycles (ORCs)," *Energy*, vol. 23, no. 6, pp. 449–463, 1998.

[74] W. R. Huster, A. M. Schweidtmann, and A. Mitsos, "Globally optimal working fluid mixture composition for geothermal power cycles," *submitted to Energy*, 2020.

[75] X. Wang, G. Shu, H. Tian, P. Liu, D. Jing, and X. Li, "Dynamic analysis of the dual-loop Organic Rankine Cycle for waste heat recovery of a natural gas engine," *Energy Conversion and Management*, vol. 148, pp. 724–736, 2017.

[76] E. H. Wang, H. G. Zhang, B. Y. Fan, M. G. Ouyang, Y. Zhao, and Q. H. Mu, "Study of working fluid selection of organic rankine cycle (ORC) for engine waste heat recovery," *Energy*, vol. 36, no. 5, pp. 3406–3418, 2011.

[77] S. Amicabile, J.-I. Lee, and D. Kum, "A comprehensive design methodology of organic rankine cycles for the waste heat recovery of automotive heavy-duty diesel engines," *Applied Thermal Engineering*, vol. 87, pp. 574–585, 2015.

[78] W. R. Huster, A. M. Schweidtmann, and A. Mitsos, "Working fluid selection for organic rankine cycles via deterministic global optimization of design and operation," *Optimization and Engineering*, vol. 21, no. 2, pp. 517–536, 2019.

[79] D. Tillmanns, J. Petzschmann, J. Schilling, C. Gertig, and A. Bardow, "ORC on tour: Integrated design of dynamic ORC processes and working fluids for waste-heat recovery from heavy-duty vehicles," in *Computer Aided Chemical Engineering*, pp. 163–168, Elsevier, 2019.

[80] J. Schilling, K. Eichler, B. Kölsch, S. Pischinger, and A. Bardow, "Integrated design of working fluid and organic rankine cycle utilizing transient exhaust gases of heavy-duty vehicles," *Applied Energy*, vol. 255, p. 113207, 2019.

[81] B. Chachuat, "Nonlinear and dynamic optimization: From theory to practice," tech. rep., 2007.

[82] R. W. H. Sargent and G. R. Sullivan, "The development of an efficient optimal control package," in *Optimization Techniques*, pp. 158–168, Springer-Verlag, 1978.

[83] L. T. Biegler, "Solution of dynamic optimization problems by successive quadratic programming and orthogonal collocation," *Computers & Chemical Engineering*, vol. 8, no. 3-4, pp. 243–247, 1984.

[84] H. G. Bock and K. J. Plitt, "A multiple shooting algorithm for direct solution of optimal control problems," *IFAC Proceedings Volumes*, vol. 17, no. 2, pp. 1603–1608, 1984.

[85] A. Wächter and L. T. Biegler, "On the implementation of an interior-point filter line-search algorithm for large-scale nonlinear programming," *Mathematical Programming*, vol. 106, no. 1, pp. 25–57, 2005.

[86] T. Binder, L. Blank, H. G. Bock, R. Bulirsch, W. Dahmen, M. Diehl, T. Kronseder, W. Marquardt, J. P. Schlöder, and O. von Stryk, "Introduction to model based optimization of chemical processes on moving horizons," in *Online Optimization of Large Scale Systems*, pp. 295–339, Springer Berlin Heidelberg, 2001.

[87] J. Fu, J. M. M. Faust, B. Chachuat, and A. Mitsos, "Local optimization of dynamic programs with guaranteed satisfaction of path constraints," *Automatica*, vol. 62, pp. 184–192, 2015.

[88] E. S. Schultz, R. Hannemann-Tamás, and A. Mitsos, "Guaranteed satisfaction of inequality state constraints in PDE-constrained optimization," *Automatica*, vol. 111, p. 108653, 2020.

[89] P. E. Gill, W. Murray, and M. A. Saunders, "SNOPT: An SQP algorithm for large-scale constrained optimization," *SIAM Review*, vol. 47, no. 1, pp. 99–131, 2005.

[90] J. B. Rawlings, D. Q. Mayne, and M. Diehl, *Model Predictive Control: Theory, Computation, and Design*. Nob Hill Publishing, 2017.

[91] R. Findeisen and F. Allgöwer, "An introduction to nonlinear model predictive control," in *21st Benelux meeting on systems and control*, vol. 11, pp. 119–141, Technische Universiteit Eindhoven Veldhoven Eindhoven, The Netherlands, 2002.

[92] S. J. Qin and T. A. Badgwell, "A survey of industrial model predictive control technology," *Control Engineering Practice*, vol. 11, no. 7, pp. 733–764, 2003.

[93] A. Mitsos, N. Asprion, C. A. Floudas, M. Bortz, M. Baldea, D. Bonvin, A. Caspari, and P. Schäfer, "Challenges in process optimization for new feedstocks and energy sources," *Computers & Chemical Engineering*, vol. 113, pp. 209–221, 2018.

[94] J. B. Rawlings and C. T. Maravelias, "Bringing new technologies and approaches to the operation and control of chemical process systems," *AIChE Journal*, vol. 65, no. 6, p. e16615, 2019.

[95] D. Q. Mayne, "Model predictive control: Recent developments and future promise," *Automatica*, vol. 50, no. 12, pp. 2967–2986, 2014.

[96] D. Q. Mayne, J. B. Rawlings, C. V. Rao, and P. O. M. Scokaert, "Constrained model predictive control: Stability and optimality," *Automatica*, vol. 36, no. 6, pp. 789–814, 2000.

[97] L. Grüne and J. Pannek, *Nonlinear Model Predictive Control*. Springer International Publishing, 2017.

[98] J. Puschke, H. Djelassi, J. Kleinekorte, R. Hannemann-Tamás, and A. Mitsos, "Robust dynamic optimization of batch processes under parametric uncertainty: Utilizing approaches from semi-infinite programs," *Computers & Chemical Engineering*, vol. 116, pp. 253–267, 2018.

[99] S. Lucia, T. Finkler, and S. Engell, "Multi-stage nonlinear model predictive control applied to a semi-batch polymerization reactor under uncertainty," *Journal of Process Control*, vol. 23, no. 9, pp. 1306–1319, 2013.

[100] R. Huang, E. Harinath, and L. T. Biegler, "Lyapunov stability of economically oriented NMPC for cyclic processes," *Journal of Process Control*, vol. 21, no. 4, pp. 501–509, 2011.

[101] J. V. Kadam and W. Marquardt, "Sensitivity-based solution updates in closed-loop dynamic optimization," *IFAC Proceedings Volumes*, vol. 37, no. 9, pp. 947–952, 2004.

[102] L. Würth, R. Hannemann, and W. Marquardt, "Neighboring-extremal updates for nonlinear model-predictive control and dynamic real-time optimization," *Journal of Process Control*, vol. 19, no. 8, pp. 1277–1288, 2009.

[103] C. M. Bishop, *Pattern Recognition and Machine Learning*. Springer New York, 2016.

[104] D. M. Himmelblau, "Accounts of experiences in the application of artificial neural networks in chemical engineering," *Industrial & Engineering Chemistry Research*, vol. 47, no. 16, pp. 5782–5796, 2008.

[105] S. Haykin, *Neural networks and learning machines*. New York: Prentice Hall/Pearson, 2009.

[106] W. S. McCulloch and W. Pitts, "A logical calculus of the ideas immanent in nervous activity," *The Bulletin of Mathematical Biophysics*, vol. 5, no. 4, pp. 115–133, 1943.

[107] G. Cybenko, "Approximation by superpositions of a sigmoidal function," *Mathematics of Control, Signals, and Systems*, vol. 2, no. 4, pp. 303–314, 1989.

[108] K. Hornik, M. Stinchcombe, and H. White, "Multilayer feedforward networks are universal approximators," *Neural Networks*, vol. 2, no. 5, pp. 359–366, 1989.

[109] Y. LeCun, Y. Bengio, and G. Hinton, "Deep learning," *Nature*, vol. 521, no. 7553, pp. 436–444, 2015.

[110] S. Hochreiter, "The vanishing gradient problem during learning recurrent neural nets and problem solutions," *International Journal of Uncertainty, Fuzziness and Knowledge-Based Systems*, vol. 06, no. 02, pp. 107–116, 1998.

[111] S. Geman, E. Bienenstock, and R. Doursat, "Neural networks and the bias/variance dilemma," *Neural Computation*, vol. 4, no. 1, pp. 1–58, 1992.

[112] D. C. Psichogios and L. H. Ungar, "A hybrid neural network-first principles approach to process modeling," *AIChE Journal*, vol. 38, no. 10, pp. 1499–1511, 1992.

[113] M. von Stosch, R. Oliveira, J. Peres, and S. F. de Azevedo, "Hybrid semi-parametric modeling in process systems engineering: Past, present and future," *Computers & Chemical Engineering*, vol. 60, pp. 86–101, 2014.

[114] V. Venkatasubramanian, "The promise of artificial intelligence in chemical engineering: Is it here, finally?," *AIChE Journal*, vol. 65, no. 2, pp. 466–478, 2018.

[115] A. M. Schweidtmann, W. R. Huster, J. T. Lüthje, and A. Mitsos, "Deterministic global process optimization: Accurate (single-species) properties via artificial neural networks," *Computers & Chemical Engineering*, vol. 121, pp. 67–74, 2019.

[116] J. A. Schroeder, S. G. Penoncello, and J. S. Schroeder, "A Fundamental Equation of State for Ethanol," *Journal of Physical and Chemical Reference Data*, vol. 43, no. 4, p. 043102, 2014.

[117] H. Xie and C. Yang, "Dynamic behavior of Rankine cycle system for waste heat recovery of heavy duty diesel engines under driving cycle," *Applied Energy*, vol. 112, pp. 130–141, 2013.

[118] S. Quoilin, R. Aumann, A. Grill, A. Schuster, V. Lemort, and H. Spliethoff, "Dynamic modeling and optimal control strategy of waste heat recovery Organic Rankine Cycles," *Applied Energy*, vol. 88, no. 6, pp. 2183–2190, 2011.

[119] A. Desideri, B. Dechesne, J. Wronski, M. van den Broek, S. Gusev, V. Lemort, and S. Quoilin, "Comparison of Moving Boundary and Finite-Volume Heat Exchanger Models in the Modelica Language," *Energies*, vol. 9, no. 5, p. 339, 2016.

[120] H. Pangborn, A. G. Alleyne, and N. Wu, "A comparison between finite volume and switched moving boundary approaches for dynamic vapor compression system modeling," *International Journal of Refrigeration*, vol. 53, pp. 101–114, 2015.

[121] S. Bendapudi, J. E. Braun, and E. A. Groll, "A comparison of moving-boundary and finite-volume formulations for transients in centrifugal chillers," *International Journal of Refrigeration*, vol. 31, no. 8, pp. 1437–1452, 2008.

[122] E. Rodriguez and B. Rasmussen, "A comparison of modeling paradigms for dynamic evaporator simulations with variable fluid phases," *Applied Thermal Engineering*, vol. 112, pp. 1326–1342, 2017.

[123] M. Crialesi Esposito, N. Pompini, A. Gambarotta, V. Chandrasekaran, J. Zhou, and M. Canova, "Nonlinear Model Predictive Control of an Organic Rankine Cycle for Exhaust Waste Heat Recovery in Automotive Engines," *IFAC-PapersOnLine*, vol. 48, no. 15, pp. 411–418, 2015.

[124] D. Jolevski, O. Bego, and P. Sarajcev, "Control structure design and dynamics modelling of the organic Rankine cycle system," *Energy*, vol. 121, pp. 193–204, 2017.

[125] A. Hernandez, A. Desideri, C. Ionescu, S. Quoilin, V. Lemort, and R. de Keyser, "Increasing the eciency of Organic Rankine Cycle Technology by means of Multivariable Predictive Control," *The International Federation of Automatic Control, Cape Town, South Africa. August 24-29, 2014*, 2014.

[126] E. Feru, F. Willems, B. de Jager, and M. Steinbuch, "Model predictive control of a waste heat recovery system for automotive diesel engines," *18th International Conference on System Theory, Control and Computing (ICSTCC)*, pp. 658–663, 2014.

[127] J. Zhang, Y. Zhou, R. Wang, J. Xu, and F. Fang, "Modeling and constrained multivariable predictive control for ORC (Organic Rankine Cycle) based waste heat energy conversion systems," *Energy*, vol. 66, pp. 128–138, 2014.

[128] M. Willatzen, N. B. O. L. Pettit, and L. Ploug-Sørensen, "A general dynamic simulation model for evaporators and condensers in refrigeration. Part I: moving-boundary formulation of two-phase flows with heat exchange," *International Journal of Refrigeration*, vol. 21, no. 5, pp. 398–403, 1998.

[129] N. B. O. L. Pettit, M. Willatzen, and L. Ploug-Sørensen, "A general dynamic simulation model for evaporators and condensers in refrigeration. Part II: simulation and control of an evaporator," *International Journal of Refrigeration*, vol. 21, no. 5, pp. 404–414, 1998.

[130] W.-J. Zhang and C.-L. Zhang, "A generalized moving-boundary model for transient simulation of dry-expansion evaporators under larger disturbances," *International Journal of Refrigeration*, vol. 29, no. 7, pp. 1119–1127, 2006.

[131] T. L. McKinley and A. G. Alleyne, "An advanced nonlinear switched heat exchanger model for vapor compression cycles using the moving-boundary method," *International Journal of Refrigeration*, vol. 31, no. 7, pp. 1253–1264, 2008.

[132] J. Bonilla, S. Dormido, and F. E. Cellier, "Switching moving boundary models for two-phase flow evaporators and condensers," *Communications in Nonlinear Science and Numerical Simulation*, vol. 20, no. 3, pp. 743–768, 2015.

[133] M. Crialesi Esposito, N. Pompini, A. Gambarotta, and M. Canova, "A switching Moving Boundary Model for the simulation of ORC plants in automotive applications," in *15. Internationales Stuttgarter Symposium* (M. Bargende, H.-C. Reuss, and J. Wiedemann, eds.), Proceedings, pp. 735–753, Wiesbaden: Springer Fachmedien Wiesbaden, 2015.

[134] J. I. Zapata, J. Pye, and K. Lovegrove, "A transient model for the heat exchange in a solar thermal once through cavity receiver," *Solar Energy*, vol. 93, pp. 280–293, 2013.

[135] E. Feru, F. Kupper, C. Rojer, X. Seykens, F. Scappin, F. Willems, J. Smits, B. de Jager, and M. Steinbuch, "Experimental Validation of a Dynamic Waste Heat Recovery System Model for Control Purposes," in *SAE 2013 World Congress & Exhibition*, SAE Technical Paper Series, SAE International400 Commonwealth Drive, Warrendale, PA, United States, 2013.

[136] A. Desideri, A. Hernandez, S. Gusev, M. van den Broek, V. Lemort, and S. Quoilin, "Steady-state and dynamic validation of a small-scale waste heat recovery system using the ThermoCycle Modelica library," *Energy*, vol. 115, pp. 684–696, 2016.

[137] D. Seitz, O. Gehring, C. Bunz, M. Brunschier, and O. Sawodny, "Dynamic Model of a Multi-Evaporator Organic Rankine Cycle for Exhaust Heat Recovery in Automotive Applications," *IFAC-PapersOnLine*, vol. 49, no. 21, pp. 39–46, 2016.

[138] B. Xu, D. Rathod, S. Kulkarni, A. Yebi, Z. Filipi, S. Onori, and M. Hoffman, "Transient dynamic modeling and validation of an organic Rankine cycle waste heat recovery system for heavy duty diesel engine applications," *Applied Energy*, vol. 205, pp. 260–279, 2017.

[139] D. Wei, X. Lu, Z. Lu, and J. Gu, "Dynamic modeling and simulation of an Organic Rankine Cycle (ORC) system for waste heat recovery," *Applied Thermal Engineering*, vol. 28, no. 10, pp. 1216–1224, 2008.

[140] Process Systems Enterprise, "gPROMS ModelBuilder Guide: Release v3.3.0," 2010.

[141] H. E. Dillon and S. G. Penoncello, "A Fundamental Equation for Calculation of the Thermodynamic Properties of Ethanol," *International Journal of Thermophysics*, vol. 25, no. 2, pp. 321–335, 2004.

[142] M. Thorade and A. Saadat, "Partial derivatives of thermodynamic state properties for dynamic simulation," *Environmental Earth Sciences*, vol. 70, no. 8, pp. 3497–3503, 2013.

[143] VDI e. V., *VDI-Wärmeatlas*. VDI-Buch, Berlin, Heidelberg: Springer, 11., bearb. und erw. aufl ed., 2013.

[144] J. C. Leung and M. Epstein, "A Generalized Correlation for Two-Phase Non-flashing Homogeneous Choked Flow," *Journal of Heat Transfer*, vol. 112, no. 2, p. 528, 1990.

[145] A. Michel and A. Kugi, "Accurate low-order dynamic model of a compact plate heat exchanger," *International Journal of Heat and Mass Transfer*, vol. 61, pp. 323–331, 2013.

[146] E. Feru, F. Willems, C. Rojer, B. de Jager, and M. Steinbuch, "Heat Exchanger Modeling and Identification for Control of Waste Heat Recovery Systems in Diesel Engines," *American Control Conference (ACC), Washington, DC, USA, June 17-19, 2013*, 2013.

[147] H. Koppauer, W. Kemmetmüller, and A. Kugi, "Modeling and optimal steady-state operating points of an ORC waste heat recovery system for diesel engines," *Applied Energy*, vol. 206, pp. 329–345, 2017.

[148] D. Seitz, O. Gehring, C. Bunz, M. Brunschier, and O. Sawodny, "Design of a Nonlinear, Dynamic Feedforward Part for the Evaporator Control of an Organic Rankine Cycle in Heavy Duty Vehicles," *IFAC-PapersOnLine*, vol. 49, no. 11, pp. 625–632, 2016.

[149] F. Casella, T. Mathijssen, P. Colonna, and J. van Buijtenen, "Dynamic Modeling of Organic Rankine Cycle Power Systems," *Journal of Engineering for Gas Turbines and Power*, vol. 135, no. 4, p. 042310, 2013.

[150] B. Li and A. G. Alleyne, "A dynamic model of a vapor compression cycle with shut-down and start-up operations," *International Journal of Refrigeration*, vol. 33, no. 3, pp. 538–552, 2010.

[151] X.-D. He, S. Liu, and H. H. Asada, "Modeling of Vapor Compression Cycles for Multivariable Feedback Control of HVAC Systems," *Journal of Dynamic Systems, Measurement, and Control*, vol. 119, no. 2, p. 183, 1997.

[152] M. Eck and T. Hirsch, "Dynamics and control of parabolic trough collector loops with direct steam generation," *Solar Energy*, vol. 81, no. 2, pp. 268–279, 2007.

[153] A. Yebi, B. Xu, X. Liu, J. Shutty, P. Anschel, Z. Filipi, S. Onori, and M. Hoffman, "Estimation and Predictive Control of a Parallel Evaporator Diesel Engine Waste Heat Recovery System," *IEEE Transactions on Control Systems Technology*, pp. 1–14, 2017.

[154] H. Qiao, C. R. Laughman, V. Aute, and R. Radermacher, "An advanced switching moving boundary heat exchanger model with pressure drop," *International Journal of Refrigeration*, vol. 65, pp. 154–171, 2016.

[155] S. Quoilin, I. Bell, A. Desideri, P. Dewallef, and V. Lemort, "Methods to Increase the Robustness of Finite-Volume Flow Models in Thermodynamic Systems," *Energies*, vol. 7, no. 3, pp. 1621–1640, 2014.

[156] J. Bonilla, L. J. Yebra, and S. Dormido, "Mean densities in dynamic mathematical two-phase flow models.," *Computer Modeling in Engineering and Sciences (CMES)*, vol. 67, no. 1, pp. 13–37, 2010.

[157] J. Bonilla, L. J. Yebra, and S. Dormido, "A heuristic method to minimise the chattering problem in dynamic mathematical two-phase flow models," *Mathematical and Computer Modelling*, vol. 54, no. 5-6, pp. 1549–1560, 2011.

[158] J. Bonilla, L. J. Yebra, and S. Dormido, "Chattering in dynamic mathematical two-phase flow models," *Applied Mathematical Modelling*, vol. 36, no. 5, pp. 2067–2081, 2012.

[159] L. Cecchinato and F. Mancini, "An intrinsically mass conservative switched evaporator model adopting the moving-boundary method," *International Journal of Refrigeration*, vol. 35, no. 2, pp. 349–364, 2012.

[160] P. I. Barton and C. C. Pantelides, "Modeling of combined discrete/continuous processes," *AIChE Journal*, vol. 40, no. 6, pp. 966–979, 1994.

[161] S. Quoilin, A. Desideri, J. Wronski, I. Bell, and V. Lemort, "ThermoCycle: A Modelica library for the simulation of thermodynamic systems," in *the 10th International Modelica Conference*, Linköping Electronic Conference Proceedings, pp. 683–692, Linköping University Electronic Press, 2014.

[162] Process Systems Enterprise, "gPROMS ModelBuilder Guide: Release v5.0.1," 2017.

[163] T. Chen, W. Zhuge, Y. Zhang, and L. Zhang, "A novel cascade organic Rankine cycle (ORC) system for waste heat recovery of truck diesel engines," *Energy Conversion and Management*, vol. 138, pp. 210–223, 2017.

[164] S. Skogestad and I. Postlethwaite, *Multivariable feedback control: Analysis and design*. Chichester: Wiley, 2. ed., repr ed., 2010.

[165] Y. Dai, J. Wang, and L. Gao, "Parametric optimization and comparative study of organic Rankine cycle (ORC) for low grade waste heat recovery," *Energy Conversion and Management*, vol. 50, no. 3, pp. 576–582, 2009.

[166] S. Quoilin, S. Declaye, B. F. Tchanche, and V. Lemort, "Thermo-economic optimization of waste heat recovery Organic Rankine Cycles," *Applied Thermal Engineering*, vol. 31, no. 14–15, pp. 2885–2893, 2011.

[167] W. R. Huster, D. Bongartz, and A. Mitsos, "Deterministic global optimization of the design of a geothermal organic rankine cycle," *Energy Procedia*, vol. 129, pp. 50–57, 2017.

[168] D. Wei, X. Lu, Z. Lu, and J. Gu, "Performance analysis and optimization of organic Rankine cycle (ORC) for waste heat recovery," *Energy Conversion and Management*, vol. 48, no. 4, pp. 1113–1119, 2007.

[169] Z. Shengjun, W. Huaixin, and G. Tao, "Performance comparison and parametric optimization of subcritical Organic Rankine Cycle (ORC) and transcritical power cycle system for low-temperature geothermal power generation," *Applied Energy*, vol. 88, no. 8, pp. 2740–2754, 2011.

[170] M. E. Mondejar, F. Ahlgren, M. Thern, and M. Genrup, "Quasi-steady state simulation of an organic rankine cycle for waste heat recovery in a passenger vessel," *Applied Energy*, vol. 185, pp. 1324–1335, 2017.

[171] J. Schilling, K. Eichler, S. Pischinger, and A. Bardow, "Integrated design of ORC process and working fluid for transient waste-heat recovery from heavy-duty vehicles," in *13th International Symposium on Process Systems Engineering (PSE 2018)*, pp. 2443–2448, Elsevier, 2018.

[172] G. Manente, A. Toffolo, A. Lazzaretto, and M. Paci, "An organic rankine cycle off-design model for the search of the optimal control strategy," *Energy*, vol. 58, pp. 97–106, 2013.

[173] T. Eller, F. Heberle, and D. Brüggemann, "Transient simulation of geothermal combined heat and power generation for a resilient energetic and economic evaluation," *Energies*, vol. 12, no. 5, p. 894, 2019.

[174] N. Espinosa, I. Gil-Roman, D. Didiot, V. Lemort, B. Lombard, and S. Quoilin, "Transient Organic Rankine Cycle Modelling for Waste Heat Recovery on a Truck," *24th International Conference on Efficiency, Cost, Optimization, Simulation and Environmental Impact of Energy Systems*, 2011.

[175] P. Tona, J. Peralez, and A. Sciarretta, "Supervision and control prototyping for an engine exhaust gas heat recovery system based on a steam Rankine cycle," *IEEE/ASME International Conference on Advanced Intelligent Mechatronics (AIM)*, pp. 695–701, 2012.

[176] J. Peralez, M. Nadri, P. Dufour, P. Tona, and A. Sciarretta, "Organic rankine cycle for vehicles: Control design and experimental results," *IEEE Transactions on Control Systems Technology*, vol. 25, no. 3, pp. 952–965, 2017.

[177] B. Xu, A. Yebi, S. Onori, Z. Filipi, X. Liu, J. Shutty, P. Anschel, and M. Hoffman, "Transient power optimization of an organic rankine cycle waste heat recovery system for heavy-duty diesel engine applications," *SAE International Journal of Alternative Powertrains*, vol. 6, no. 1, 2017.

[178] B. Xu, D. Rathod, A. Yebi, and Z. Filipi, "A comparative analysis of real-time power optimization for organic rankine cycle waste heat recovery systems," *Applied Thermal Engineering*, vol. 164, p. 114442, 2020.

[179] T. Yamamoto, T. Furuhata, N. Arai, and K. Mori, "Design and testing of the organic rankine cycle," *Energy*, vol. 26, no. 3, pp. 239–251, 2001.

[180] J. Peralez, P. Tona, O. Lepreux, A. Sciarretta, L. Voise, P. Dufour, and M. Nadri, "Improving the control performance of an organic rankine cycle system for waste heat recovery from a heavy-duty diesel engine using a model-based approach," in *52nd IEEE Conference on Decision and Control*, IEEE, 2013.

[181] A. Hernandez, A. Desideri, C. Ionescu, R. de Keyser, V. Lemort, and S. Quoilin, "Real-Time Optimization of Organic Rankine Cycle Systems by Extremum-Seeking Control," *Energies*, vol. 9, no. 5, p. 334, 2016.

[182] D. Seitz, O. Gehring, C. Bunz, M. Brunschier, and O. Sawodny, "Model-based control of exhaust heat recovery in a heavy-duty vehicle," *Control Engineering Practice*, vol. 70, pp. 15–28, 2018.

[183] P. Petr, C. Schröder, J. Köhler, and M. Gräber, "Optimal Control of Waste Heat Recovery Systems Applying Nonlinear Model Predictive Control," in *Proceedings of the 3rd International Seminar on ORC Power Systems* (V. Lemort, S. Quoilin, M. de Paepe, and M. van den Broek, eds.), pp. 1183–1192, 2015.

[184] X. Liu, A. Yebi, P. Anschel, J. Shutty, B. Xu, M. Hoffman, and S. Onori, "Model predictive control of an organic rankine cycle system," *Energy Procedia*, vol. 129, pp. 184–191, 2017.

[185] A. Caspari, A. M. Bremen, J. M. M. Faust, F. Jung, C. D. Kappatou, S. Sass, Y. Vaupel, R. Hannemann-Tamás, A. Mhamdi, and A. Mitsos, "DyOS - a framework for optimization of large-scale differential algebraic equation systems," in *Computer Aided Chemical Engineering*, pp. 619–624, Elsevier, 2019.

[186] D. Rathod, B. Xu, A. Yebi, A. Vahidi, Z. Filipi, and M. Hoffman, "A look-ahead model predictive optimal control strategy of a waste heat recovery-organic rankine cycle for automotive application," in *SAE Technical Paper Series*, SAE International, 2019.

[187] M. Schlegel, W. Marquardt, R. Ehrig, and U. Nowak, "Sensitivity analysis of linearly-implicit differential–algebraic systems by one-step extrapolation," *Applied Numerical Mathematics*, vol. 48, no. 1, pp. 83–102, 2004.

[188] M. Schlegel, K. Stockmann, T. Binder, and W. Marquardt, "Dynamic optimization using adaptive control vector parameterization," *Computers & Chemical Engineering*, vol. 29, no. 8, pp. 1731–1751, 2005.

[189] V. Grelet, P. Dufour, M. Nadri, T. Reiche, and V. Lemort, "Modeling and control of rankine based waste heat recovery systems for heavy duty trucks," *IFAC-PapersOnLine*, vol. 48, no. 8, pp. 568–573, 2015.

[190] E. Feru, F. Willems, B. de Jager, and M. Steinbuch, "Modeling and control of a parallel waste heat recovery system for euro-VI heavy-duty diesel engines," *Energies*, vol. 7, no. 10, pp. 6571–6592, 2014.

[191] H. Koppauer, W. Kemmetmüller, and A. Kugi, "Model predictive control of an automotive waste heat recovery system," *Control Engineering Practice*, vol. 81, pp. 28–42, 2018.

[192] A. Yebi, B. Xu, X. Liu, J. Shutty, P. Anschel, S. Onori, Z. Filipi, and M. Hoffman, "Nonlinear model predictive control strategies for a parallel evaporator

diesel engine waste heat recovery system," in *ASME 2016 Dynamic Systems and Control Conference*, American Society of Mechanical Engineers, 2016.

[193] E. Guerrero Merino, J. P. Schloder, and C. Kirches, "A nonlinear model-predictive control scheme for a heavy duty truck's waste heat recovery system featuring moving horizon estimation," in *2018 Annual American Control Conference (ACC)*, IEEE, 2018.

[194] V. Grelet, P. Dufour, M. Nadri, V. Lemort, and T. Reiche, "Explicit multi-model predictive control of a waste heat rankine based system for heavy duty trucks," in *2015 54th IEEE Conference on Decision and Control (CDC)*, IEEE, 2015.

[195] M. Diehl, H. G. Bock, and J. P. Schlöder, "A real-time iteration scheme for nonlinear optimization in optimal feedback control," *SIAM Journal on Control and Optimization*, vol. 43, no. 5, pp. 1714–1736, 2005.

[196] B. Houska, H. J. Ferreau, and M. Diehl, "ACADO toolkit-an open-source framework for automatic control and dynamic optimization," *Optimal Control Applications and Methods*, vol. 32, no. 3, pp. 298–312, 2011.

[197] F. Willems, F. Kupper, G. Rascanu, and E. Feru, "Integrated Energy and Emission Management for Diesel Engines with Waste Heat Recovery Using Dynamic Models," *Oil & Gas Science and Technology – Revue d'IFP Energies nouvelles*, vol. 70, no. 1, pp. 143–158, 2015.

[198] V. Lemort and A. Legros, "Positive displacement expanders for organic rankine cycle systems," in *Organic Rankine Cycle (ORC) Power Systems*, pp. 361–396, Elsevier, 2017.

[199] R. Hannemann, W. Marquardt, U. Naumann, and B. Gendler, "Discrete first- and second-order adjoints and automatic differentiation for the sensitivity analysis of dynamic models," *Procedia Computer Science*, vol. 1, no. 1, pp. 297–305, 2010.

[200] N. M. C. de Oliveira and L. T. Biegler, "Constraint handing and stability properties of model-predictive control," *AIChE Journal*, vol. 40, no. 7, pp. 1138–1155, 1994.

[201] E. E. Guerrero Merino, *Real-Time Optimization for Estimation and Control: Application to Waste Heat Recovery for Heavy Duty Trucks.* PhD thesis, University of Heidelberg, 2018.

[202] L. Del Re, L. Allgöwer, F. Glielmo, C. Guardiola, and I. Kolmanovsky, eds., *Automotive Model Predictive Control*. Springer-Verlag, 2010.

[203] B. M. Åkesson and H. T. Toivonen, "A neural network model predictive controller," *Journal of Process Control*, vol. 16, no. 9, pp. 937–946, 2006.

[204] S. Lucia, D. Navarro, B. Karg, H. Sarnago, and O. Lucia, "Deep learning-based model predictive control for resonant power converters," *arXiv:1810.04872*, 2018.

[205] B. Karg and S. Lucia, "Efficient representation and approximation of model predictive control laws via deep learning," *arXiv:1806.10644v1*, 2018.

[206] R. J. Lovelett, F. Dietrich, S. Lee, and I. G. Kevrekidis, "Some manifold learning considerations toward explicit model predictive control," *AIChE Journal*, 2020.

[207] M. H. Beale, M. T. Hagan, and H. B. Demuth, "Neural network toolbox," *User's Guide, MathWorks*, vol. 2, pp. 77–81, 2010.

[208] D. Angeli, R. Amrit, and J. B. Rawlings, "On average performance and stability of economic model predictive control," *IEEE Transactions on Automatic Control*, vol. 57, no. 7, pp. 1615–1626, 2012.

[209] M. Diehl, H. G. Bock, J. P. Schlöder, R. Findeisen, Z. Nagy, and F. Allgöwer, "Real-time optimization and nonlinear model predictive control of processes governed by differential-algebraic equations," *Journal of Process Control*, vol. 12, no. 4, pp. 577–585, 2002.

[210] W. Xie, I. Bonis, and C. Theodoropoulos, "Off-line model reduction for on-line linear MPC of nonlinear large-scale distributed systems," *Computers & Chemical Engineering*, vol. 35, no. 5, pp. 750–757, 2011.

[211] P. Schäfer, A. Caspari, A. Mhamdi, and A. Mitsos, "Economic nonlinear model predictive control using hybrid mechanistic data-driven models for optimal operation in real-time electricity markets: In-silico application to air separation processes," *Journal of Process Control*, vol. 84, pp. 171–181, 2019.

[212] A. Alessio and A. Bemporad, *A survey on explicit model predictive control*, pp. 345–369. Springer, 2009.

[213] T. Parisini, M. Sanguineti, and R. Zoppoli, "Nonlinear stabilization by receding-horizon neural regulators," in *Proceedings of 1995 34th IEEE Conference on Decision and Control*, IEEE.

[214] W. Dasoud, P. Kittisupakorn, M. Fikar, S. Lucia, and R. Paulen, "Efficient robust nonlinear model predictive control via approximate multi-stage programming: A neural network based approach," *Computer Aided Chemical Engineering*, vol. 46, pp. 1261–1266, 2019.

[215] B. Karg and S. Lucia, "Deep learning-based embedded mixed-integer model predictive control," in *2018 European Control Conference (ECC)*, IEEE, 2018.

[216] M. Hertneck, J. Köhler, S. Trimpe, and F. Allgöwer, "Learning an approximate model predictive controller with guarantees," *IEEE Control Systems Letters*, vol. 2, no. 3, pp. 543–548, 2018.

[217] S. Gros and M. Zanon, "Data-driven economic nmpc using reinforcement learning," *arXiv:1904.04152v1.*

[218] M. Zanon and S. Gros, "Safe reinforcement learning using robust mpc," *arXiv:1906.04005v1.*

[219] L. Hewing, K. P. Wabersich, M. Menner, and M. N. Zeilinger, "Learning-based model predictive control: Toward safe learning in control," *Annual Review of Control, Robotics, and Autonomous Systems*, vol. 3, no. 1, 2019.

[220] M. Ławryńczuk, "Practical nonlinear predictive control algorithms for neural wiener models," *Journal of Process Control*, vol. 23, no. 5, pp. 696–714, 2013.

[221] M. Ławryńczuk, "Explicit nonlinear predictive control algorithms with neural approximation," *Neurocomputing*, vol. 129, pp. 570 – 584, 2014.

[222] Z. Wu, A. Tran, D. Rincon, and P. D. Christofides, "Machine learning-based predictive control of nonlinear processes. part I: Theory," *AIChE Journal*, vol. 65, no. 11, 2019.

[223] Z. Wu, A. Tran, D. Rincon, and P. D. Christofides, "Machine-learning-based predictive control of nonlinear processes. part II: Computational implementation," *AIChE Journal*, vol. 65, no. 11, 2019.

[224] Z. Zhang, Z. Wu, D. Rincon, and P. D. Christofides, "Real-time optimization and control of nonlinear processes using machine learning," *Mathematics*, vol. 7, no. 10, p. 890, 2019.

[225] M. Diehl, H. J. Ferreau, and N. Haverbeke, "Efficient numerical methods for nonlinear MPC and moving horizon estimation," in *Nonlinear Model Predictive Control*, pp. 391–417, Springer Berlin Heidelberg, 2009.

[226] L. Würth, *Dynamic real time optimization for economically optimal operation of chemical processes*. PhD thesis, RWTH Aachen University, 2013.

[227] D. Masti and A. Bemporad, "Learning binary warm starts for multiparametric mixed-integer quadratic programming," in *Proceedings of the European Control Conference*, 2019.

[228] M. Klaučo, M. Kalúz, and M. Kvasnica, "Machine learning-based warm starting of active set methods in embedded model predictive control," *Engineering Applications of Artificial Intelligence*, vol. 77, pp. 1–8, 2019.

[229] P. M. Hidalgo and C. B. Brosilow, "Nonlinear model predictive control of styrene polymerization at unstable operating points," *Computers & Chemical Engineering*, vol. 14, no. 4-5, pp. 481–494, 1990.

[230] B. R. Maner, F. J. Doyle, B. A. Ogunnaike, and R. K. Pearson, "Nonlinear model predictive control of a simulated multivariable polymerization reactor using second-order volterra models," *Automatica*, vol. 32, no. 9, pp. 1285–1301, 1996.

[231] M. Z. Jamaludin and C. L. E. Swartz, "Approximation of closed-loop prediction for dynamic real-time optimization calculations," *Computers & Chemical Engineering*, vol. 103, pp. 23–38, 2017.

[232] R. Hannemann and W. Marquardt, "Continuous and discrete composite adjoints for the hessian of the lagrangian in shooting algorithms for dynamic optimization," *SIAM Journal on Scientific Computing*, vol. 31, no. 6, pp. 4675–4695, 2010.

[233] V. M. Zavala and L. T. Biegler, "The advanced-step NMPC controller: Optimality, stability and robustness," *Automatica*, vol. 45, no. 1, pp. 86–93, 2009.

[234] A. Caspari, L. Lüken, P. Schäfer, Y. Vaupel, A. Mhamdi, L. T. Biegler, and A. Mitsos, "Dynamic optimization with complementarity constraints: Smoothing for direct shooting," *Computers & Chemical Engineering*, vol. 139, p. 106891, 2020.

[235] P. Stechlinski, M. Patrascu, and P. I. Barton, "Nonsmooth differential-algebraic equations in chemical engineering," *Computers & Chemical Engineering*, vol. 114, pp. 52–68, 2018.

[236] L. P. Russo and B. W. Bequette, "Operability of chemical reactors: multiplicity behavior of a jacketed styrene polymerization reactor," *Chemical Engineering Science*, vol. 53, no. 1, pp. 27–45, 1998.

[237] M. Abadi, P. Barham, J. Chen, Z. Chen, A. Davis, J. Dean, M. Devin, S. Ghemawat, G. Irving, M. Isard, M. Kudlur, J. Levenberg, R. Monga, S. Moore, D. G. Murray, B. Steiner, P. Tucker, V. Vasudevan, P. Warden, M. Wicke, Y. Yu, and X. Zheng, "Tensorflow: A system for large-scale machine learning," in *12th USENIX Symposium on Operating Systems Design and Implementation (OSDI 16)*, (Savannah, GA), pp. 265–283, USENIX Association, 2016.

[238] F. Chollet *et al.*, "Keras." `https://keras.io`, 2015.

[239] D. P. Kingma and J. Ba, "Adam: A method for stochastic optimization," *arXiv:1412.6980v9*, 2014.